

Doctoral Thesis

**Study on the Development of a Rock
Identification System Using Artificial Intelligence
and Spectral Imaging**

Brian Bino Sinaice

Graduate school of International Resource Sciences

Division of Earth Resource Engineering and Environmental Science

Department of Geosciences, Geotechnology and Minerals Engineering for Resources

Akita University

September 2022

A dissertation submitted in partial fulfilment of the requirements for the degree Doctor of
Engineering

Copyright by Brian Bino Sinaice 2022

All Rights Reserved

DECLARATION

I Brian Bino Sinaice (Student ID. 6519111) do hereby declare that the work reported in this thesis was exclusively carried out by myself under the supervision of professor Tsuyoshi Adachi of Akita University. It describes the results of my own independent research except where due reference is made in the text. No part of this thesis has been submitted earlier or concurrently for the same or any other degree.

Candidate's signature

Date

Certified by

Professor Tsuyoshi Adachi (supervisor)

Supervisor's signature

Date

ACKNOWLEDGEMENTS

For this research to be a success, I would like to thank the following organizations as well as individuals:

First of all, I am grateful for the bilateral relations between Botswana and Japan. I thank the Japanese government for having awarded me with a 5.5-year long scholarship grant to pursue my master's (Apr. 2017 - Sep. 2019) as well as my doctorate (Oct. 2019 - Sep. 2022) studies. Through Japan's Ministry of Education, Culture, Sports, Science and Technology (MEXT) Japan and Akita University New frontier leader program for Rare-metal and resources, I was provided with a plethora of resources to facilitate the smooth running of my studies. I will forever be grateful for this once in a lifetime opportunity. I would like to thank Akita University professors for having sparked in me, a desire to pursue higher education post a short-stay program at Akita University in 2014. Additionally, would like to give thanks to the staff at Akita University's International Affairs Division for their support my guidance throughout every aspect of my life in Japan.

This research would not have been a success without the supervision, mentorship and support of professor Youhei Kawamura. I will forever be grateful to you for having facilitated my growth and development, both in terms of research and cycling. I would like to thank my supervising professor Tsuyoshi Adachi for taking over the reins and supervising me from 2021 to 2022. Special thanks also go out to the following senseis for taking part in my academic development; Prof. Shibuya and Kitahara (Tsukuba University); Dr. Nishikawa (Akita University Mining Museum); Dr. Utsuki; Prof. Shibayama, Ishiyama, Takasaki, Fuji, Imai, Miyamoto (Akita University); Dr. Bagai (University of Botswana) and Prof. Shemang (BIUST).

I am grateful to all my colleagues in the laboratory and leading program for their comments, insights and encouragement in writing this thesis and completing my degree. Most importantly, I am grateful for the support and love I have always received from my lab mates (Taeyoo, Jaewon, Jo, Ko, Yoshio, Kei, Rempei, Natsuo, Jun, Elsa, Kursat, Elisha, Yuimi, Rei, Yohei, Jalali, Khan, Dorj, Taiga, Ume, Zed, Yoshino, Takeuchi, Narihiro, Daniyar). They have been a family and I will forever be grateful for that. To the family in Japan (Watanabe-san, Kay, Fyfy, Tumelo, Beullah, Fiona, Mpho, Deezy, Larona, Labone, Lesego, Amo, Tsae, Admore Tonnie), I am indebted to you all for the love and support I have received from you.

Last but not least, I would like to thank God for his mercy and grace; my family; my parents Sainah Sinaice (mum) and Sinaice K. Sinaice (dad) for their love, and support, as well as for keeping me stable during stressful times. I appreciate the love, care and support from my girlfriend/life partner Segofalang Annah Modisenyane, she too is a researcher and has been instrumental in my academic endeavours. I thank God for you, and for forever being my backbone and pillar of strength, you indeed have been with me through thick and thin. I am blessed to have you by my side — much love to you.

ABSTRACT

It is imperative that one acknowledges that we now live in a digital age where almost every aspect of our daily lives produces an immense amount of data, with this, one may say the 21st century and those to come are and will be data-driven. With a closer look into the mining industry, trends show a steady but inevitable shift from traditional to modern digital methods. One may attribute this shift to a number of reasons such as the shortage of specialists in various fields within the mining industry, be it exploration, monitoring, maintenance, and processing amongst others. Also, there is a lessening desire to conduct on-sight investigations as health and safety regulations stiffen along with the necessity to distance human life from occupational mishaps. Lastly, traditional methods of delineating rocks and minerals may at times be thought of as subjective, which is an inherent part of procedures conducted by humans. For this reason, this study aims to provide solutions to these problems through the employment of artificially intelligent (AI) algorithms, which are known to be objective in their analysis. Coupled with spectral imaging techniques in the discrimination of rocks and minerals, the study was split into three main chapters, each covering the achievable potential advantages of employing AI-based classifications, hence solving the aforementioned problems.

The first aim was to combine two technologies to classify rocks; hyperspectral imaging, and artificial intelligence in the form of a one-dimensional deep learning convolution neural network (1D DL CNN). In order to classify rocks, visual imagery data generated using a hyperspectral camera was quantified in terms of how each captured image pixel responds across the electromagnetic spectrum, obtaining hyperspectral signatures of that particular rock. The second step involved running the hyperspectral signature data in a 1D CNN, application of this highly capable DL technique allows one to perform classification procedures with minimal error. The output results showed that the 1D CNN was capable of performing rock

classifications via hyperspectral signatures as supported by the optimised (across three models) average per class prediction precision of 91.2% for all eight igneous rock lithologies employed in this part of the study.

Having realized the time, computational and data storage costs attained in solving the first aim, the second aim was thus an attempt to develop a method by which rock classification may be performed without these costs. This was achieved by integrating Hyperspectral Imaging, Neighbourhood Component Analysis (NCA) and Machine Learning (ML) as a combined system that can classify rocks. Modestly put, hyperspectral imaging gathers electromagnetic signatures of the rocks in hundreds of spectral bands. However, this data suffers from what is termed the ‘dimensionality curse’, which led to the employment of NCA as a dimensionality reduction technique. NCA, in turn, highlights the most discriminant feature bands, the number of which is dependent on the intended application(s) of the system. The study’s envisioned application was rock classification via specialized multispectral bands. Hence, the study performed a 204-band hyperspectral to 5-band multispectral reduction, the reason being, that current production drones are limited to five multispectral band sensors. Based on these bands, the study applied ML to identify and classify rocks, thereby supporting the study’s hypothesis, reducing computational costs, and attaining an average optimized ML classification accuracy of 91.2%.

The third aim was to investigate the potential use of drones in mining environments as a way in which data pertaining to the state of a site may be remotely collected. This aim proposes a combined system that employs a six bands multispectral image capturing camera mounted on an Unmanned Aerial Vehicle (UAV) drone, Spectral Angle Mapping (SAM), as well as AI. Unlike in the second aim, the 6 multispectral bands are factory pre-set, hence the employment of SAM to aid in pinpointing the spectra of sought after magnetite iron sands. Depth possessing multispectral data was captured at different flight elevations in an attempt to

find the best elevation where remote identification via the UAV drone was possible. Data was analysed via SAM to deduce the cosine similarity thresholds at each elevation. Using these thresholds, AI algorithms were trained and tested to find the best performing model at classifying magnetite iron sand. Considering the post-flight logs, the spatial area coverage of 338 m², a global classification accuracy of 99.7%, as well the per-class precision of 99.4%, the 20 m flight elevation outputs presented the best performance ratios overall.

In conclusion, the study emphasizes that the employment of AI-based spectral imaging methods in various aspects of the mining industry is necessary to ensure the continuation of a robust and future-proof rock and mineral classification practice. Lastly, data-driven classification practices are sustainable, easily optimizable, repeatable, and objective in their outputs, deeming the proposed systems viable for current and future industrial applications.

TABLE OF CONTENTS

ACKNOWLEDGEMENTS	i
ABSTRACT	iii
LIST OF FIGURES	viii
LIST OF TABLES	xi
LIST OF ABBREVIATIONS	xii
CHAPTER 1: Introduction	1
1.1. Background	1
1.1.1. Spectral Imaging	2
1.1.2. Remote Sensing.....	4
1.1.3. Data Processing via AI Algorithms.....	5
1.2. Purpose of the Study	7
1.3. Outline of the Study	8
CHAPTER 2: Application of a 1D Deep Learning CNN in the Classification of Rocks via Hyperspectral Imaging	10
2.1. Introduction.....	10
2.2. Methodology	12
2.1.1. Hyperspectral Imaging.....	12
2.2.2. Why Employ Deep Learning Networks.....	13
2.3. Practical Experiments	16
2.3.1. Capturing Rock Hyperspectral Signatures.....	16
2.3.2. Data Pre-processing	21
2.4. Experimental and Analytical Results.....	22
2.4.1. Findings Based on Hyperspectral Imaging	22
2.4.1.1. Hyperspectral signatures as image mean anomalies	22
2.4.1.2. Compilation of all average rock hyperspectral signatures	23
2.4.1.3. Hyperspectral signatures at pixel level anomalies	24
2.4.2. Rock 1D CNN Prediction and Classification.....	27
2.5. Discussion	33
2.6. Conclusion	36
CHAPTER 3: Coupled with Machine Learning, Achieving Specialized Rock Multispectral Imaging via Dimensionality Reduction from Hyperspectral Imaging.....	37
3.1. Introduction.....	37
3.2. Methodology for Coupling Dimensionality Reduction with Machine Learning	40

3.2.1. Hyperspectral Imaging.....	40
3.2.2. Dimensionality Reduction.....	41
3.2.2.1. Supervised vs Unsupervised Dimensionality Reduction Methods	41
3.2.2.2. Why Employ NCA.....	42
3.2.3. Why Machine Learning?.....	44
3.3. Practical Experiments	45
3.3.1. Capturing Rock Hyperspectral Signatures.....	45
3.3.2. Selecting the Appropriate Feature Bands.....	46
3.3.3. Post-NCA Classification via ML	48
3.4. Experimental and Analytical Results	48
3.4.1. Findings Based on NCA.....	48
3.4.2. Classification with ML, Post-NCA	56
3.5. Significance of Proposed System.....	64
3.6. Conclusions.....	66
CHAPTER 4: Capabilities of a Multispectral Imaging UAV Drone in Identifying Minerals via SAM and AI Techniques: A Case Study on Magnetite Iron Sands.....	68
4.1. Introduction.....	68
4.2. Methodological Strategies for SAM and AI Integration.....	71
4.2.1. UAV Drone Mounted Multispectral Imaging.....	71
4.2.2. Parallax Error Correction	74
4.2.3. A Scrutiny of SAM Analysis	75
4.2.4. Benefits of Employing ML and DL AI Methods in Magnetite Identification	77
4.3. Experimental and Analytical Results	78
4.3.1. In the field UAV Drone Analytics	78
4.3.2. Outputs Pertaining to SAM Analysis.....	80
4.3.3. Application of AI Methods in Magnetite Spectral Classification post SAM.....	83
4.3.3.1 Classification via Machine Learning Models.....	85
4.3.3.2 Classification via Deep Learning CNN.....	88
4.4. Discussion	91
4.5. Conclusions.....	94
CHAPTER 5: Study Conclusions.....	96
REFERENCES.....	100

LIST OF FIGURES

Chapter 1

Figure 1.1: Relationship between the different kinds of electromagnetic radiation with the VNIR highlighted in red.....	3
Figure 1.2: Relationship between different levels of spectroscopy based on band resolution. 3	
Figure 1.3: Overview of spectral imaging applications employed for regional scale remote sensing practices. Adapted from: https://www.harris.com/ (6 Nov, 2020).....	5
Figure 1.4: Relationship between artificial intelligence, machine learning and deep learning algorithms.....	6
Figure 1.5: Overview of the study showing chapters and methods employed (1 dimensional convolution neural network (1D CNN, deep learning (DL), dimensionality reduction (DR), hyperspectral imaging (HSI), machine learning (ML), multispectral imaging (MSI), Neighborhood Component Analysis (NCA), Spectral Angle Mapping (SAM), Unmanned Aerial Vehicle (UAV).	9

Chapter 2

Figure 2.1: Typical representation of feature extraction from a 2D CNN with convolution and maximum pooling layers (C1-3 and MP1-2 respectively). The main CNN layers are input layer, hidden layer and output layer.	14
Figure 2.2: Simplified (i) and true (ii) structure of the 1D CNN with input, hidden and output layers.	15
Figure 2.3: Classification diagrams showing the plutonic (i) and volcanic (ii) rocks which were of interest for this study to be carried out: (1) granite (2) diorite (3) gabbro (4) granodiorite (a) rhyolite (b) andesite (c) basalt (d) dacite.	17
Figure 2.4: Experimental set-up showing the main components of Visible-NIR hyperspectral imaging system. The camera extracts data and sends it straight to the computer system where data can then be used for various kinds of analysis.	18
Figure 2.5: Images of some of the 32 rock samples from eight rock lithologies used in building the rock hyperspectral database.	18
Figure 2.6: Automatic random extraction of rock pixel spectra captured via a Specim IQ camera that acquires 512×512 pixel images from 204 bands within the visible-near-infrared range. Extracted spectra are used to build a rock hyperspectral database.....	20
Figure 2.7: Representation of how the data was handled during the training and testing processes (data pre-processing).....	22
Figure 2.8: Hyperspectral signatures of rocks as whole image average anomalies.....	23
Figure 2.9: All rock hyperspectral signatures as per rock image averages.....	24
Figure 2.10: Reflectance hyperspectral signatures of eight rock lithologies employed in the construction of a hyperspectral database. Each anomaly represents the interaction between each 20×20 pixels 2D area with a depth of 204 bands within a rock's hyperspectral image with light, captured via a Visible-Near-Infrared-Range hyperspectral camera.	26
Figure 2.11: Plutonic rocks training progress showing a high validation accuracy of 88.2 % and a low loss function plot.	29
Figure 2.12: Volcanic rocks training progress showing a high validation accuracy of 74.3% and low loss function plot.	29

Figure 2.13: Igneous rocks training progress showing a high validation accuracy of 96.4 % and low loss function plot.	30
Figure 2.14: Post training plutonic rocks confusion matrix.....	32
Figure 2.15: Post training volcanic rocks confusion matrix.	32
Figure 2.16: Post training igneous rocks confusion matrix.	33
Figure 2.17: Post training global accuracy and average per-class classification capability comparisons.....	34
Figure 2.18: Post training model comparisons per rock in the database.	35

Chapter 3

Figure 3.1: The proposed system design, consisting of hyperspectral imaging, dimensionality reduction via Neighbourhood Component Analysis, Machine Learning classification of rocks and minerals to test system viability based on the selected features, and finally employing those features together with the ML model in developing a unmanned aerial vehicle drone-mountable multispectral camera.	39
Figure 3.2: A hyperspectral signature database with 204 dimensionalities from within the VNIR.	45
Figure 3.3: A hyperspectral signature database with 204 dimensionalities from within the VNIR.	47
Figure 3.4: Neighbourhood Component Analysis feature selection which assigns higher weights to the most discriminatory hyperspectral bands by eliminating redundancy in data, with the top five feature-bands being 14, 46, 116, 133 and 169.	50
Figure 3.5: Projection of complex rock hyperspectral signature data points in dimensionality reduced (via Neighbourhood Component Analysis feature selection) 2D planes showing the relative reflectance spectral strength relationships between five different spectral bands for eight rock lithologies.	54
Figure 3.6: Post Neighbourhood Component Analysis hyperspectral signature projections as relative frequency histograms; a simplification of Figure 3.5.	55
Figure 3.7: Database handling of training and testing sets. A 5-fold-cross-validation was used in all instances.	57
Figure 3.8: Confusion matrix from a Cubic SVM machine learning model used in evaluating the classification viability of post dimensionality reduction spectral bands.....	61

Chapter 4

Figure 4.1: Map showing Kamaiso magnetite iron sand placer deposits. Red polygon represents the 30m by 90 m study area within which the UAV drone shown was flown. Map acquired from: Google maps (2021).	71
Figure 4.2: The 6 bands multispectral sensor with a 62.7° field of view; [1] Blue: 450 nm ± 16 nm, [2] Green: 560 nm ± 16 nm, [3] Red: 650 nm ± 16 nm, [4] Red Edge: 730 nm ± 16 nm, [5] Near Infrared: 840 nm ± 26 nm and [6] RGB camera: 400-1000 nm represent the multispectral sensor capabilities. Images captured are corrected for parallax error via an edge detection method. The red point is the reference area from which magnetite iron sands are known to exist.	73
Figure 4.3: Schematic diagram showing the principle of SAM cosine similarity. Reference spectrum is what is sought after. Angle α is the cosine similarity threshold between a reference and a synthetic spectrum.	76

- Figure 4.4:** Illustration of the difference spatial resolutions of each image, attained from capturing multispectral images at 2 m, 10 m, and 20 m flight elevations.....79
- Figure 4.5:** SAM analysis at 2 m, 10 m and 20 m UAV drone elevations at different reference spectral thresholds. The red points represent the user selected reference point known to be magnetite (pre-SAM), whilst the blue overlay represent areas within the threshold limit thought to be magnetite (post SAM cosine similarity). The best threshold cosine similarities are 0.12, 0.13 and 0.17 at 2 m, 10 m and 20 m respectively. The x and y axis represent the size of each captured multispectral image. The bar on the right of each first image represent the variation in spectral intensities present in each captured image.82
- Figure 4.6:** Extraction of segmentation maps used to create a magnetite iron sand database. Segmentation maps at each UAV flight elevation are based on the 0.12, 0.13 and 0.17 cosine similarity thresholds at 2 m, 10 m and 20 m.83
- Figure 4.7:** Extraction of segmentation maps used to create a magnetite iron sand database. Proposed process overview with emphasis on how data extracted from spectral angle mapping cosine similarities is segmented, assigned ground truths, and used in training artificially intelligent algorithms in the classification of magnetite iron sand.....84
- Figure 4.8:** Input dataset sizes used to train the machine learning and deep learning algorithms as well as selection of the best performing model at each UAV flight elevation.85
- Figure 4.9:** Machine learning confusion matrices from Ensemble (RUS Boosted Trees) at 2 m UAV drone elevation, Tree (Course-tree) at 10 m UAV drone elevation, and Tree (Course-tree) at 20 m UAV drone.....88
- Figure 4.10:** Deep learning one dimensional convolution neural network confusion matrices at 2 m, 10 m and 20 m UAV drone elevation.91
- Figure 4.11:** Global accuracy and pre-class precision: best performing machine learning vs. deep learning classification models based on SAM cosine similarity thresholds at 2 m, 10 m and 20 m.....93
- Figure 4.12:** Model training durations: best performing machine learning vs. deep learning classification models based on SAM cosine similarity thresholds at 2 m, 10 m and 20 m.94

LIST OF TABLES

Chapter 2

Table 2.1: Results of the deep learning data, acquired from the hyperspectral signatures of the plutonic and volcanic rocks.....	33
---	-----------

Chapter 3

Table 3.1: Top five machine learning classification comparisons based on pre-dimensionality reduction from 204-bands, to post-dimensionality reduction (using Neighbourhood Component Analysis) for 100, 50, 25, 10 and 5 rock spectral bands.	59
Table 3.2: Optimized ML classification capabilities for subject rock vs. other rocks post NCA.	63
Table 3.3: Summary of ML classification precisions based on Figure. 3.8, Table 3.1 and Table 3.2 post NCA outputs.	64

Chapter 4

Table 4.1: Multispectral UAV drone post flight logs from operating at 3 different flight elevations.....	79
Table 4.2: Top 3 machine learning classification model comparisons at 2 m, 10 m and 20 m UAV flight elevations based 0.12, 0.13 and 0.17 SAM cosine similarity thresholds respectively.	87
Table 4.3: Deep learning one dimensional convolution neural network classification model comparisons at 2 m, 10 m and 20 m UAV flight elevations based 0.12, 0.13 and 0.17 SAM cosine similarity thresholds respectively.	90

LIST OF ABBREVIATIONS

AI	→	Artificial intelligence
CNN	→	Convolution Neural Network
DL	→	Deep learning
DR	→	Dimensionality reduction
HSI	→	Hyperspectral imaging
ML	→	Machine learning
MSI	→	Multispectral imaging
NCA	→	Neighborhood Component Analysis
SAM	→	Spectral Angle Mapping
UAV	→	Unmanned Aerial Vehicle
VNIR	→	Visible-near-infrared
1D	→	1 dimensional

CHAPTER 1: Introduction

This chapter discusses the essence of the study, it gives a glimpse into the problem statement, the general background literature, as well as the purpose of this study.

1.1. Background

Rock and mineral classification tasks are of the utmost importance in the mining, rock and mineral engineering industries (Fox et al., 2017). The world, however, has been experiencing a decline in mineral grades, strengthening of safety regulations, shortage of specialists and the shift from in the field investigations (Nageshwaranier et al., 2018). Thus, it would make sense for these industries to invest in technologies that may improve any aspect of the value chain so as to solve these problems and remain profitable. With the digital age the world is currently experiencing, an undertaking of this magnitude usually encompasses performing remote assessments of phenomena, the application of high computation power, as well as performing these tasks in the most cost effective manner (Gaffey and Bhardwaj, 2020). In recent years, with respect to the mining industry, we have seen the introduction and application of various technology based rock identification methods (Ganesh et al., 2017). This rapid transformation from traditional to more modern techniques is driven by the need to perform faster, and accurate rock identification. It is for this reason that this paper attempts to investigate the abilities of artificial intelligence (AI) in performing rock classification via hyperspectral as well as multispectral imaging techniques.

The adoption of advanced automated technology in the mining industry has proven to be highly effective in improving sustainability and efficiencies (Heinz et al., 2004). This is greatly due to the optimisation of system designs, data collection methods and the overall implementation of automation. From this, it is clear that the mining industry strives for the

improvement of safety regulations by increasing the distance between miners and the environment (Jia et al., 2016). This is where automated technology plays its part, by improving site data collection methods followed by high accuracy analysis methods (Zhang and Li, 2014). Such improvements, as will be described in this study include hyperspectral imaging in the distinction of rocks, dimensionality reduction from hyperspectral imaging to multispectral imaging, and the integration of multispectral imaging with unmanned aerial vehicle (UAV) technology. Data assessment via these methodologies will be performed by various AI algorithms. To begin the investigation, one needs to understand the concept of spectral imaging, remote sensing, and AI.

1.1.1. Spectral Imaging

In order to understand the concept of spectral imaging, which usually takes place within the visible-near-infrared (VNIR) range of 400-1000 nm (Figure 1.1), one needs to understand how spectroscopy has evolved ever since its discovery. This entails understanding the different types or levels of spectroscopy from those with the lowest to the ones with the highest spectral resolution (Debba et al., 2005; Wright et al., 2013; van Ruitenbeek et al., 2012). With advancements in science, there have been developments which allow spectrometers to be divided into even smaller spectral bands whilst maintaining the same spectral range (Figure 1.2). Farooq et al. (2014), point out that these spectrometers are also said to maintain high sensitivity in terms of detection and absorption of reflected electromagnetic radiation from objects; which for this study objects in question are rocks.

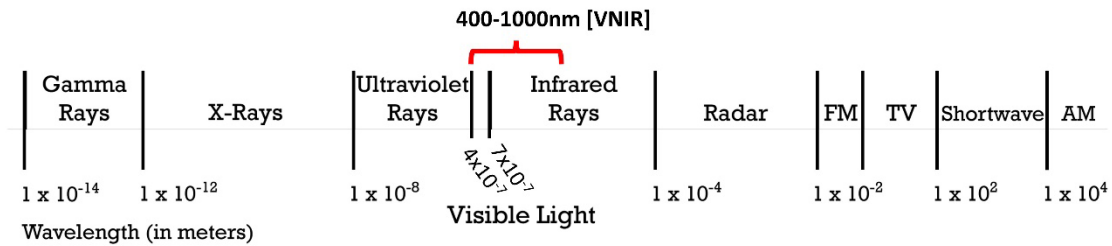


Figure 1.1: Relationship between the different kinds of electromagnetic radiation with the VNIR highlighted in red.

From Figure 1.2, one is able to visually set apart different resolutions of spectral imaging. Within the VNIR, broadband has 2 spectral channels, which gives it a poor spectral resolution, whilst multispectral imaging has 10's of spectral channels within the same spectral range (Tompkins & Pieters, 1999; Spinetti et al., 2009; Savage et al., 2012). Lastly, hyperspectral imaging has 100's of spectral channels within the same range (Fox et al., 2017; Salvatore et al., 2014), giving it the best spectral resolution with the ability to distinguish material characteristics with finer details across the spectral range (Li et al., 2017). With this said, it means rock spectral signatures will potentially be easily distinguishable through the employment of both hyperspectral as well as multispectral imaging.

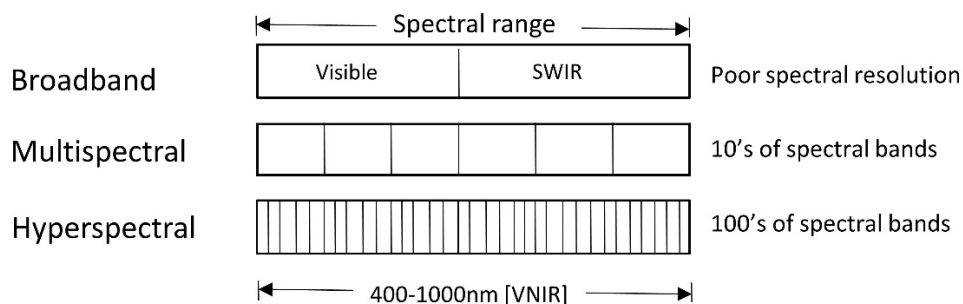


Figure 1.2: Relationship between different levels of spectroscopy based on band resolution.

1.1.2. Remote Sensing

As shown in Figure 1.3, Zhang & Li (2014), explain that since the discovery and employment of spectral imaging by the geology and rock engineering community via satellites, spectral imaging has been employed for regional mapping. This has been the case for different purposes such as the discrimination of different soil types from place to place (Jie et al, 2018). Lithological mapping of large rock formations and how they transition or interact with each other to explain geological phenomena (Landgrebe, 1999) too has been investigated. Vegetation mapping to investigate how and why different flora are found in certain regions and not others (Qiu et al., 2017) has taken advantage of satellite remote sensing. Lastly, tracing water movements in order to investigate possible mineral and/or contaminant constituents present within it is one of the practices that have taken advantage of satellite remote sensing (Farooq et al., 2014).

For this reason, this has driven other industries and academic organizations to further develop and take advantage of these aerial investigation technologies as they see major advantages in combining high-resolution spectral imaging over normal colour imaging techniques (Meer, 2006). Hence for this study, remote sensing investigations combining a 6 band multispectral camera with a UAV drone will be investigated. Positive results from this amalgamation will render such a system highly capable of rock and mineral discrimination or classification from a remote area via spectral imaging (Jun-Hu & Da-Wen., 2014).

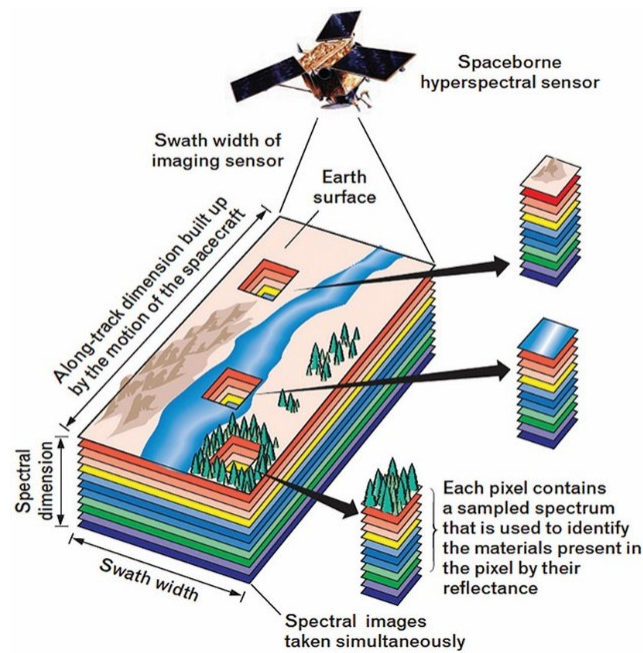


Figure 1.3: Overview of spectral imaging applications employed for regional scale remote sensing practices. Adapted from: <https://www.harris.com/> (6 Nov, 2020)

1.1.3. Data Processing via AI Algorithms

In order to make calculations, humans need to use their brainpower so as to attain quick and accurate results all the time (Jia et al., 2016; Zhang et al., 2017; Tang et al., 2017). However, the human brain has limitations in terms of the number of calculations viable for processing per specific time (Karen et al., 2013; Ma et al., 2017). Hence, scientists have developed computers with even more computational power, able to carry out multitudes of calculations with little or no error, keep data, and reemploy it wherever need be after learning, just as a human being's brain would (Shugao et al., 2017; Altaf et al., 2019; Dolz et al., 2018). This computer brain (Figure 1.4), has earned the name 'AI'. Within artificial intelligence, exists machine learning (ML), as well as deep learning (DL) convolutional neural networks (CNN), which will be employed in this study's rock classification via spectral imaging problems.

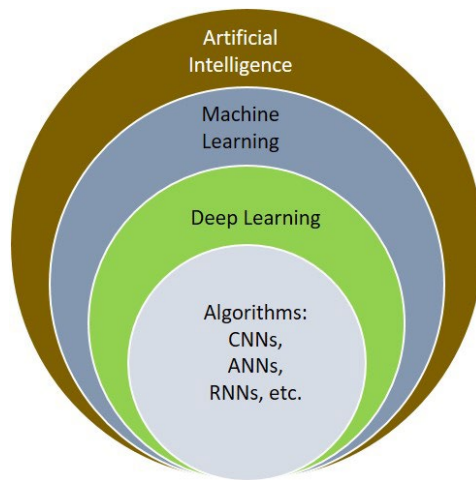


Figure 1.4: Relationship between artificial intelligence, machine learning and deep learning algorithms.

Though both ML and DL AI algorithms are useful in multitudes of data-related tasks such as the classification problem being investigated in this study, they differ in several ways. ML algorithms are mathematical engines of AI, which means these algorithms attribute their classification abilities to perceived mathematical relationships present within the data (Hartog et al., 2021). In simple terms, ML algorithms try to fit the data within a particular pattern which can be described using mathematical functions. Examples of machine learning algorithms include Linear Regression, Decision Trees and k-Means amongst others (Shafri et al., 2007). These algorithms are relatively easier to employ, hence, several ML algorithms will be investigated in this study.

DL, on the other hand, is far more sophisticated in its architecture compared to ML algorithms (Ganesh and Kannan, 2017). They are complex and multi-layered; and are built to allow data to pass through information processing layers (like human brain neurons) in highly connected ways, the result is a non-linear transformation of data which cannot be described by a mathematical function (Ganesh and Kannan, 2017; Shafri et al., 2007; Hartog et al., 2021). It does however take a large amount of data compared to ML to train DL algorithms in order to attain high accuracy output models (Hartog et al., 2021). For this study, a one dimensional (1D)

CNN is employed. This type of CNN was applied as it is known to be highly capable of classifying imagery and waveform data (Fox et al., 2017), which coincides with the data structures presented in this study.

1.2. Purpose of the Study

The benefits of employing this proposed system within the mining industry are endless. For instance, spectral signatures are more than viable in the discrimination of rocks and minerals (Ganesh and Kannan, 2017). This may be for the purpose of determining the correct blasting procedures based on the type and state of rocks. Moreover, mining engineers are always faced with tasks, such as determining adequate slope angles within open-pit mines, determining dilution ratios in the processing of ore, and determining waste rock quantities, among other standards (Rahimi et al., 2021). These all depend on rock and mineral information, this information being attainable via rock and mineral spectral signatures without the need to employ expensive, risky, and time-consuming investigations, hence achieving cost efficiency, fast data collection times, human life protection, and quicker analysis rates. In order to assess the full capabilities of the systems, a series of questions will be answered by each of the following chapters in an attempt to address the gaps observed in previous literature;

In chapter 2, using eight igneous rocks (granite, diorite, gabbro, granodiorite, rhyolite, andesite, basalt and dacite), the study will:

- Strive to visually distinguish rocks based on their VNIR hyperspectral signatures;
- Assess the classification abilities of a 1D CNN in distinguishing rocks based on 204-band hyperspectral signatures.

In chapter 3, using the same igneous rocks as in chapter 2 (granite, diorite, gabbro, granodiorite, rhyolite, andesite, basalt and dacite), the study will:

- Determine the 5 most important spectral bands necessary to classify rocks via conversion from hyperspectral to multispectral imaging, this will be achieved through dimensionality reduction from 204 hyperspectral bands, to 5 multispectral bands;
- Assess the differences in retained attainable classification capabilities pre and post dimensionality reduction.

In chapter 4, a case study on magnetite iron sands, the study will:

- Investigate the capabilities of a 6 bands multispectral camera mounted on a UAV drone across 3 different flight elevations;
- Perform Spectral Angle Mapping (SAM) in order to highlight the sought after subject (magnetite iron sands);
- Investigate the benefits of employing a 6 bands multispectral UAV drone in mineral identification based on both ML and DL classification capabilities.

1.3. Outline of the Study

As Figure 1.5 shows, Chapter 1 gives a general introduction and background of the study. It moreover stresses the study's goals. Chapter 2 addressed the capabilities of a 1D CNN in classifying rocks based on their hyperspectral signatures. In an attempt to classify rocks with a reduced computational power requirement, Chapter 3 assesses dimensionality reduction via NCA of 204 hyperspectral imaging bands to 5 specialized multispectral bands. Quantitative system capabilities are presented via ML models. In Chapter 4, a 6 multispectral bands UAV drone flown at 3 different flight elevations is applied in mineral classification of magnetite iron sand. Based on the SAM analysis results at each elevation, ML and DL models will be used in ascertaining the classification capabilities of the system. Chapter 5 ties the findings of Chapters 2, 3 and 4, and presents the study's overall conclusions.

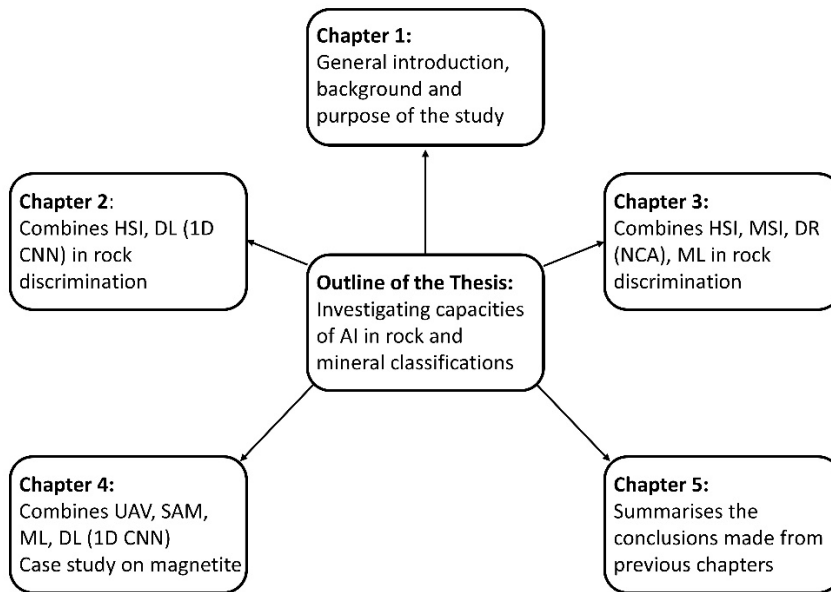


Figure 1.5: Overview of the study showing chapters and methods employed (1 dimensional convolution neural network (1D CNN, deep learning (DL), dimensionality reduction (DR), hyperspectral imaging (HSI), machine learning (ML), multispectral imaging (MSI), Neighborhood Component Analysis (NCA), Spectral Angle Mapping (SAM), Unmanned Aerial Vehicle (UAV)).

CHAPTER 2: Application of a 1D Deep Learning CNN in the Classification of Rocks via Hyperspectral Imaging

This chapter investigates the capabilities of a 1 dimensional convolution neural network in classifying eight igneous rock lithologies based on their visible-near-infrared range hyperspectral signatures.

2.1. Introduction

This chapter proposes a synchronization between rock identification and classification, with modern technological advances namely hyperspectral imaging and deep learning for applications in mining and related geoenvironmental works or industries. In order to assess the full capabilities of the system, a series of questions have to be answered; are rocks distinguishable based on their hyperspectral signatures? how robust and accurate can the one-dimensional convolution neural network (1D CNN) algorithm be? finally, what are the attainable classification predictions? For this chapter, eight igneous rock lithologies with each represented by 4 rock samples were employed for this rock classification problem. The plutonic rock counterparts were namely granite, diorite, gabbro and granodiorite, whereas their volcanic equivalents were rhyolite, andesite, basalt and dacite respectively.

In simple terms, as previously defined in Chapter 1, spectroscopy is the study of light as a function of wavelength that has been emitted, reflected or scattered from a solid, liquid or gas (Meer et al., 2006). Variances in each of these wavelengths are what make it possible to identify or detect even that which a naked eye would not. From this definition, hyperspectral imaging is therefore the technology that acquires images of the same scene in hundreds of contiguous and narrow spectral bands (Li et al., 2017). It allows one to collect information for each pixel in an image scene, hence enabling the digital imaging of geological materials and

the measurement of their reflectance spectra in the visible-near-infrared range' (VNIR) portions of the electromagnetic spectrum (400-1000 nm). Since every pixel in the image contains a continuous spectrum (reflectance), the technique has the potential to be manipulated for a broad number of uses (Nageshwaranier et al., 2018), including but not limited to the identification and characterization of complex structural and mineralogical alteration assemblages (Qiu et al., 2017).

Having stated the above, it is critical to handle this data with accurate and precise analytical methods, hence the proposed integration of hyperspectral imaging with deep learning (DL) models. DL is generally defined as a subset of machine learning in the broader subject of artificial intelligence, it is said to have networks capable of learning with little or no supervision from data which would be considered unstructured or poorly organized (Jie et al., 2018). Marais & Aldrich (2011) further mention that deep learning has proved to be a highly effective tool in image analysis, particularly its CNN algorithm, where it has been subjected to many different tasks, some of which include document and face recognition (Zhang et al., 2017). This is moreover supported by Portia et al. (2016), who state that CNNs have over the years proved to be highly effective in feature extraction and representation of visual imagery. It is for this reason that this chapter aimed at exploring the capability of this extreme learning machine on high-level deep features of rock hyperspectral signatures and potentially employ this technology in various mining activities (Zhang et al., 2017).

By being able to classify changes in lithology, engineers will be able to assess and come up with appropriate mining and blasting methods that better suit that particular lithology and its structural characteristics. Moreover, this system has the capacity to detect moisture content anomalies in rocks if need be, as it is often said that 'water is the number one enemy when it comes to mining and rock stability' (Sitharam & Kolathayar, 2020) due to its ability to seep through rock structures, hence weakening their overall integrity.

2.2. Methodology

2.1.1. Hyperspectral Imaging

Hyperspectral remote sensing with high spectral resolving properties has been established as one of the important applications in mineral/lithological mapping as it has a higher spectral resolution as compared to the conventional multispectral technology with a lesser number of spectral bands within a given wavelength range (Kruse, 2012; Rowan et al., 2000; Mangold et al., 2017; Kim et al., 2016). Scientists around the world now see great potential in accurately identifying and mapping the constituents of the earth's surface since its introduction. Various methods have been developed and have produced very promising results in lithological diagramming (Meer, 2006; Chen et al., 2007; Farooq & Govil 2014).

Hyperspectral imaging, as defined by researchers (Beretta et al., 2018; Martelet et al 2021; Galal et al., 2012), refers to the collection of hundreds of pixel-scale imagery information pertaining to a subject from within the electromagnetic spectrum. The collection of such data, which in our case was within the VNIR range, numerically translates to the 400–1000 nm electromagnetic spectrum. Hyperspectral imaging is a graduation from multispectral imaging, meaning that within the same spectral range, hyperspectral imaging has a higher resolution, thereby facilitating the extraction of detailed spectral signatures (Beretta et al., 2018; Shafri et al., 2007; Martelet et al 2021). Since its discovery, it has seen various applications in fields, such as soil sciences, hydrology, geology and the mining industry (Saha and Annamalai, 2021; Debba et al., 2005). When an image is captured using a hyperspectral camera such as the 204 band Specim IQ camera used in this study, information pertaining to the subject's interaction with light is recorded (Girouard et al., 2004). This makes each of the 204 VNIR spectral bands receive a specific signal within each of the approximately 3 nm wide spectral bands. It should be mentioned that camera specifications may differ in terms of the number of spectral bands

per spectral range provided by a certain manufacturer. This, in essence, affects the width of each spectral band, it however does not affect the underlying signatures exhibited by specific rocks and minerals.

2.2.2. Why Employ Deep Learning Networks

Recently, techniques based on deep learning approaches have demonstrated their effectiveness as compared to conventional hand-crafted techniques, and have become the state-of-the-art in many applications such as remote sensing and geotechnical engineering (Vetrivel et al., 2017). The underlying reason why deep learning holds the potential to overcome deficiencies found in previously employed intelligent diagnosis techniques is in its incorporation of a class of machine learning techniques such as CNNs, which are further aided by the various layers of information processing stages used to exploit pattern classifications (Marais & Aldrich, 2011; Singh et al., 2021). Jang et al. (2015) support this statement by saying it is primarily due to these deep architectures that deep learning neural networks are able to adaptively capture the finest details in representative information from raw data.

Since the time when the idea of deep learning appeared in science, it has appealed to a lot of researchers from different fields (Jia et al., 2016). The core of within the deep learning structure is to let the network directly learn the feature representations and concurrently train with thorough prediction tasks from end to end (Zhang et al., 2017; Al Sallab & Rashwan 2011; Haixiang et al., 2017; Mohammadi & Rezaei 2020), which as a result aids the deep learning models set new strides for many vision tasks. It is for this sophisticated reason that this chapter proposes the employment of a CNN to classify rocks based on their hyperspectral signatures. Although with many successes, it is worth mentioning that deep learning models are still mostly thought of as ‘hard to implement’ as they require multitudes of data in order to operate and

need several ‘tips and tricks’ (Xinga et al., 2017; Estrada-Ruiz and Pérez-Garibay, 2009), hence the need to continuously expand databases and refine neural network algorithms.

As shown in Figures 2.1 and 2.2, a typical CNN has 3 main layers, an input layer, where raw data is located, this data may be in form of 2D image data or 1D wave form data. For this classification task, hyperspectral imagery data which has a structure similar to wave-forms will be processed via the 1D CNN (Figure 2.2). The second main layer of a CNN is the hidden layer, which houses the convolution layers which specialize in detecting and locating localized features (Xinga et al., 2017). The convolution layer works by assigning a weight called a filter/kernel which is multiplied with input data as shown in Figures 2.1 and 2.2, as the learning is repeated over time, the filter is then updated for the upcoming input data (Marais & Aldrich, 2011). Updating of the filter uses a method called ‘stochastic gradient descent’ which is often referred to as backpropagation.

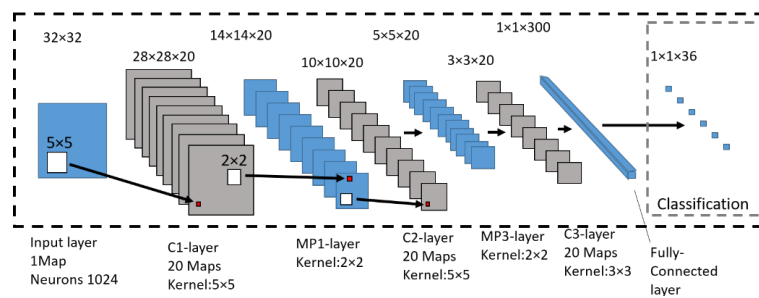


Figure 2.1: Typical representation of feature extraction from a 2D CNN with convolution and maximum pooling layers (C1-3 and MP1-2 respectively). The main CNN layers are input layer, hidden layer and output layer.

Figure 2.1 and 2.2 further highlight the other important layer housed within the hidden layer namely the ‘maximum pooling layer’, this layer’s focus is to compress localized feature extractions Poria et al. (2016). Zhang et al. (2017) state that within the maximum pooling layers, selection of the maximum value for the feature map is performed, this process reduces the number of units, thereby lowering the computational cost, lowering the sensitivity of minute

changes, and suppressing overfitting in the feature map. At the end of the network, exists the third main layer namely the output layer, it gathers information from the fully connected layer and is where results pertaining to the performance of the network are presented.

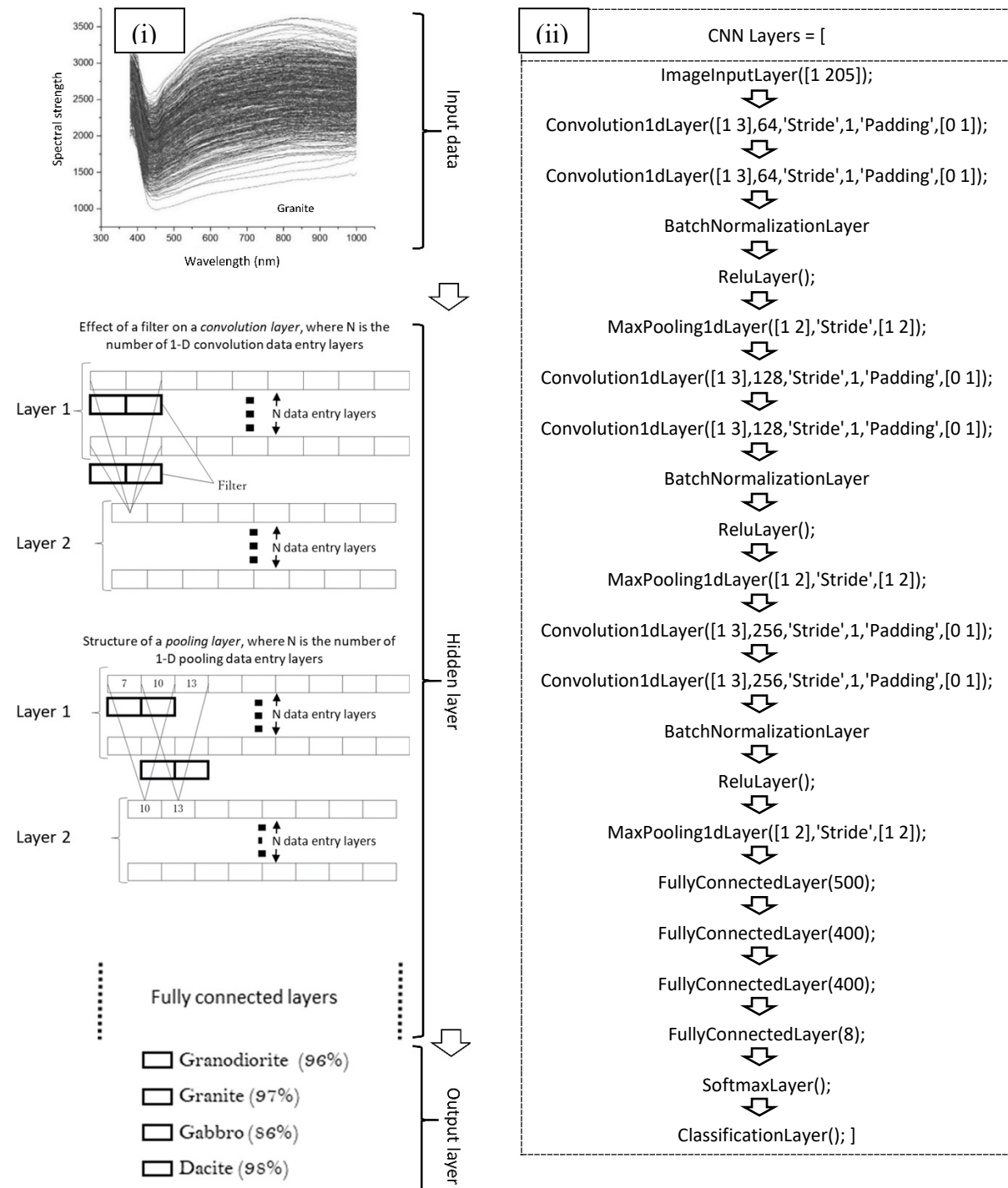


Figure 2.2: Simplified (i) and true (ii) structure of the 1D CNN with input, hidden and output layers.

2.3. Practical Experiments

2.3.1. *Capturing Rock Hyperspectral Signatures*

To craft this proposed system, experimental work was carried out using pre-evaluated and labelled rock samples collected from various unrelated outcrops, which are specimens registered in the ‘Mineral Industry Museum, Akita University’. For data acquisition, the selected 32 igneous rock samples from eight rock lithologies, four being of plutonic origin (granite, diorite, gabbro and granodiorite), and the other four of volcanic origin (andesite, dacite, basalt and rhyolite), were used. According to researchers (Sinaice et al., 2020; Carrino et al., 2018; Burley et al., 2017), Figures 2.3(i) and 2.3(ii) are classification diagrams of how the geology community typically distinguishes these rocks with the naked eye (plutonic rocks) or chemical analysis (volcanic rocks). The complexity of these methods is what drove this study to propose hyperspectral imaging as a method in which representative features of these rocks whose areas have been shaded in Figure 2.3 can be extracted and later predicted and classified.

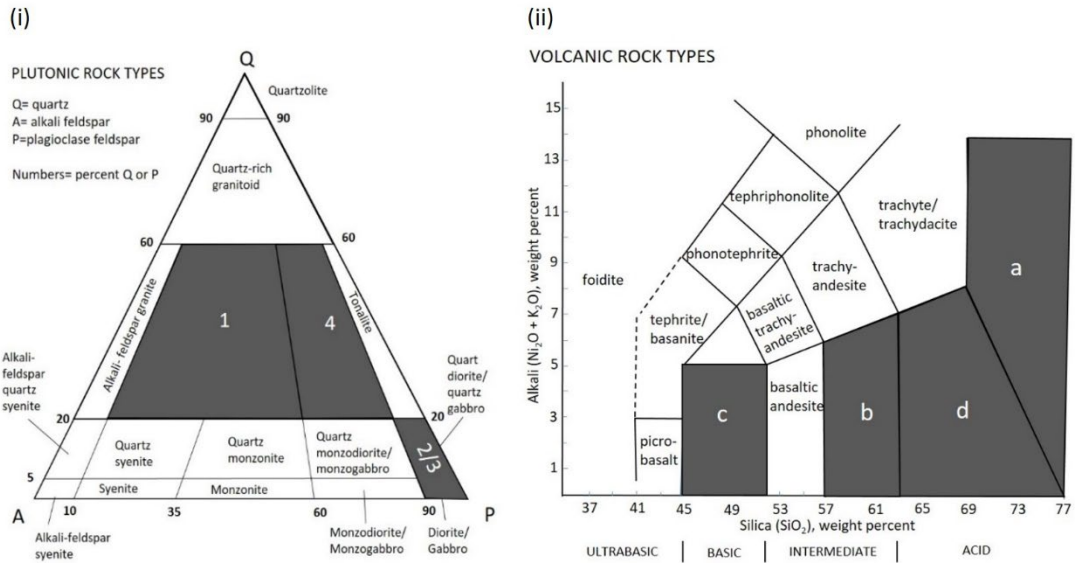


Figure 2.3: Classification diagrams showing the plutonic (i) and volcanic (ii) rocks which were of interest for this study to be carried out: (1) granite (2) diorite (3) gabbro (4) granodiorite (a) rhyolite (b) andesite (c) basalt (d) dacite.

To capture their spectral signatures, a Specim IQ hyperspectral camera with VNIR range capabilities (400–1000 nm, 204 bands) was used to record the pixel-by-pixel signatures of the rocks. The main components of the spectral data extraction setup are illustrated in Figure 2.4. As van der Meer (2006) has pointed out, gathering this data entails standardising the spectral signature recording process. This was done by initialising the camera with a white reference board (provided by the manufacturer, Specim), the purpose of which is to filter out the noise and verify subsequent data is recorded under the same standardised conditions. The experimental setup utilises tungsten-halogen lamps to illuminate the stage as they have high output capabilities throughout the VNIR, which coincides with the camera capturing range. Figure 2.5 is a collection of some of the 32 rock samples from eight rock lithologies used in this study to build a rock hyperspectral database.

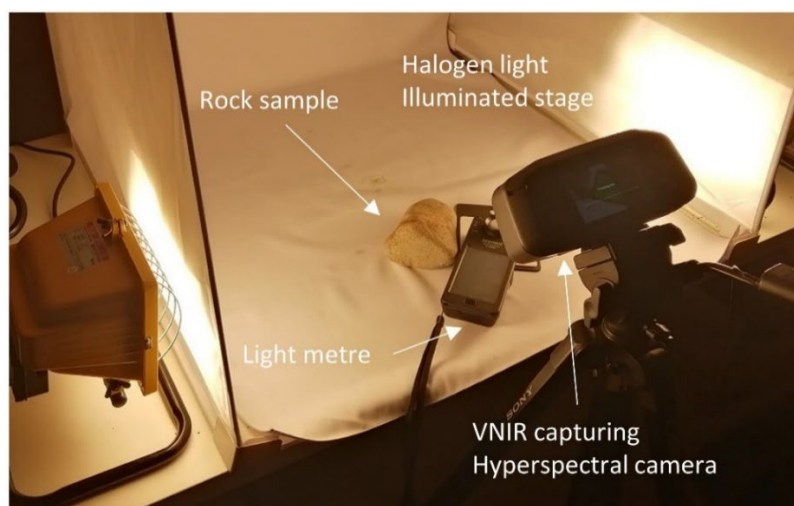


Figure 2.4: Experimental set-up showing the main components of Visible-NIR hyperspectral imaging system. The camera extracts data and sends it straight to the computer system where data can then be used for various kinds of analysis.

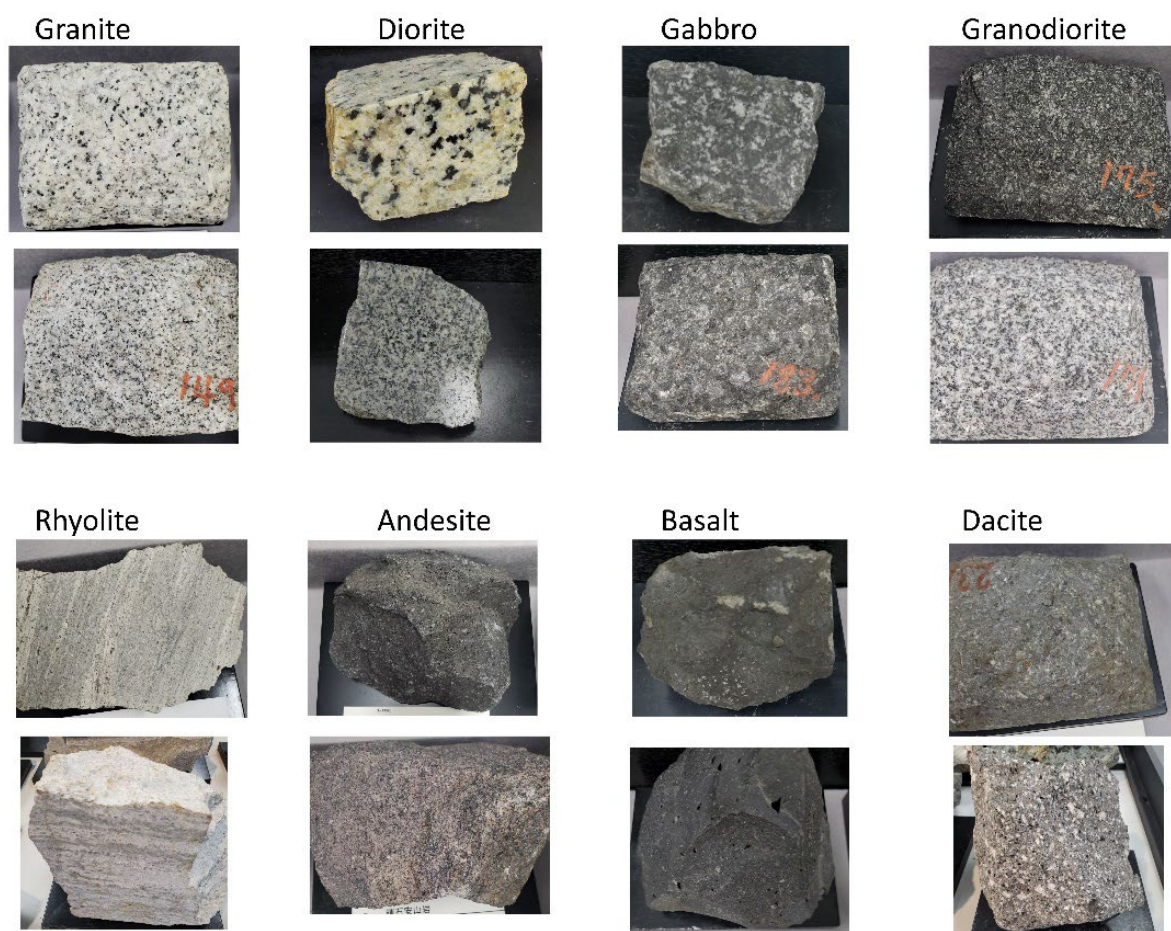


Figure 2.5: Images of some of the 32 rock samples from eight rock lithologies used in building the rock hyperspectral database.

Having captured the depth possessing, high dimensionality hyperspectral imagery data of all rocks, this data is then converted to numerical data using hyperspectral analysing software such as python. Converting to numerical data entails the extraction of spectra from specific pixel blocks. This is performed after having assigned a data extraction area to allow automatic selection of pixel blocks with spectra to be considered for analysis (Figure 2.6). Since the Specim IQ camera acquires images of 512×512 pixels from 204 bands, the software randomly and automatically extracts 20×20 -pixel information from these 204 band images (Figures 2.6). Meaning, that each spectrum is an average of the spectral reflectance information from a 20×20 -pixels (400 pixels) area; hence, each block becomes an average spectral strength with a depth of 204 bands (wavelength). The selection area boundaries are set by the user to ensure the software extracts only relevant data.

To extract 100% of the captured image spatial area of the 512×512 pixels = 262,144 total pixels, a total of approximately 655 spectra (the exact number is 655.36 pixels), each with a spatial area of 20×20 pixels = 400 pixels would have to be extracted. This is derived from dividing 262,144 pixels by 400 pixels to get 655. However, since the spectral extractor used in this study extracts 220 pixels per image, this results in approximately 30% [$262,144 / (220 \times 400)$] of the image area being used for analysis. This 30% (made up of 220 spectra minus manual elimination of non-rock spectra) of the extracted whole image area, however, can be placed anywhere on the image area using the spectral extraction boundary controlled by the user. Therefore, should a perfect 88,000 pixels ($220 \times 20 \times 20$) area be defined by the user, 100% of the selected rock spectral information without background noise would be extracted. However, this was not the case in this study, as the extraction boundaries were randomly set judging from the area in which actual rock resides within each image.

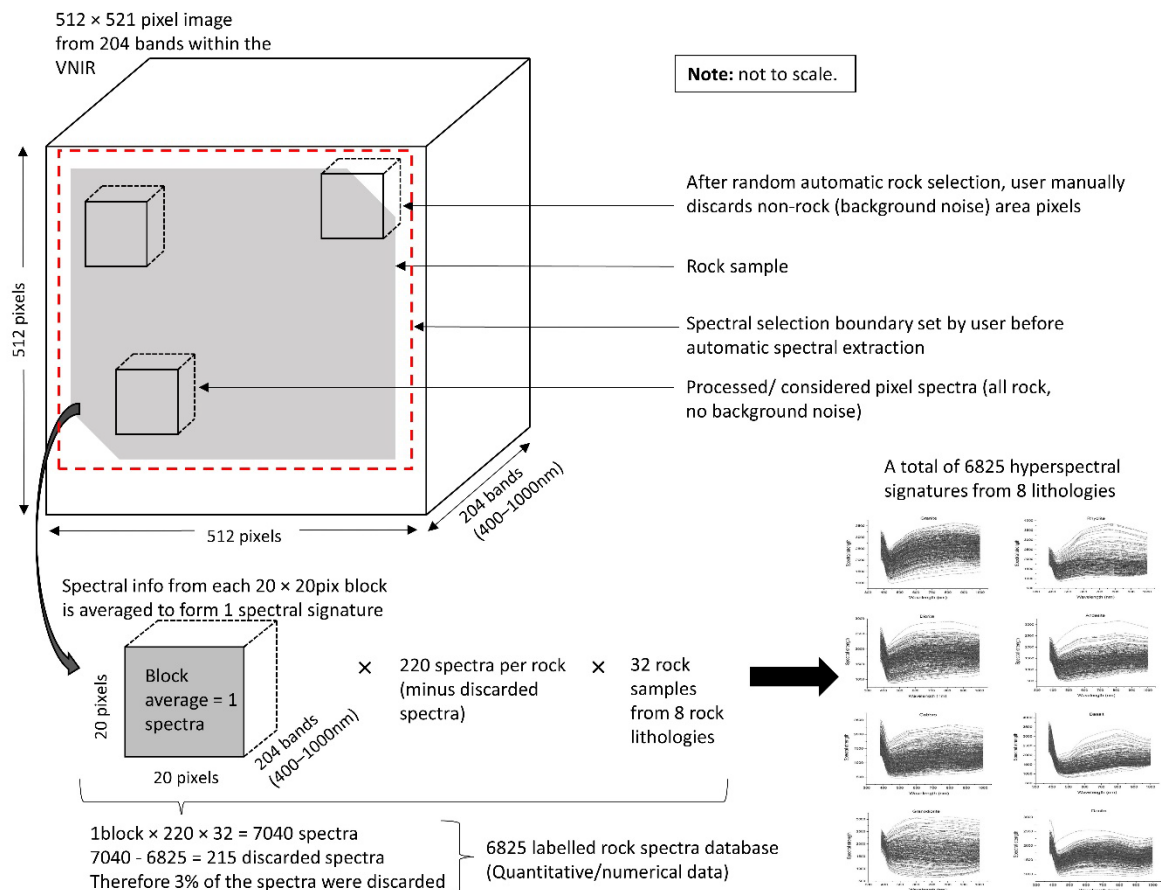


Figure 2.6: Automatic random extraction of rock pixel spectra captured via a Specim IQ camera that acquires 512×512 pixel images from 204 bands within the visible-near-infrared range. Extracted spectra are used to build a rock hyperspectral database.

Performing manual elimination (by the user) of unwanted spectra from the automatically extracted (by the software) 220 results in a lesser number of extracted spectra than the initial 220. As a result, from the 32 rock samples, we now have a total of 6825 [(220 spectra × 32 samples) minus unwanted background noise] viable representative spectra from eight rock lithologies, each with a 204-band depth having been extracted for analysis. This, in essence, means the quantitative dataset has a matrix of size $204 \times 6825 = 1,392,300$ spectral information, which is used as input data in subsequent procedures. This data goes through a pre-processing stage where each dataset is assigned a relevant label; hence, a hyperspectral rock database was built based on the eight igneous rock lithologies. It should be noted that this

process can be performed on any rocks, minerals or the combination of which. The choice or type of data used to develop a database depends entirely on the purpose upon which rock or mineral classification is intended to be based. This, as a result, enables the AI coupled system to be highly specialised in classifying that which is within or related to the database.

2.3.2. Data Pre-processing

Having formed a rock hyperspectral signature database, Figure 2.7 shows the next important step in data pre-processing before training the 1D CNN. This stage involves assigning the 1D CNN to randomly select 80% of the total data and treat it as training data. This is called the learning process.

The next vital step is to set the 1D CNN to randomly select the remaining 50% (10% of the total) of data and treat it as validation data. This data has the same data labels as the training data, its function is to verify if indeed the system has gained knowledge and the ability to recognize similarities and differences in data it had been previously subjected to (training data).

Finally, the last 10% of the data omitted in the validation and training processes are then treated as testing data. This data functions as a dataset used to challenge the 1D CNN and find out its classification capabilities. In this testing process, the CNN is expected to recognize and classify data based on the knowledge it has gained in assessing patterns and tendencies in the previously mentioned training and validation processes. Figure 2.7 is a visualization that highlights the data pre-processing process and how the data is randomly assigned to the training, validation and testing processes.

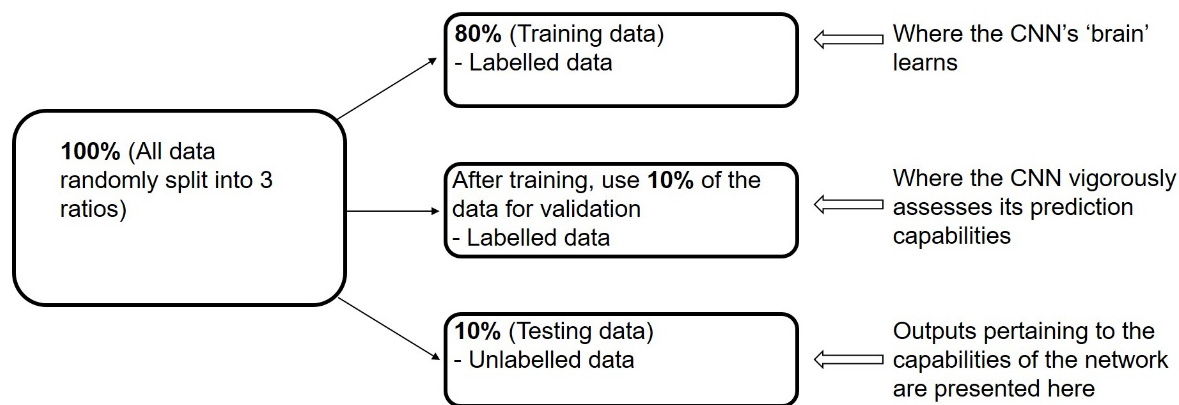


Figure 2.7: Representation of how the data was handled during the training and testing processes (data pre-processing).

2.4. Experimental and Analytical Results

2.4.1. Findings Based on Hyperspectral Imaging

Conversional hyperspectral signatures are usually presented as single line anomalies with specific reflectance values across the entire spectral range as presented in sections 2.4.1.1 and 2.4.1.2 for each hyperspectral image. However, this study believes this way of representing them tends to assume rocks exist as end-member variables, which in nature, is not true as rocks exist as variations across different end member variables. This is why this study also presents section 2.4.1.3 where rock spectral signatures are denoted as as per image partitions, hence every variation within each rock is accounted for by its own spectral signature. Such a representation in turn allows extraction of the most data, thus aiding the 1D CNN to recognize each variation which may exist within each rock (Li et al., 2017), therefore, making predictions made by the CNN vaster and more precise.

2.4.1.1. Hyperspectral signatures as image mean anomalies

According to Debba et al. (2005), if one's purpose is solely to obtain and analyse hyperspectral rock signatures visually, converting or averaging the previously illustrated

(Figure 2.6) image partition hyperspectral signatures into one anomaly is a viable way of doing so (Figure 2.8). Though effective to a certain extent, this way of obtaining hyperspectral signatures of rocks does not feed enough data to the 1D CNN as it requires multitudes of data in order to learn different possible permutations (Shugao et al., 2017) a single rock may have from having captured a single hyperspectral image of that rock. The reason for pointing this out is because in nature, rocks do not always exist as endmember constituents but rather as variations between two or more endmembers (Meer et al., 2012). Figure 2.8 is a representation of rock hyperspectral signatures given as mean representative anomalies of each rock. From these, one can easily differentiate the rocks, based on the amount of tilt, reflectance strength peaks, and band shapes (Satadru et al., 2011). As a general trend, the volcanic rock counterparts seem to possess a higher spectral reflectance as compared to their plutonic counterparts.

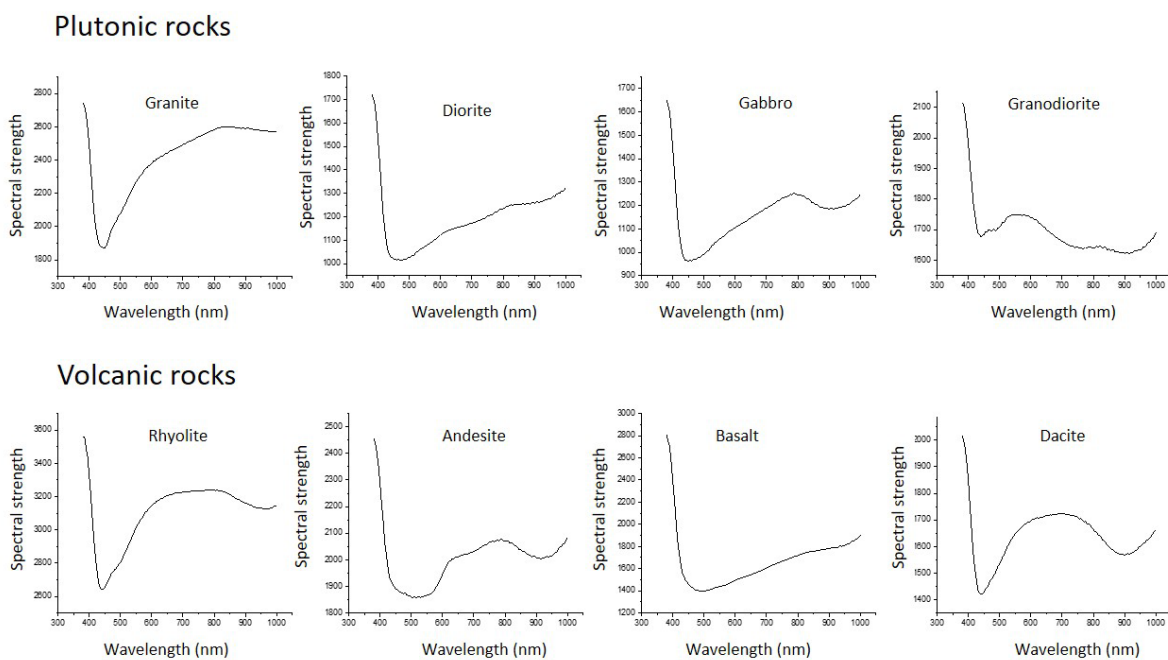


Figure 2.8: Hyperspectral signatures of rocks as whole image average anomalies.

2.4.1.2. Compilation of all average rock hyperspectral signatures

To compare section 2.4.1.1 rock hyperspectral signatures, one may be required to do a compilation of all the above mentioned average rock hyperspectral signatures (Figure 2.8) into

one (Pieters et al., 2009). As Figure 2.9 shows, rhyolite has the overall highest spectral reflectance strength, followed by granite, and andesite, across the entire VNIR range. The rest of the rocks (basalt, granodiorite, dacite, diorite and gabbro), seem to switch positions from 450~630 nm, 630~830 nm, and lastly from 830~1000 nm, the reason being, that these rocks interact with electromagnetic radiation differently across different ranges (Zhang & Li, 2014). For this reason, this was an anticipated trend.

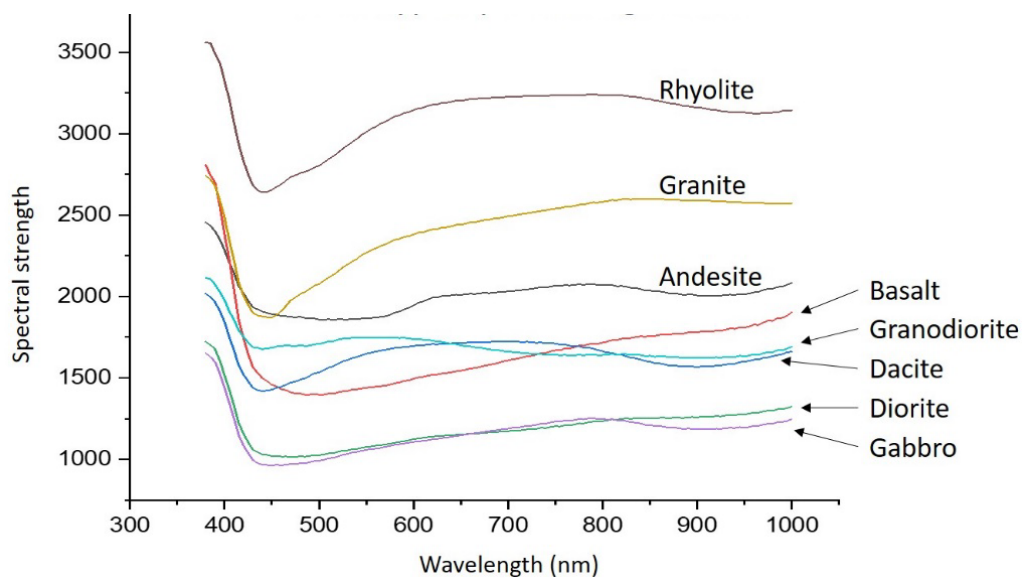


Figure 2.9: All rock hyperspectral signatures as per rock image averages.

2.4.1.3. Hyperspectral signatures at pixel level anomalies

As a way of visualising the characteristic rock and light interactions at a pixel level from within the VNIR range, Figure 2.10 hyperspectral signatures are typical illustrations used to visualise these inherent reflectance signatures. Each anomaly represents a given 20×20 pixels block as an average spectral reflectance strength from the image scene. Based on Figure 2.10, one can appreciate the differences in spectral reflectance strength signatures attainable from different pixels within the same hyperspectral image. Moreover, the way different rock sample variants of the same rock exhibit different signatures combined to form hyperspectral signatures, hence, each of the eight rock lithologies shows dispersed hyperspectral signatures.

Taylor (2000) employed VNIR spectroscopy on their ‘Mineral and Lithology Mapping of Drill Core Pulps’ problem and concluded that spectrometry, like XRD, provides an evaluation of quantitative mineralogy that is very reliable. Hence, we are confident hyperspectral imaging is very useful in our rock identification problem, as has been hypothesised. We see these inherent differences in the spectral signatures exhibited by the rocks in our database (Figure 2.10).

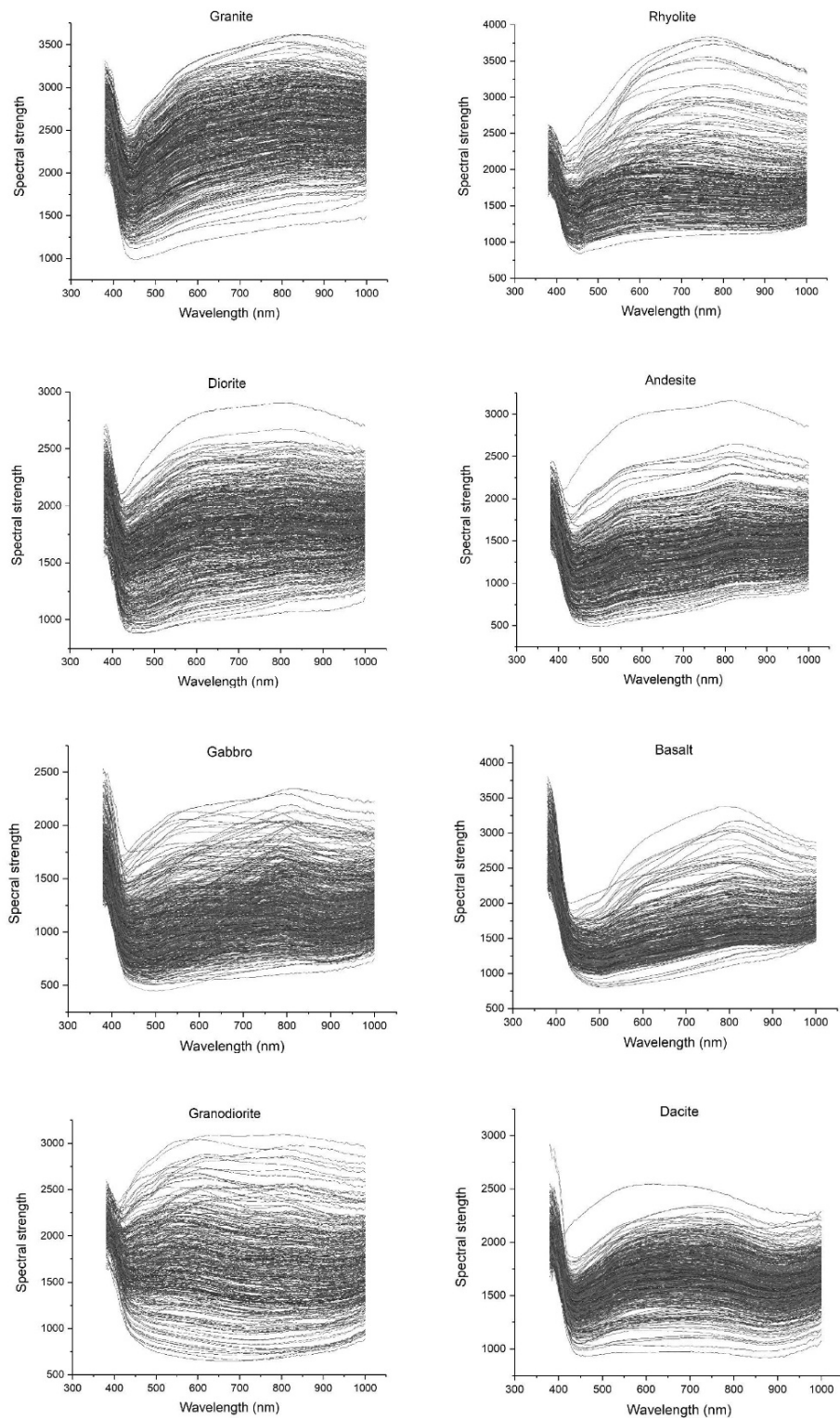


Figure 2.10: Reflectance hyperspectral signatures of eight rock lithologies employed in the construction of a hyperspectral database. Each anomaly represents the interaction between each 20×20 pixels 2D area with a depth of 204 bands within a rock's hyperspectral image with light, captured via a Visible-Near-Infrared-Range hyperspectral camera.

Patterns can be drawn from hyperspectral signatures, enabling one to distinguish individual rocks and/or minerals (Bhattacharya et al., 2011). However, it is difficult to extract a certain anomaly from each of the eight hyperspectral rock signatures and deem it the most representative spectral signature of a particular rock and/or mineral. This can be said when for example, examining the general spectral patterns of granite with those of diorite. Their anomaly shapes seem rather similar in terms of resembling ‘check marks’, with some of them displaying comparable reflectance intensities even; the same can be said when comparing gabbro signatures with those of andesite (Figure 2.10). Having seen the advantages and disadvantages of hyperspectral signatures employed as a means for rock and/or mineral classification, one can acknowledge that there is a need to employ a method by which these anomalies may be objectively and quantitatively analysed. This would allow for better comparisons and distinguishability of rocks and/or minerals via their hyperspectral signatures, which is what the 1D CNN will be set to improve.

2.4.2. Rock 1D CNN Prediction and Classification

Three 1D CNNs were set out to perform 3 vital tasks, training and classifying plutonic rocks (task 1), training and classifying volcanic rocks (task 2), and lastly, training and classifying all igneous rocks (task3). From what the results of the training and validation processes were able to present, all three 1D CNNs were indeed able to classify rocks accordingly with high accuracy and precision ratings (Figure 2.11, 2.12 and 2.13). For a CNN to be referred to as accurate and robust at making predictions, there are a number of prerequisites to satisfy. First, validation accuracy results after the training process has been performed need to be high, which in this study was achieved as the 1D CNNs had a prediction accuracy of 88.2% for plutonic rocks, 74.3% for volcanic rocks, and 96.4% for all igneous rocks. These high percentages communicate the prediction capabilities of the three 1D CNNs (Peng et al., 2017). Hence making it viable for rock discrimination from hyperspectral images.

As a general observation, the 1D CNN classifying all eight igneous rocks outperformed the CNNs whose tasks were to classify plutonic and volcanic rocks only, which is not surprising as the larger a dataset is, the better the classification accuracies.

The second vital variable communicated by the 1D CNN training progress is the cross-entropy loss function plot (Figure 2.11, 2.12 and 2.13), which is defined as a measure of the difference between two probability distributions for a given random variable or set of events. Therefore, with more information, the lower the probability event, which could be thought of as surprising, whereas, the lesser the information, the higher the probability event, which could be thought of as unsurprising. This plot shows the state of the CNN in the sense that it maps out the cumulative number of times in which the CNN was unable to obtain correct answers during validation (Portia et al., 2016). It is presented as a cumulative relationship as it shows how the number of training steps employed during training relates to the number of times the CNN gains familiarity with the data presented to it, hence, like a brain, with more training steps or iterations involved in training the network, the more accurate the network becomes at predicting and classifying data accordingly. Another aspect presented by the loss function plot is how robust the CNN is. The robustness of a CNN dictates how stable the entire network is when making predictions from the point data is imported into the system, through the multiple hidden layers, to the output layer (Shugao et al., 2017). This is shown by how quick the CNN loss function graph reaches and maintains a low loss value from the time the network commences the training process, till it is completed.

However, it should be noted that both validation and loss functions can be improved at any time via hyperparameter tuning, by defining the number of iterations the network is to run, and the amount of data the network runs per iteration (batch number). This offers the flexibility to improve the network as more data is introduced into the CNN for database expansion or

further classification (Landgrebe, 1999) of unknown rocks; and predicting what they may most likely to be based on the already learnt data in the database.

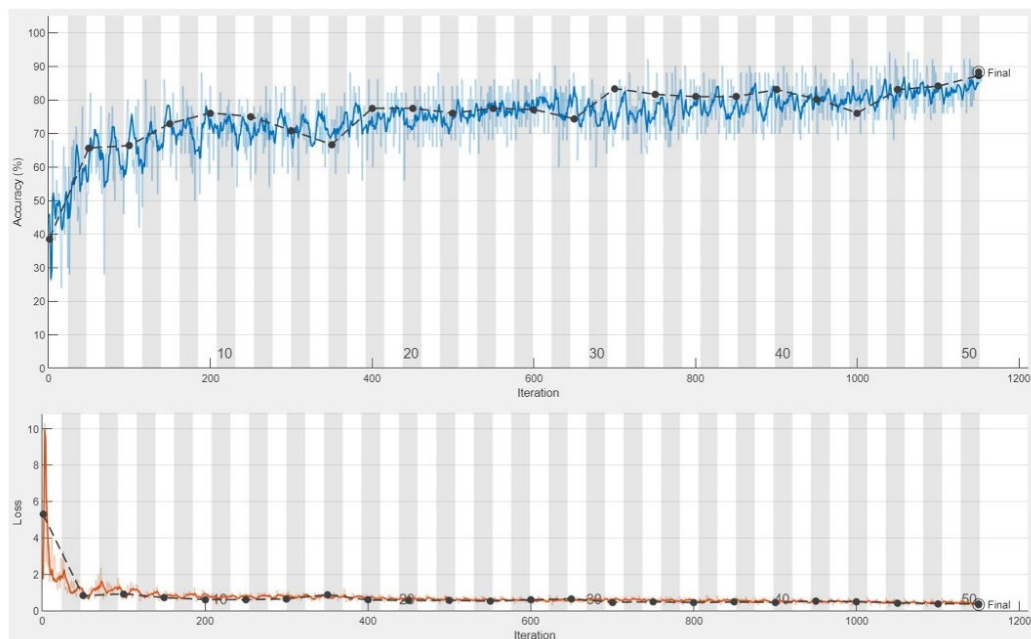


Figure 2.11: Plutonic rocks training progress showing a high validation accuracy of 88.2 % and a low loss function plot.

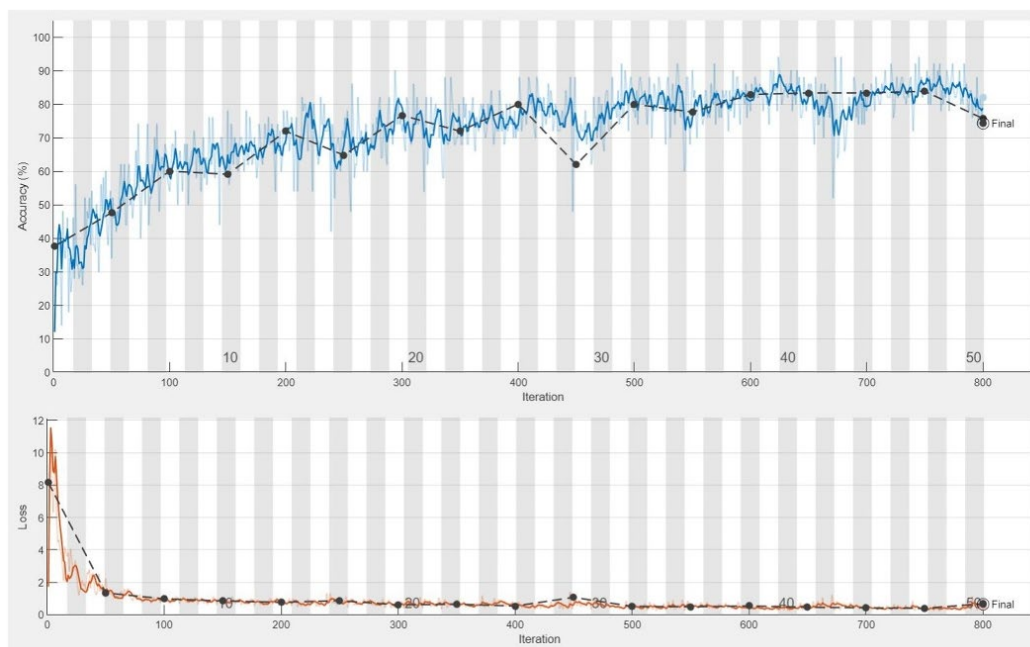


Figure 2.12: Volcanic rocks training progress showing a high validation accuracy of 74.3% and low loss function plot.

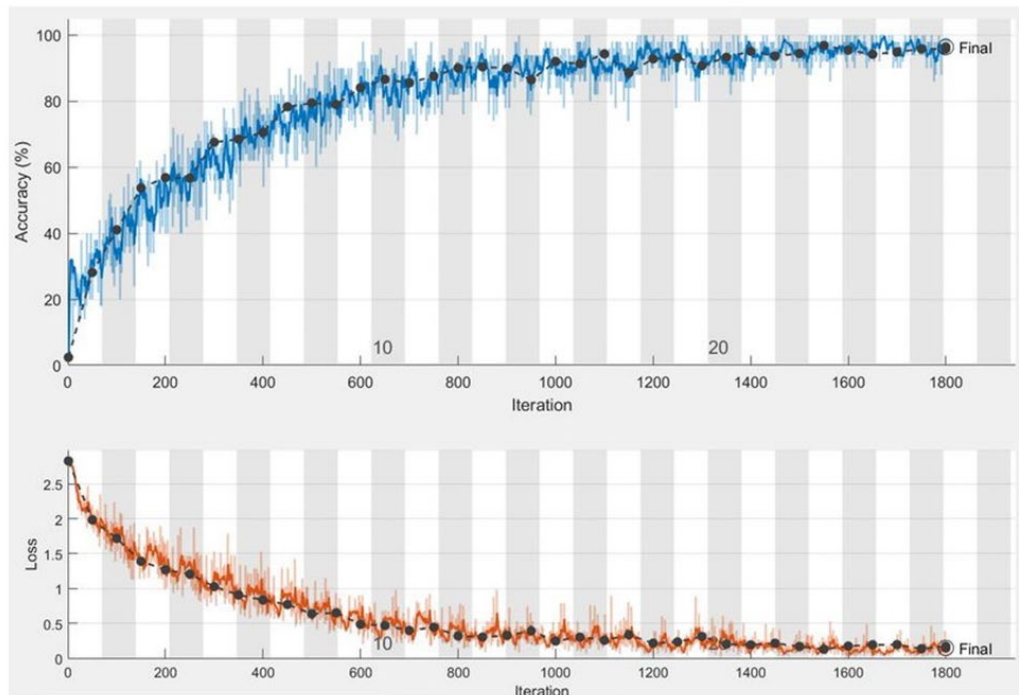


Figure 2.13: Igneous rocks training progress showing a high validation accuracy of 96.4 % and low loss function plot.

Having established that the networks are indeed robust and highly capable of making high accuracy predictions from the hyperspectral igneous rock images, one is now able to read in detail the results presented by the 1D CNN models. With a focus on the plutonic rock, volcanic rock all eight igneous rock 1D CNN model confusion matrix results, the CNNs were able to classify plutonic rocks with an average per-class precision of 89.1%, as well as 82.6% for the CNN model responsible for classifying the volcanic rocks. Lastly, the igneous rocks' average per-class precision was 87.9%. Based on these outputs, the plutonic rock CNN model outperforms the other two models, which could be attributed to their crystal sizes as these rocks formed below the earth's surface. These confusion matrix output values are obtained from the previously mentioned testing process. The network attempts to match unknown or unlabelled data with what it has learnt during the training and validation processes, these results show the true and more detailed prediction precision capabilities of the CNN at distinguishing individual plutonic rocks amongst other plutonic rocks (Figure 2.14), individual volcanic rocks amongst

other volcanic rocks (Figure 2.15), as well as individual igneous rock among our igneous rocks (Figure 2.16).

To further assess the viability of the performances of the three 1D CNNs in classifying plutonic, volcanic and igneous rocks, Figures 2.14, 2.15 and 2.16 respectively, present two performance metrics. The first is True Positive Rates (TPR), defined as the probability that an actual positive will test positive (Equation 1). The second is False Negative Rates (FNR), defined as the probability that a true positive will be missed by the test (Equation 2). Both variables are highly viable in assessing the capability of the 1D CNNs.

True Positive Rates (TPR):

$$TPR = 100 \left(\frac{TP}{TP+FN} \right) \quad (1)$$

False Negative Rates (FNR):

$$FNR = 100 \left(\frac{FN}{TP+FN} \right) \quad (2)$$

where FN is false negatives and TP is true positives.

For plutonic rocks only (Figure 2.14), the 1D CNN has an average per-class precision (TPR) of 89.1%, with gabbro prediction being the highest performance as TPR of 95.6% and the least with granodiorite at TPR of 84.3%.

For volcanic rocks only (Figure 2.15), the 1D CNN has an average per-class precision (TPR) of 82.6%, with dacite prediction being the highest performance as TPR of 100% and the least with basalt at a TPR of 65.5%. Based on Figure 2.3(ii), the low basalt prediction could be attributed to the chemical differences existing between basalt and the other volcanic rocks, which could have influenced the 1D CNN to give more priority to the other volcanic rocks when training and outputting the model, hence the results.

For all eight igneous rocks (Figure 2.16), the 1D CNN has an average per-class precision (TPR) of 87.7%, with granodiorite and gabbro predictions being the highest performance as TPR of 97.7%, which is significantly higher than the previous 84.3% (Figure 2.14) from having trained the CNN with input data being only plutonic rocks. In addition, the least prediction capability was attained in classifying dacite at a TPR of 78%. Based on Figure 2.9, this could be attributed to the manner in which the dacite spectral anomalies possess a trend unlike the other rock, which could have meant the 1D CNN algorithm gave it less priority in developing a final model to classify all eight igneous rocks. From these quantitative assessments, one can appreciate the extent to which a DL 1D CNN such as the ones employed in this study can be used to objectively classify rocks based on their hyperspectral signatures. Table 2.1 is a summary of all three 1D CNNs model capabilities.

True class	Diorite	84.3%	7%	2.6%	6.1%	84.3%	15.7%
	Gabbro	4.4%	95.6%	0%	0%	95.6%	4.4%
	Granite	4.1%	0%	93.2%	2.7%	93.2%	6.8%
	Granodiorite	11.1%	5.6%	0%	83.3%	83.3%	16.7%
		Diorite	Gabbro	Granite	Granodiorite	TPR	FNR
Predicted class							

Figure 2.14: Post training plutonic rocks confusion matrix.

True class	Andesite	96%	0%	4%	0%	96%	4%
	Basalt	23.3%	65.5%	5.2%	6%	65.5%	34.5%
	Dacite	0%	0%	100%	0%	100%	0%
	Rhyolite	7.1%	4.8%	19.1%	69%	69%	31%
		Andesite	Basalt	Dacite	Rhyolite	TPR	FNR
Predicted class							

Figure 2.15: Post training volcanic rocks confusion matrix.

True class	Andesite	97.4%	0%	0%	2.7%	0%	0%	2.7%	0%	94.9%	5.1%
	Basalt	14.3%	81.3%	1.1%	2.2%	1.1%	0%	0%	0%	81.3%	18.7%
	Dacite	0%	2%	78%	2%	0%	4%	8%	6%	78%	22%
	Diorite	1.7%	0.9%	0%	84%	6.7%	4.2%	2.5%	0%	84%	16%
	Gabbro	0%	0%	0%	2.3%	97.7%	0%	0%	0%	97.7%	2.3%
	Granite	0%	0%	0%	4.1%	0%	90.3%	2.8%	2.8%	90.3%	9.7%
	Granodiorite	0%	0%	0%	0%	2.3%	0%	97.7%	0%	97.7%	2.3%
	Rhyolite	5.1%	5.1%	5.1%	0%	2.6%	0%	2.6%	79.5%	79.5%	20.5%
		Andesite	Basalt	Dacite	Diorite	Gabbro	Granite	Granodiorite	Rhyolite	TPR	FNR
		Predicted class									

Figure 2.16: Post training igneous rocks confusion matrix.

Table 2.1: Results of the deep learning data, acquired from the hyperspectral signatures of the plutonic and volcanic rocks.

Input dataset	Global accuracy (%)	Average per-class precision (%)	Training time (minutes : seconds)
Plutonic rocks	88.2	89.1	1 : 25
Volcanic rocks	74.3	82.6	2 : 06
All 8 igneous rocks	96.4	87.9	25 : 43

2.5. Discussion

Figure 2.17 and 2.18 are summarized comparisons between the three 1D CNN model classification capabilities in terms of global accuracy and average per-class precision, as well as individual rock TPRs respectively. Based on Figure 2.17, the 1D CNN responsible for the classification of plutonic rocks only is the best performer followed by the CNN tasked with classifying all eight igneous rocks, and the least performer being the volcanic rock CNN model. the CNN models perform better than the ML models across all 3 flight elevations.

Based on Figure 2.18, if one's goal is to find the best 1D CNN model to classify individual rocks within this database based on their hyperspectral signatures, the best models would be as follows:

- andesite, 96% with the plutonic rocks 1D CNN model,
- basalt, 81.3% with the all igneous rocks 1D CNN model,
- dacite, 100% with the volcanic rocks 1D CNN model,
- diorite, 84.3% with the plutonic rocks 1D CNN model,
- gabbro, 97.7% with the all igneous rocks 1D CNN model,
- granite, 93.2% with the plutonic rocks 1D CNN model,
- granodiorite, 97.7% with the all igneous rocks 1D CNN model,
- rhyolite, 79.5% with the all igneous rocks 1D CNN model.

Overall, the eight igneous rocks 1D CNN performs better in classifying most of the rocks as compared to classification via the plutonic and volcanic rocks 1D CNN models. This could be attributed to the large size of the dataset used to train this model, hence confirming the previous statement that states, that the larger the data, the better the deep learning classification capabilities.

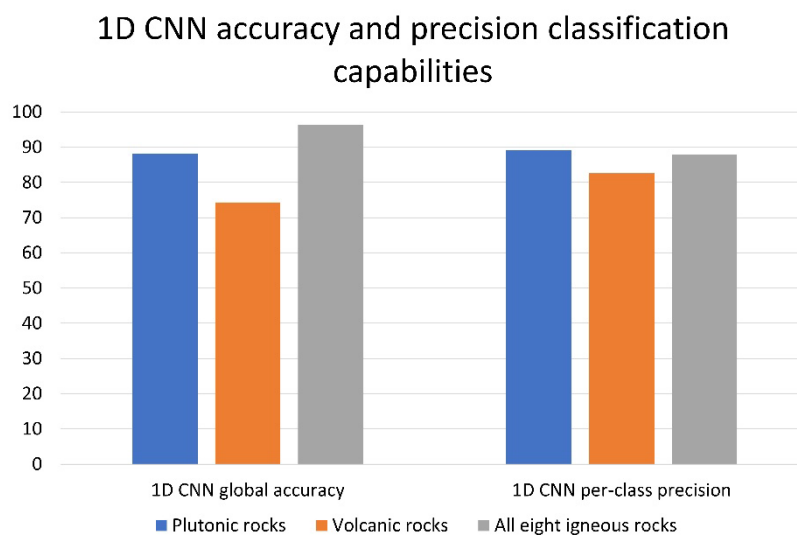


Figure 2.17: Post training global accuracy and average per-class classification capability comparisons.

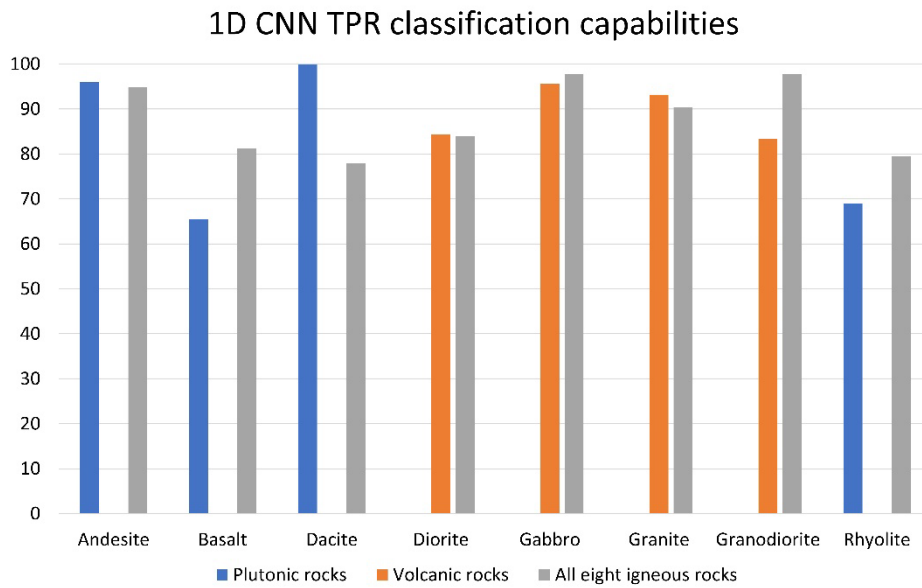


Figure 2.18: Post training model comparisons per rock in the database.

As a recap, the results suggest that indeed the deep learning CNN system is capable of separating or distinguishing rocks based on their hyperspectral signatures as demonstrated by the employed closely related plutonic and volcanic rocks. This is supported by the high classification output percentages which suggest high levels of feature recognition post network training. With further improvements such as the input of more data and the continuous tweaking of the network algorithm to improve output results, the use of hyperspectral signatures of rocks together with deep learning CNNs can potentially be a viable and technologically advanced way in which rock classification and identification can be carried out. With that said, the advantage of employing hyperspectral imaging and a 1D CNN for rock discrimination as demonstrated can be listed as;

- database creation with the option of continued future expansion,
- high discrimination capabilities with minimal error,
- the option of network improvement as more data is imported, and
- viability for employment in any rock engineering works that require such capabilities.

2.6. Conclusion

It can therefore be concluded that the combination of hyperspectral imaging of rocks with deep learning into one system, is a viable way in which future industries could base their rock discrimination and/or prediction problems. This study has demonstrated this by creating robust and highly accurate systems with network accuracy values of 88.2%, 74.3% and 96.4% for plutonic, volcanic and eight igneous rocks within the hyperspectral database respectively. With the option of database expansion and network upgrading with every data imported, this integrated system makes more sense in this digital world where every action is data intensive and requires low or minimal error for every processing action performed.

Having analysed and interpreted the spectral signatures of the rocks and quantified the results in terms of how much spectral recognition the system is able to detect, it is safe to come to the deduction that indeed hyperspectral signatures of rocks are a viable method in which rock delineation based solely on the amount of light they reflect across a given spectral range and bands and a highly capable DL 1D CNN can be performed. This is moreover supported by the exceptional prediction precision capabilities the 1D CNNs were able to attain; where plutonic, volcanic and all eight igneous rock predictions were 89.1%, 82.6% and 87.9% respectively.

In short, the main advantages of deep learning are as follows; less complicated feature representation from raw pixels, large-scale learning, and the ability to set desired parameters within the deep learning algorithms. With the above said, hyperspectral imaging and CNN based deep learning methods combine to form a state-of-the-art, feature and parameter learning technique which is worthy to be employed in any mining, rock or geological engineering work that depends on fast, accurate and overall efficient rock classification techniques of the 'computer age'.

CHAPTER 3: Coupled with Machine Learning, Achieving Specialized Rock Multispectral Imaging via Dimensionality Reduction from Hyperspectral Imaging

In an attempt to classify rocks based on their hyperspectral signatures as well as deep learning models as presented in Chapter 2, the following limitations in the methodology were realised: Hyperspectral signature processing requires high-grade computational resources; hyperspectral signature processing subjects one to analysing redundant feature bands; deep learning algorithms require a large magnitude of data in order to perform accurate pattern recognition. Therefore, this chapter assesses the dimensionality reduction of 204 hyperspectral imaging bands via Neighbourhood Component Analysis, to 5 specialized multispectral bands. Quantitative system capabilities are presented via machine learning models.

3.1. Introduction

Though the hundreds of spectral bands in hyperspectral imaging provide a multitude of highly detailed data (Galdames et al., 2019), this data suffers from what is referred to as the ‘dimensionality curse’. This is defined as the inability to visualise such depth possessing data structures (Ruiz Hidalgo et al., 2020). Moreover, Tong et al. (2017), highlight that though deep neural networks acquire high accuracy results, executing them is computationally costly and time-consuming, deeming them highly difficult to employ in rapid on-site investigations (Sinaice et al., 2020). To counter these shortcomings, this paper is a proposal whose attempt is to improve the application of rock spectral imaging by converting from hyperspectral imaging to multispectral imaging (Sharma et al 2021), this will be performed through dimensionality reduction (DR) via Neighbourhood Component Analysis (NCA). Lastly, employing different

Machine Learning (ML) models whose purpose is to access the attainable rock discrimination capabilities based on the NCA selected bands.

Other than this, with NCA, engineers should hypothetically be able to convert from using highly detailed hyperspectral data together with its often-redundant datasets (Goldberger et al., 2004), to using more specialised multispectral datasets. This specialisation can be set such that the multispectral bands focus on detecting specific phenomena, these being specific rocks, minerals, ores, tailings, dam metal contaminants, and more. Moreover, NCA can be used in determining the most important criteria (Venna, 2021) in mining, ore processing, quarrying, geological, and geotechnical assessments. This is through assigning feature weights (Venna, 2021) to datasets, such as rock hardness, presence of clay minerals, weathering intensity and water content, amongst others. These weights consequently allow for the elimination of redundant data based on the intended applications of such data (Saha and Annamalai, 2021).

Having determined the specific bands viable to discriminate a certain rock and/or mineral database, or equivalent via NCA, the selected features or multispectral bands can be accessed via various machine learning (ML) models to determine the distinguishing capabilities of such models. Their performances are usually judged based time required to train, global accuracies and sub-class precisions (Salles et al., 2017; Kruze, 2012). Thereafter, engineers should potentially be able to commission the construction of a multispectral sensing device built using the best performing ML model. Consequently, making this integrated system a novel method in which specific rocks, minerals and other phenomena can be classified via a specialised multispectral sensor. Advantages of such would include improved remote sensing, which in turn improves workplace safety, traceability of data and results, and the overall optimisation of the classification system. As one can imagine, our proposed method is not only limited to mining industry applications, and it has the potential to be employed in multitudes of other industries, such as in agriculture, forensics, biology, and banking, among others.

To understand the technicalities of this proposed integrated system (Figure 3.1), we will explain each of these technologies and how they have been previously applied by other researchers in Section 2. Having defined the ideal number of spectral bands whose position within the electromagnetic spectrum will be determined by NCA, these said bands can potentially be employed in multiple areas within the mining industry. One of such potential applications is the development of 5-band-multispectral sensing cameras mountable on unmanned aerial vehicle (UAV) drones because current industry standards for in-situ classifications related to the state of the environment are usually limited to 5-bands. Therefore, our paper will aim to satisfy the current 5-band multispectral production camera and drone trends, yet still demonstrate the different ways in which this integrated system can be taken advantage of in mining, rock and mineral engineering industries and/or studies.

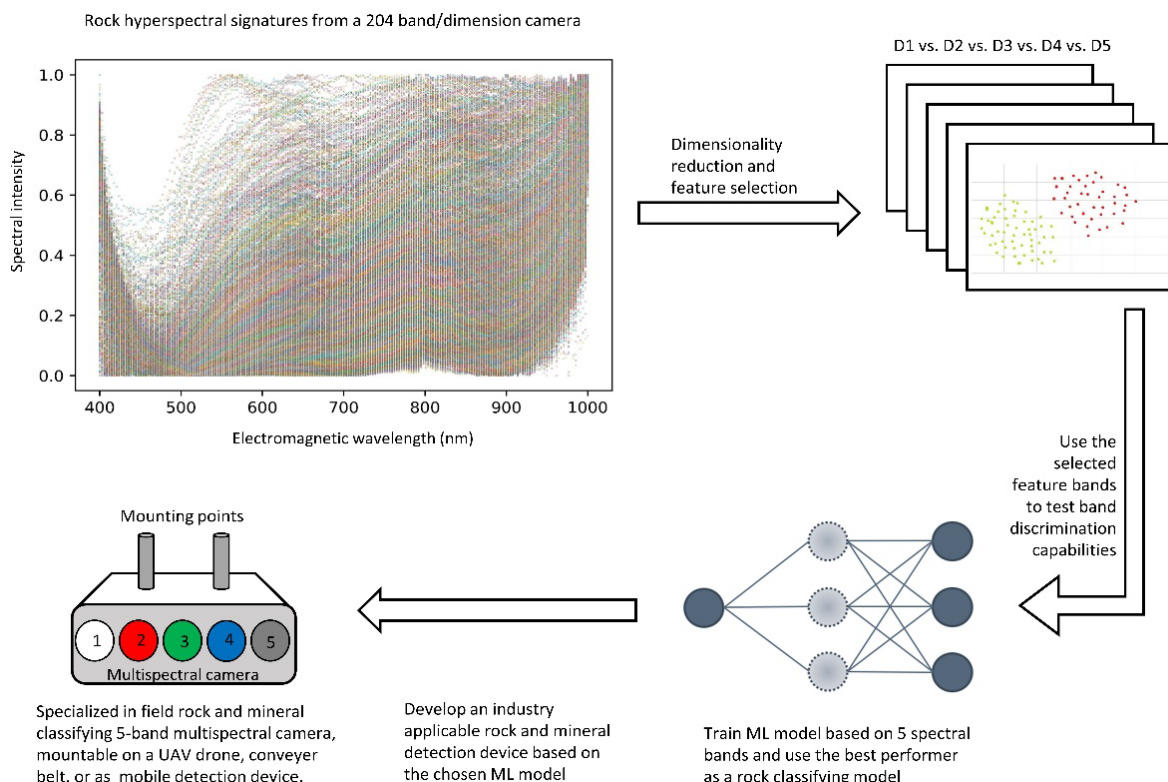


Figure 3.1: The proposed system design, consisting of hyperspectral imaging, dimensionality reduction via Neighbourhood Component Analysis, Machine Learning classification of rocks and minerals to test system viability based on the selected features, and finally employing those

features together with the ML model in developing a unmanned aerial vehicle drone-mountable multispectral camera.

3.2. Methodology for Coupling Dimensionality Reduction with Machine Learning

3.2.1. Hyperspectral Imaging

As previously covered in Chapter 1, Hyperspectral imaging, as defined by researchers (Zhang and Li, 2014; Salles et al., 2017), refers to the collection of hundreds of pixel-scale imagery information pertaining to a subject from within the electromagnetic spectrum. When an image is captured using a hyperspectral camera, such as our 204 bands Specim IQ capturing camera, information pertaining to the subject's interaction with light is recorded (Ganesh et al., 2017). This makes each of the 204 VNIR spectral bands receive a specific signal within each of the approximately 3 nm wide spectral bands. It should be mentioned that camera specifications may differ in terms of the number of spectral bands per spectral range provided by a certain manufacturer. This, in essence, affects the width of each spectral band, it however does not affect the underlying signatures exhibited by specific rocks and minerals.

Having said this, it is evident that analysing hyperspectral data requires sophisticated analysis software. This is because this type of data is computationally costly to analyse, due to the depth of information bands it possesses—often referred to as dimensionalities (Ruiz Hidalgo et al., 2020), hence the term dimensionality-curse (Ruiz Hidalgo et al., 2020; Li et al., 2021, Li et al., 2021). To counter this phenomenon, a method referred to as DR needs to be applied to reduce or eliminate redundant information. Doing so requires a selection of the most representative spectral bands, able to distinguish rocks within our database without affecting or altering their inherent spectral signature differences.

3.2.2. Dimensionality Reduction

DR techniques have in the last couple of decades been a topic of interest for researchers working in computational statistics (Zuniga et al., 2021). It is a key technique in data analysis, aimed at revealing expressive structures and unexpected relationships in multivariate data (Koren and Carmel, 2004; Zheng et al., 2015; Yang et al., 2012; Tuttaß et al., 1995; Ramamurthy et al., 2020). It should, however, be noted that, in general, it is not possible to preserve all pairwise relationships between data points in the DR process (Venna, 2021). DR is used for many purposes; it is beneficial as a visualisation tool to present multivariate data in a humanly accessible form (lower dimensions). Moreover, DR can be applied as a method of feature extraction, and as a preliminary transformation applied to data, such as our rock hyperspectral database prior to the usage of other analysis tools like clustering and classification (Bar-Hillel et al., 2005).

There are many criteria that can be used to sort the various methods of DR. With our objective being a classification task, the aim of our DR is, therefore, to project high-dimensional data points in a low-dimensional subspace whilst keeping most of the ‘intrinsic information’ contained in the original data preserved. This, in principle, keeps the within-class-sample compactness and between class-sample distinguishability (Zhang et al., 2016). The success of which means that a low-dimensional presentation of original data may provide enough information for classification.

3.2.2.1. Supervised vs Unsupervised Dimensionality Reduction Methods

Several DR techniques that reduce the size of the data table, while minimising loss of information have been studied, all of which can describe the essence of the primary data generated. Among these numerous methods, principal component analysis (PCA), linear discriminant analysis (LDA) and maximum margin criterion (MMC) are the most famous ones

because of their simplicity and effectiveness (Hu et al., 2021). Due to the nature of our data, we found that, geometrically, feature extractors based on the maximum margin criterion (MMC) maximise the (average) margin between classes after dimensionality reduction. This would not improve our research as our goal is to use machine learning for this task (Hu et al., 2021). On the other hand, the linear discriminant analysis (LDA) method operates by finding a linear combination of input features (Schölkopf et al., 1998). However, the performance of LDA is degraded when encountering limited available low dimensional spaces and singularity problems, which is one of the disadvantages of LDA (Hu et al., 2021). Lastly, PCA is a linear dimensionality reduction technique that transforms a set of correlated variables into a smaller number of uncorrelated variables called principal components, while retaining as much of the variation in the original dataset as possible (Hu et al., 2021; Kalia et al., 2020; Jiang and Li, 2017).

In addition, sometimes the performance of these methods is limited, as these methods are often unsupervised. Therefore, these methods only use the global structure of the sample, while ignoring the local structure, which are extremely important in helping improving the discrimination of the sample in the projection space. To improve on this, we have employed a supervised NCA method. The assumption is, with this supervised method, the outcome of interest informs the DR solution—this occurs because this method naturally considers the local structures and their labels (Kalia et al., 2020).

3.2.2.2. *Why Employ NCA*

While PCA is one of the most commonly used approaches for DR, the method does not reduce the number of variables (Jiang and Li, 2017; Raghu et al., 2018; Qin et al., 2014). The analyst chooses the number of components to include in analyses based on a prior defined criterion. For example, looking at the screen plot, selecting components with eigenvalues above

one, or selecting the number of components that explain a prespecified proportion of the variance in the data (Hu et al., 2021). Because PCA forces orthogonality between components, it imposes a rigid structure (Hu et al., 2021; Kalia et al., 2020).

NCA, on the other hand, performs better both in terms of classification performance in the projected representation and in terms of visualisation of class separation as compared to the standard unsupervised methods. Moreover, regarding NCA, one can substantially reduce the costs, storage, search, running and time spent on waiting at the test phase by forcing the learned distance metric to be low rank. This, therefore, favours its potential application in real-time field analyses (Liu and Chen, 2006).

NCA is a distance-based feature weighting, non-parametric supervised method, it works by automatically selecting the most significant features (Goldberger et al., 2004; Jiang and Li, 2017). To calculate the correlation between features and target, a Mahalanobis distance-based fitness function is used. The weighting of features is carried out as follows; initial weights are assigned randomly, thereafter, weights are updated using the stochastic gradient descent or ADAM optimisation method and Mahalanobis distance-based function, hence positive weights are generated for each feature (Goldberger et al., 2004; Jiang and Li, 2017; Liu and Chen, 2006).

Though Goldberger et al. (2004), applied their NCA algorithm for face recognition, they too mention that the NCA algorithm learns a training set distance metric, and can improve k-NN classifications, hence achieving very good performance. Koren & Carmel (2004) further support the employment of an NCA model by saying it provides a linear transformation model that optimises the performance of k-NN in the learnt low-dimensional space. These said advantages influenced our desire to employ NCA in distinguishing rocks from within our rock hyperspectral database.

However, researchers (Koren and Carmel 2014; Goldberger et al., 2004; Liu and Chen, 2006; Kartun-Giles and Bianconi, 2019) note that unlike the common PCA method, which is both convex and has an analytical solution, another key difference distinguishing the two is that NCA is a non-convex optimisation problem. This means every time one runs NCA, they may get a different solution, and like K-Means and other non-convex algorithms, it is advisable to run it more than once and take the best solution. Hence, our paper presents the best NCA bands from having run NCA multitudes of times and selected features that express themselves most frequently. Researchers (Koren and Carmel 2014; Liu and Chen, 2006) explain this by noting that this occurs as NCA components are not ordered nor dependent on the chosen target dimensions.

This, however, is not a drawback as run times are extremely short. Moreover, once the number and specific band positions have been specified, subsequent classification tasks require significantly less storage, fewer test times, and the redundant bands are eliminated along with their datasets. These chosen components (spectral bands) are, therefore, assumed to be the most sufficient in determining the rocks within, or related to, a said database. These said sample signatures may include mine, laboratory or environmental rock spectral signatures, such as in our case.

3.2.3. Why Machine Learning?

Though NCA provides the opportunity to ignore redundant data-heavy bands, it does not provide any information related to the retained classification accuracy, hence the need to employ an ML algorithm(s). We use ML for multitudes of data-related tasks or problems. It has grown as a subdomain of Artificial Intelligence (AI) that comprises models capable of deriving useful information from data and utilising that information in self-learning that aids in making good classifications or predictions (Sinaice et al., 2020, Sharma et al., 2021). ML

has gradually gained popularity, due to its accuracy and reliability (Gunduz, 2021). Improved hardware and software components of machine vision systems have aided in building ML algorithms that process data faster and give reliable decisions in very little time (Saha and Annamalai, 2021). Since we are dealing with a classification problem with labelled data, we employed and compared several supervised ML algorithms. Supervised learning requires learning a model from labelled training data that helps in making classification or predictions about the future data (Saha and Annamalai, 2021; Jain et al., 2018). Supervised, in essence, indicates sample sets in which the desired output is known. In other words, the labelling of data is done to guide the machine to look for the exact desired pattern.

3.3. Practical Experiments

3.3.1. Capturing Rock Hyperspectral Signatures

As previously covered in Chapter 2.3.1., this Chapter employs the same data from the 32 different igneous rocks belonging to eight rock lithologies (four samples per lithology), namely, granite, diorite, gabbro, granodiorite, rhyolite, andesite, basalt and dacite. By combining the hyperspectral signatures from all the 8 rock lithologies, Figure 3.2 is formed.

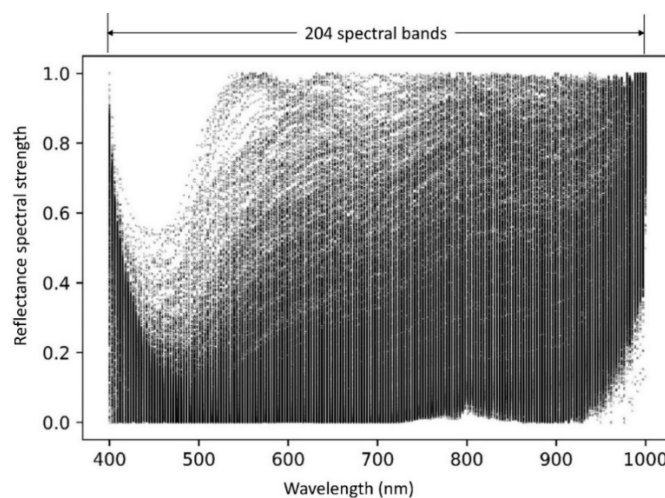


Figure 3.2: A hyperspectral signature database with 204 dimensionalities from within the VNIR.

Figure 3.2 is an illustration of all the high dimensional spectral signatures used to create a single database. Since each spectral band represents a single dimensionality, the data in this database is said to possess 204 dimensionalities from within the VNIR.

3.3.2. Selecting the Appropriate Feature Bands

As previously mentioned in Section 2.2, the common problem that may arise during a DR process is defining how many features to select for analysis. This is often dictated by the purpose of employing such a DR method. In this paper, based on the currently available industry produced spectral imaging devices, such as the ‘DJI P4 multispectral drone’ used in agricultural applications and environmental monitoring, our objective was to identify the appropriate rock classifying multispectral bands. From these bands, it would then be easier to develop a UAV drone-mountable multispectral sensing camera specialised in classifying rocks and minerals.

To achieve this, we convert heavy hyperspectral imagery classification data to less heavy multispectral classification data to meet weight restrictions, industry standards and production costs of developing such a device. This conversion is performed in consideration of the rocks and/or minerals from which subsequent multispectral data collection, such as from a UAV drone-mounted multispectral camera, is to be recorded and classified for a plethora of rock engineering purposes.

Transitioning from high dimensional hyperspectral to low dimensional multispectral data is not without challenges. The selection of a suitable method according to the type of data is a big issue that often needs to be addressed. It is essential to find a suitable mechanism to attain the highest level of accuracy when comparing the outputs of different DR techniques. Since it is well documented that supervised methods generally outperform unsupervised methods, we employed the NCA DR technique as it is a supervised and highly acclaimed

method. As a way of determining the significance of employing the 204 spectral bands with all ‘redundant features’, we used our NCA algorithm to eliminate and record the attainable output accuracies in classifying the rocks. This was based on the full 204 feature bands, down to 100, 50, 25, 10, and finally, the current UAV drone-mountable multispectral 5-band feature classification bands. NCA DR eliminates redundant information by assigning each dimensionality from within the hyperspectral signatures a feature weight (Figure 3.3).

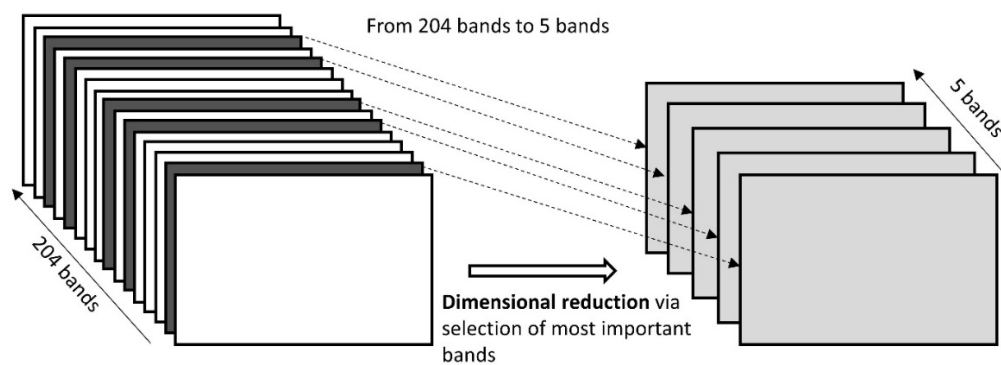


Figure 3.3: A hyperspectral signature database with 204 dimensionalities from within the VNIR.

As (Goldberger et al., 2004; Jiang and Li, 2017) researchers have mentioned before, finding the relevant and important features is a problematic task. It entails domain knowledge, and human expertise to extract the most relevant features for future processing and selection of ML models for classification (Sharma et al., 2021; Gunduz, 2021; Jain et al., 2018). Employing NCA, however, makes this process easier as the algorithm assigns feature weights to each of the dimensions, thereby highlighting the most relevant features/bands for such a database. Having employed NCA to select the most relevant features that contribute most to the prediction (dependent) variable, the final step entails exporting the selected features into an ML model. The model is then trained, thereafter, we can determine the classification capabilities based solely on these feature bands.

3.3.3. Post-NCA Classification via ML

To commence with the post-NCA classification task, we begin by preprocessing our data based on the number of spectral bands intended to be used in the rock and mineral classification task. For the initial training and classification, 100% of all the 204 spectral band signature data is employed for classification—this acts as a control task. Thereafter, depending on NCA feature weights, only the high-feature-weight possessing spectral bands are employed in succeeding classifications, which in essence means discarding the rest of the data that is deemed redundant. By doing this, we decrease data storage costs, as well as take a step towards developing a field applicable multispectral band camera. The classification was performed for 204-bands, 100, 50, 25, 10 and 5-bands using various ML models, thereby allowing for classification accuracy checks for the various band reductions.

3.4. Experimental and Analytical Results

3.4.1. Findings Based on NCA

NCA is a method that seeks to identify and down-scale global unwanted variability within the data. The method changes the feature space used for data representation by a global linear transformation referred to as a Mahalanobis metric, which assigns large weights to relevant dimensions which are the most discriminatory spectral bands (Goldberger et al., 2004). Consequently, low weights are assigned to irrelevant dimensions, which we can, thus, refer to as less discriminatory spectral bands (Liu and Chen, 2006). These relevant dimensions are estimated using a subset of points that are known to belong to the same although unknown class, also referred to as chunklets (Bar-Hillel et al., 2003). These chunklets are obtained from equivalence relations by applying a transitive closure within the algorithm. This transformation is, therefore, intended to reduce clutter, so that in the new feature space, the inherent structure of the data can be more easily unravelled (Ayesha et al., 2020).

The mathematical transformation from Figure 3.2 to 3.4 originates from the Goldberger et al. (2004) cost function from stochastic neighbour assignments in the transformed space whose function is to learn the neighbourhood components (Equation 3-6). More precisely, for each point x_i , it selects another point x_j as its neighbour with the probability p_{ij} . Hence, x_i would be classified as the label of point x_j with the same likelihood. The definition of p_{ij} with Euclidean distance is represented by Equation 3 in the softmax structure.

$$p_{ij} = \frac{\exp(-\|Ax_i - Ax_j\|^2)}{\sum_{k \neq i} \exp(-\|Ax_i - Ax_k\|^2)}, \quad p_{ii} = 0 \quad (3)$$

where A is the matrix that needs to be learnt for transforming the input data linearly. Based on such a stochastic neighbour assignment structure, the probability that point x_i would be classified correctly is computed as follows (Equation 4):

$$p_i = \sum_{j \in C_i} p_{ij} \quad (4)$$

where C_i represents the set of points that have the same class label as point x_i , and c_i denotes the class label of point x_i ; then, we define this set as $C_i = \{j | c_i = c_j\}$. The objective function of NCA is thus shown in Equation 5, which is also the expected number of points that are correctly classified.

$$f(A) = \sum_i \sum_{j \in C_i} p_{ij} = \sum_i p_i \quad (5)$$

To maximize the objective function, the common method is to use a gradient-based optimizer according to the derivative of $f(A)$. When we denote that $x_{ij} = x_i - x_j$, then the derivative of $f(A)$ with respect to A is derived in Equation 6.

$$\frac{\partial f}{\partial A} = -2A \sum_i \left(p_i \sum_k p_{ik} x_{ik} x_{ik}^T - \sum_{j \in C_i} p_{ik} x_{ik} x_{ik}^T \right) \quad (6)$$

Based on Figure 3.4, our NCA algorithm flawlessly reduced the dimensionality space of the hyperspectral signatures. We are, therefore, able to compare the different projection graphs of each of the 5-bands against one another in 2D spaces, hence mapping or visualising the manner in which the rocks plot at these chosen high classification dimensionalities. Results from the NCA algorithm in Figure 3.4 show that there are multitudes of spectral bands that one would refer to as relevant as they possess a substantial feature weight relative to the rest. Depending on the computational resources an entity or individual possesses, the number of spectral bands one desires to employ for future classifications having done away with redundant bands is upon the user. Having said this, we used Figure 3.4 to select the most rated bands as we can indeed see the redundancy in some of the feature bands.

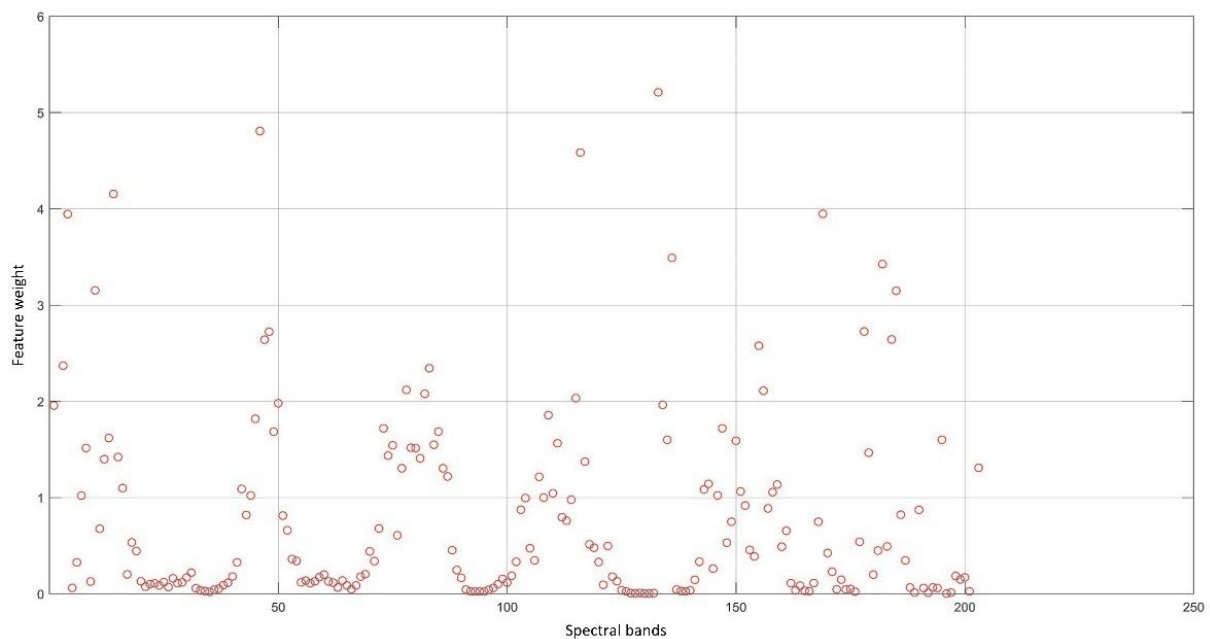


Figure 3.4: Neighbourhood Component Analysis feature selection which assigns higher weights to the most discriminatory hyperspectral bands by eliminating redundancy in data, with the top five feature-bands being 14, 46, 116, 133 and 169.

As stated in Section 3.3.2, our intended use of the most representative feature bands requires 5-bands which, according to Figure 3.4, are located at positions 14, 46, 116, 133 and 169 from the 204 feature bands of the VNIR. From these selected feature band positions, we

can then convert these positions into electromagnetic wavelength bands. Doing so, we get 441 nm, 535 nm, 741 nm, 791 nm and 897 nm as the most discriminatory spectral bands for our rock database. It should be noted that, considering each of these spectral bands is approximately 3 nm wide, a system designed to classify rocks based on these five spectral bands would have an error of ± 3 nm, as stated in Section 2.1. Having said this, we can safely say our NCA algorithm flawlessly assigns feature weights to high dimensionality hyperspectral data. This allows the user to select the number of spectral bands they wish to employ based on NCA assigned feature weights.

DR is the transformation of data from a high-dimensional space into a low-dimensional space so that the low-dimensional representation retains some meaningful properties of the original data, ideally close to its intrinsic dimension. From this statement and having selected the now five multispectral bands to employ in future classification problems related to our data, our NCA breaks down the hyperspectral signatures. This allows for visualisation in 2D spaces whose X and Y planes are the NCA-defined spectral bands with the highest feature weights, as shown in Figures 3.5 and 3.6.

It should be noted that there are numerous ways in which these (Figure 3.5 and 3.6) dimensionally reduced band-by-band projections can be interpreted. Starting with the relative reflectance spectral strength scatter plots (normalised to 1), where each point represents the relative reflectance spectral strength of each rock sample's previously extracted 20×20 pixels averages. The area within which every point plot within the scatter plots is governed by the relative spectral strength between its (previously extracted 20×20 block averages) spectral reflectance strength within its respective spectral band (for example, band 14), in relation to the other band (hence 2D), as well as in relation to the other seven rocks (eight in total). Having said this, the point with the highest relative spectral reflectance strength in these three categories (respective band, other band and other rocks) would plot at the rightmost region of

the scatter plot. Having plotted these points, the relative frequency histogram sums and summarises the frequency densities of the points from 4 scatter plots into 1 (Figures 3.5 and 3.6). Since these histograms are also relative, the most densely populated rock points are normalised to 1. From interpreting the relative scatter and histogram plots, we can assess the spectral reflectance strengths of rocks in lower, dimensionality reduced, 2D planes.

Here, is an example of interpretations deducible from Figure 3.5 where band 14 occupies the x-axis, and bands 46, 116, 133 and 169 occupy the y-axis. From band 14's histogram (leftmost), we can make the following assumptions based on the number of rock spectral reflectance strength points summarising the scatter plots directly below it. Gabbro has the highest relative density of points (hence, the highest peak), meaning this rock has the highest concentration of points located within the further right small patch area of band 14. This is supported by the four scatter plot projections at bands 46, 116, 133 and 169, where we can see a similar dense cluster of gabbro data points (pink colour) located at this said location of the relative scatter plot projections (Figures 3.5 and 3.6). Within the same patch of area, we see that the next densely populated points belong to basalt and andesite, where basalt shows a slight edge over andesite. Below these point frequency densities, we find diorite, followed by rhyolite, granodiorite, granite and dacite as the least dense.

However, we see a difference in the density of points for the histogram bar on the immediate left to the previously described. The frequency of points starts from diorite as the most densely populated within this small area. This is followed by basalt, dacite, gabbro, granodiorite, a tie between andesite and rhyolite, and granite as the least dense. Within the same band 14 projection against other bands, we can see a relatively equal frequency density of data points within the first half (left to the middle) of the projection for seven rocks. This is with the exception of granite, which has a higher density of points within this wide area. Therefore, we can make similar assessments of data points for the 46, 116, 133 and 169 bands,

as the x-axis and draw different patterns based on the frequency and location of rock relative reflectance strength points. Having said this, we can safely say, based on Figures 3.5 and 3.6 relative scatter and frequency histograms—thus, we can make predictions on future rock identification problems related to those of our study.

Hence, should new data, related to our rock database with similar multispectral bands (441 nm, 535 nm, 741 nm, 791 nm and 897 nm), be introduced, we expect such data to exhibit similar patterns as the rocks we have assessed. This may be in terms of relative frequency density relationships, or areas within which such rock relative reflectance spectral strength points are expected to exist. From these density histograms and scatter plots, we can make one more assumption. The more the frequency of data points exist within a small area, the easier it is to identify with a naked eye such rock relative points based on the scatter plots. The opposite is true for scattered data points. As much as NCA can reduce dimensionality, visual rock identification based on Figures 3.5 and 3.6 patterns alone is time-consuming and prone to some human error. Hence, there is a need to employ objective ML models which can draw patterns faster and more accurately. Moreover, ML models give feedback with regard to the best rock delineation strategies.

The normalized eigenvectors (relative frequency scatter and histogram plots) in Figures 3.5 and 3.6 are nothing but eigenvectors having a unit length. Thus, each normalized eigenvector can be found by simply dividing each component of the vector by the length of the vector. By doing so, the vector is converted into the vector of length one. Ayesha et al. (2020) refer to this representation as eigendecomposition, where decomposing a matrix means that one intends to find a product of matrices that is equal to the initial matrix. As a result, via NCA, the initial matrix is decomposed into the product of its eigenvectors and eigenvalues.

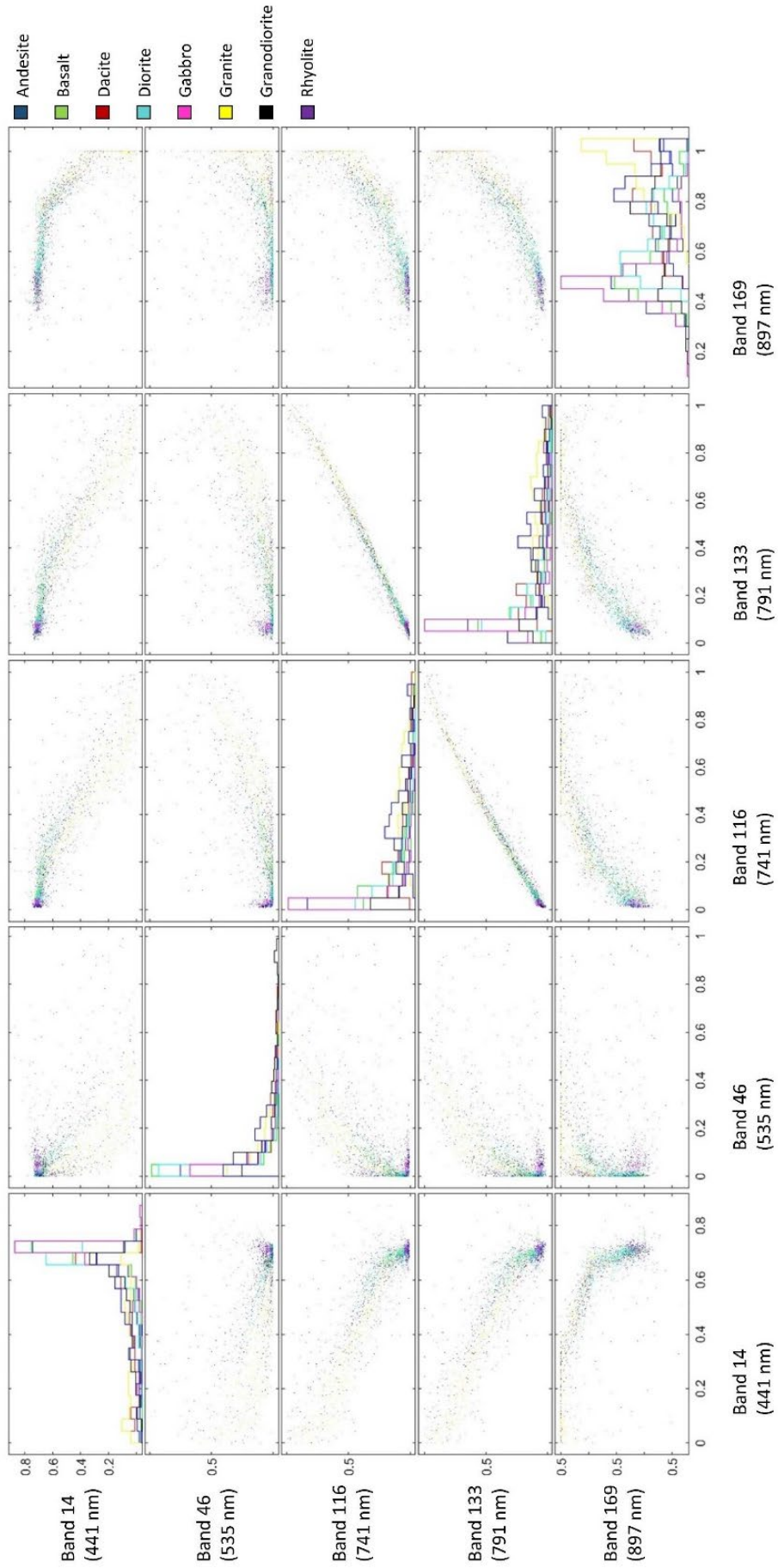


Figure 3.5: Projection of complex rock hyperspectral signature data points in dimensionality reduced (via Neighbourhood Component Analysis feature selection) 2D planes showing the relative reflectance spectral strength relationships between five different spectral bands for eight rock lithologies.

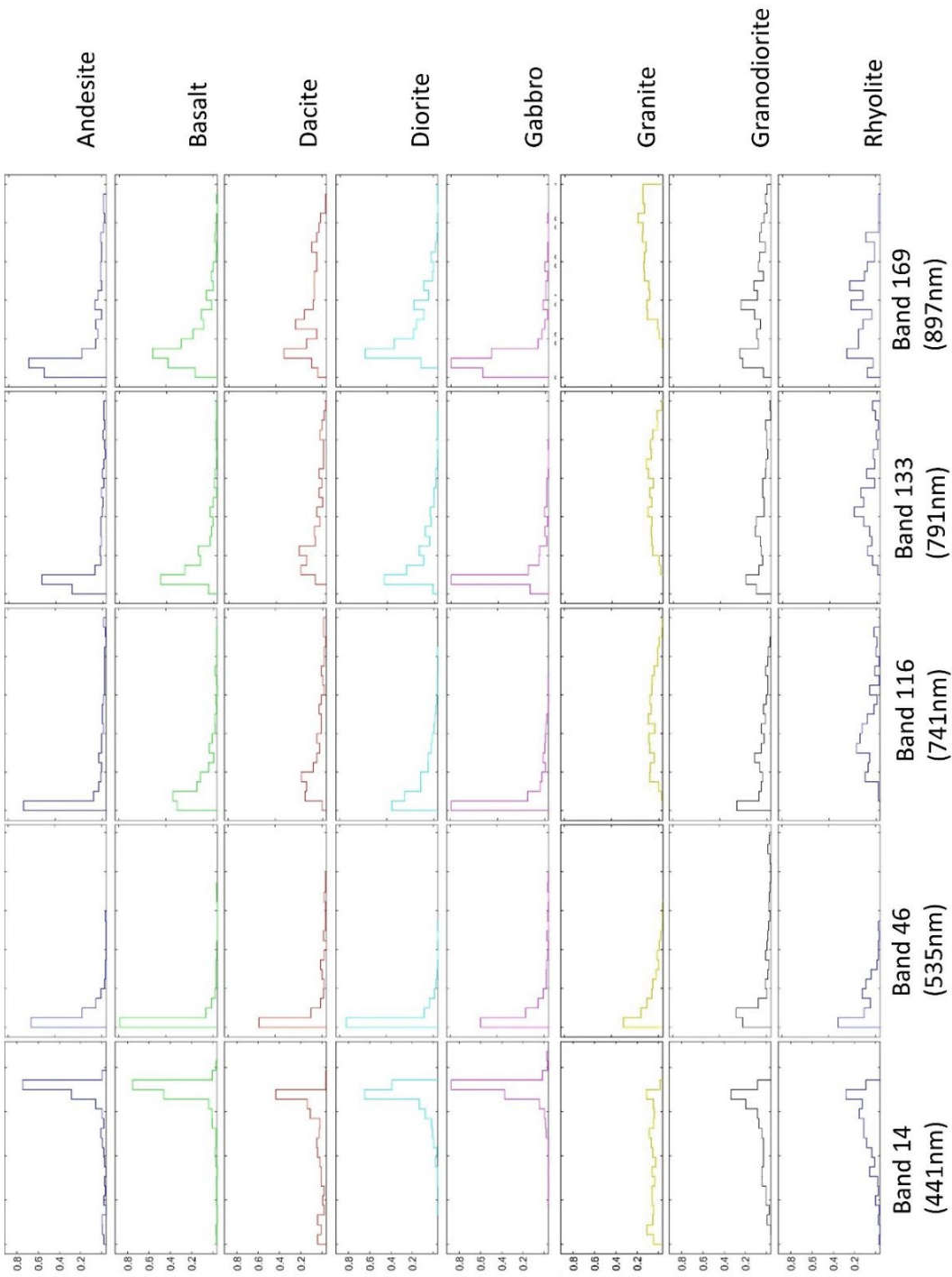


Figure 3.6: Post Neighbourhood Component Analysis hyperspectral signature projections as relative frequency histograms; a simplification of Figure 3.5.

3.4.2. Classification with ML, Post-NCA

Supervised learning uses an algorithm that requires external help. The provided input database is automatically separated into training and testing datasets. The output variable is predicted or classified from the training database. Algorithms try to learn some shapes during training of the database and implement these learnt patterns to the testing database, which provides results in relation to the learnt patterns (Saha and Annamalai, 2021; Gundu, 2021; Jain et al., 2018). From these output results, we can evaluate the performance of each algorithm.

As shown in Figure 3.7, a 5-folds-cross-validation (6825 divided 5) was used to process the data at all times, resulting in 1365 samples (including all eight rock lithologies) being used in each set. This ensures that every observation set (with each of the eight rocks contributing) from the original dataset has the chance of appearing in training and test sets as the ultimate goal is to classify entire rocks (Figure 3.7). This method generally results in a less biased model compared to other methods, it is said to be one of the best approaches whenever there is a limited amount of input data (Jain et al., 2018). Since the number of samples is 6825 (rows), it does not reduce, only the number of bands/features reduces (columns, from 204 down to 5). Each row represents the spectral reflectance strength of each rock signature, whilst each column represents the position of the wavelength band from which the spectral strengths have been extracted, hence forming a 2D matrix. As a result, a breakdown of the input dataset matrices is as follows; for 204 bands (full database), input dataset is 204 (columns) \times 6825 (rows) matrix = 1,392,300; for 100 bands, input dataset is 100 \times 6825 matrix = 682,500; for 50 bands, input dataset is 50 \times 6825 matrix = 341,250; for 25 bands, input dataset is 25 \times 6825 matrix = 170,625; for 10 bands, input dataset is 10 \times 6825 matrix = 68,250; for five bands, input dataset is 5 \times 6825 matrix = 34,125.

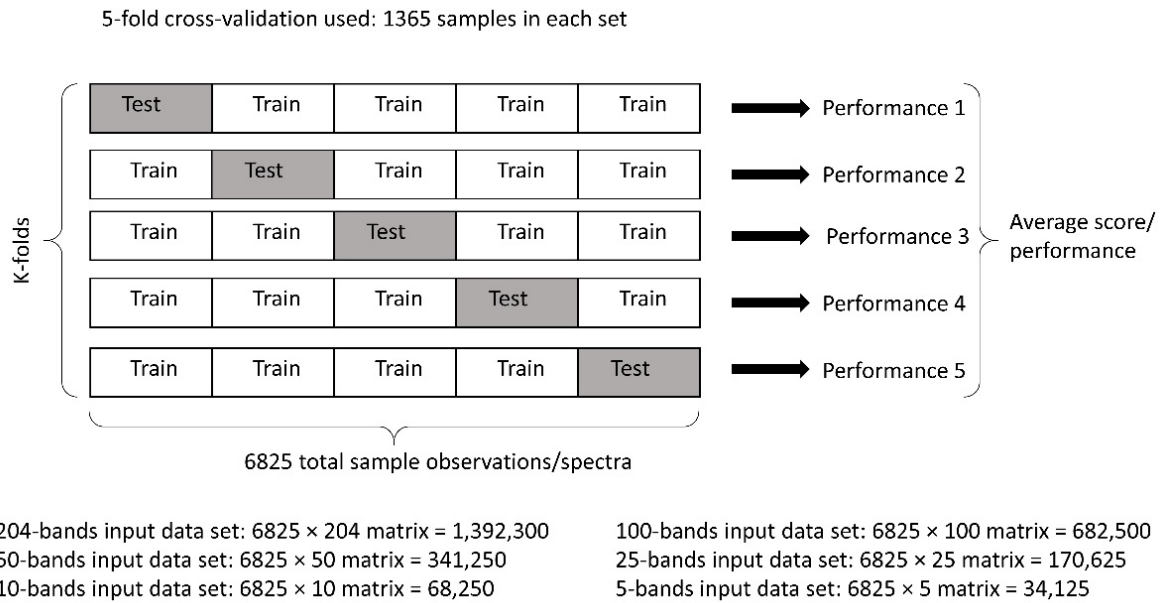


Figure 3.7: Database handling of training and testing sets. A 5-fold-cross-validation was used in all instances.

Using MATLAB R2020b classification learner Machine Learning toolbox, we assessed multiple ML algorithms and combined the best five classification performers in terms of training, average per class precision, and time taken to train the algorithm. These attributes are said to be the most important classification evaluation criteria. Moreover, these attributes govern industrial applicability and the overall viability of the algorithm. Table 3.1 is a compilation of the top-performing ML algorithms per given number of selected spectral bands from the pre-DR 204 spectral bands, down to 100, 50, 25, 10 and our intended goal of five spectral bands. It demonstrates the differences in classification based on bands with the most feature weights. Results from the ML models in Table 3.1 show that the highest performing model in all pre-and-post classifications was the Cubic Support Vector Machine (SVM).

A similar approach was applied by Galdames et al. (2019), where they performed a feature selection from 2424 spectral channels to 73 spectral channels. Their study employed colour images, a VNIR sensor, as well as a SWIR (900–2500 nm) sensor. They achieved a

classification performance of 99.73% using Conditional Mutual Information Maximisation to select their most important features. Considering the tools and number of bands selected at the most intrinsic bands, we would argue our methods achieves more for less. On the other hand, Mei et al. (2019), employed Unsupervised Spatial-Spectral Feature Learning by 3D Convolutional Autoencoder for Hyperspectral Classification. Though with high classification capabilities, we believe this method is computationally taxing as convolutional neural networks are known to require a lot of training data and times, making CNNs invalid in our five feature bands quest.

From the results compiled in Table 3.1, we can appreciate the differences in accuracies acquired and elapsed times when training our ML models before and after DR. This confirms our hypothesis, which stated that with NCA, ML will maintain rapid run times and good accuracies, while maintaining without compromise, the fundamental differences in the hyperspectral signatures of rocks within our database. Global accuracy refers to the validation accuracy acquired during training. Average per-class precision refers to the individual rock classification sum averages in testing the models. Lastly, training time refers to elapsed time in training the models to classify the rocks based on the number of spectral band datasets.

As our goal was to reduce the number of hyperspectral bands to five multispectral bands capable of distinguishing rocks at a substantial, industry applicable accuracy, we assessed the highest performing Cubic SVM ML model for the 5-band classification. The results are presented in Figure 3.8. To assess the viability of this Cubic SVM model, Figure 3.8 presents two performance metrics. The first is True Positive Rates (TPR), defined as the probability that an actual positive will test positive (Equation 1). The second is False Negative Rates (FNR), defined as the probability that a true positive will be missed by the test (Equation 2). Both variables are highly viable in assessing the capability of the ML model in classifying each rock.

Table 3.1: Top five machine learning classification comparisons based on pre-dimensionality reduction from 204-bands, to post-dimensionality reduction (using Neighbourhood Component Analysis) for 100, 50, 25, 10 and 5 rock spectral bands.

Number of Classification Bands post-NCA	Machine Learning Algorithm	Global Accuracy (%)	Average per-Class Precision (%)	Training Time (seconds)
204-bands *	SVM (Cubic SVM)	90.7	90.0	28.7
	SVM (Quadratic SVM)	87.0	86.0	27.3
	SVM (Linear SVM)	79.1	76.5	13.8
	Linear discriminant	80.4	78.4	4.6
	Ensemble (Subspace discriminant)	81.2	79.3	41.5
100-bands	SVM (Cubic SVM)	89.4	88.7	37.7
	SVM (Quadratic SVM)	84.7	83.8	21.8
	Quadratic Discriminant	77.9	77.5	1.0
	SVM (Linear SVM)	76.9	76.0	5.9
	Linear Discriminant	76.7	75.6	1.1
50-bands	SVM (Cubic SVM)	86.9	85.7	39.1
	SVM (Quadratic SVM)	84.3	82.1	23.2
	Quadratic Discriminant	79.1	78.9	1.1
	SVM (Linear SVM)	76.1	75.4	5.3
	Ensemble (Subspace KNN)	75.2	75.0	34.9
25-bands	SVM (Cubic SVM)	86.3	86.2	45.1
	SVM (Quadratic SVM)	83.9	82.6	28.2
	SVM (Fine Gaussian SVM)	75.9	70.6	6.7
	Quadratic Discriminant	75.7	75.3	1.2
	Ensemble (Subspace KNN)	75.4	70.0	29.2
10-bands	SVM (Cubic SVM)	81.0	80.3	78.2
	SVM (Quadratic SVM)	78.2	76.0	40.7
	SVM (Fine Gaussian SVM)	72.7	70.1	8.2
	Ensemble (Bagged trees)	71.0	69.8	19.1
	Ensemble (Subspace KNN)	70.6	70.3	17.9
5-bands	SVM (Cubic SVM)	70.9	72.0	182.1
	Ensemble (Bagged trees)	68.6	67.0	12.3
	SVM (Quadratic SVM)	68.4	65.8	76.7
	SVM (Fine Gaussian SVM)	68.4	66.6	7.5
	KNN (Fine KNN)	67.3	66.0	5.7

• * Pre-dimensionality reduction.

Another assessment that can be drawn from the Figure 3.8 confusion matrix is the average per-class precision of 72%. This is substantial considering the magnitude of the DR from 100% of that hyperspectral data (204-bands) to approximately 2.5% (5-bands), which we now refer to as multispectral data. We have, therefore, determined an applicable classification model for this particular problem. In addition to this, we gained a reduction in computational costs and storage requirements, ease of data management, ease of data application and visualisation, and most importantly, viability in rapid field applications.

In addition to the above-given assessment, Figure 3.8 illustrates the in-depth classification capabilities of the ML algorithm post-DR for each class of rocks employed in this study. From the Figure 3.8 confusion matrix, 63.3% of the initial input andesite datasets (for 5-bands) were correctly (TPR) classified as andesite. On the other hand, the remaining 36.7% (FNR) was incorrectly classified as basalt (15.6%), dacite (4.8%), diorite (4.4%), gabbro (5.9%), granite (1.1%), granodiorite (1.9%), and rhyolite (3.0). Similar assessments can be made for all rocks, resulting in different ratios of both TPR and FNR. Comparing Figure 3.5 and 3.6 results, we can make the following assumptions; the flatter the relative frequency histograms (Figures 3.5 and 3.6), the higher the prediction precision (Figure 3.8), hence granite has the highest ML prediction precision. On the other hand, the steeper the relative frequency histograms (Figures 3.5 and 3.6), the lower the ML prediction precision (Figure 3.8), hence basalt and gabbro have lower ML prediction precision outcomes. By developing algorithms on a particular type of rock, it is possible to improve any of the Figure 3.8 results to favour that specific rock, mineral or environmental phenomenon of interest. This thereby makes this system highly applicable in a magnitude of highly specialised classification problems. Doing so simply requires importing the most discriminative hyperspectral bands of any particular rock, mineral, or phenomenon, and giving them priority over other spectral bands, hence improving their succeeding ML classification outputs. However, since the goal of this paper

was to classify eight igneous rock lithologies as a collective based on five multispectral bands, our system was not pre-programmed to be biased towards any of the eight igneous rock lithologies, but rather used the data as is, hence the true/unmodified results.

Model 1.10 (Cubic SVM)

True Class	Model 1.10 (Cubic SVM)									
	Andesite	Basalt	Dacite	Diorite	Gabbro	Granite	Granodiorite	Rhyolite	TPR	FNR
Andesite	63.3%	15.6%	4.8%	4.4%	5.9%	1.1%	1.9%	3.0%	63.3%	36.7%
Basalt	10.8%	61.0%	4.6%	13.3%	4.9%	1.0%	1.5%	2.8%	61.0%	39.0%
Dacite	3.3%	4.3%	80.5%	3.8%	1.4%	4.3%	0.5%	1.9%	80.5%	19.5%
Diorite	0.4%	7.0%	0.9%	66.3%	3.9%	3.7%	16.9%	0.9%	66.3%	33.7%
Gabbro	9.6%	9.3%	0.7%	9.3%	61.9%	0.7%	6.7%	1.9%	61.9%	38.1%
Granite	0.6%	0.3%	2.2%	5.0%		88.9%	1.7%	1.4%	88.9%	11.1%
Granodiorite	1.5%	1.1%	1.5%	17.4%	2.6%	1.9%	73.3%	0.7%	73.3%	26.7%
Rhyolite	2.8%	6.7%	0.6%	0.6%	0.6%	5.0%	3.3%	80.6%	80.6%	19.4%
	Predicted Class									

Figure 3.8: Confusion matrix from a Cubic SVM machine learning model used in evaluating the classification viability of post dimensionality reduction spectral bands

Without having to perform NCA again for individual rocks, the same 5 database-defined bands can be used to optimize the ML classification capabilities for each rock in the 8 rock database. For Table 3.1 and Figure 3.8, the input dataset has 8 categories coinciding with 8 rocks, this informs the ML model to output 8 classification capabilities for each of the 8 rocks. However, in order to maximize the classification precision capabilities of each rock against the rest of the database, a pre-processing step has to be performed prior to training various ML

models (Ruiz Hidalgo et al., 2020; Tong et al., 2017). This entails assigning a new common label (Other rocks) to 7 rocks and keeping the same initial label (Actual rock) for the rock whose output is to be optimized against the 7 (Table 3.2).

This means, for example, leaving all andesite spectra with their labels and changing the rest of the 7 rock names to 'other rocks'; basalt, dacite, diorite, granite, gabbro, granodiorite, and rhyolite labels changed to 'other rocks'. When training the supervised ML models that take into account the data labels post this name change, the models attempt to output 2 categorical outputs, thereby, meaning, andesite or non-andesite (other rocks). Results from training the ML models with such emphasis on a particular rock show that ML models output higher individual rock classification precisions. This is demonstrated in Table 3.2 where andesite classification precision improved from the previous (TPR) 63.3% (Table 3.1) before optimization pre-processing to an improved (TPR) 87.8% (Table 3.2). Table 3.2 moreover shows that by applying this individual rock pre-processing step, the global classification accuracy for all 8 rock classifications improves from the previous whole database training method from 70.9% (Table 3.1) to an average of 95.4% for all 8 rocks individually optimized (Table 3.2).

It should however be noted that the Table 3.1 5-bands outputs, as well as Figure 3.8, originate from a single trained model, whereas Table 3.2 is a compilation of 8 different ML models optimized for given rocks. Therefore, in terms of the number of steps necessary to obtain output results, whole database training possesses the upper hand. On the other hand, in terms of individual rock classification precision, pre-processing outputs the best results. Instead of having an 8 outputs precision confusion matrix such as before pre-processing, Table 3.2 is a summary of each of the 8 ML model confusion matrices. This means, that for a model optimized to classify andesite and the rest of the rocks as a whole, the TPR for andesite is 89.8%, with a FPR of 10.2%. The same model classifies the rest of the rocks (7 rocks as a whole) with a TPR of 97.3%, and a FPR of 2.7%.

Table 3.2: Optimized ML classification capabilities for subject rock vs. other rocks post NCA.

Rock	Model	Global acc. (%)	Actual rock TPR prec. (%)	Other rocks in database prec. (%)
Andesite	Ensemble (subspace KNN)	95.4	87.8	97.3
Basalt	Ensemble (subspace KNN)	94.1	89.2	95.9
Dacite	Ensemble (Bagged trees)	96.3	88.3	97.8
Diorite	Ensemble (Bagged trees)	92.2	94.8	90.8
Gabbro	Ensemble (subspace KNN)	95.7	90	97.1
Granite	Ensemble (Bagged trees)	96.2	97.4	95.8
Granodiorite	Ensemble (subspace KNN)	95.8	90.4	97.1
Rhyolite	Ensemble (Bagged trees)	97.6	91.9	98.5

Based on Table 3.2, the best performing models are Ensemble as compared to the previous SVM model (Table 3.1). This could be attributed to the number of expected outputs, 8 outputs in Table 1 (optimized for the whole 8 rocks database), and 2 outputs for Table 3.2 (optimized for each rock). The Ensemble method is defined as a ML technique that combines several base models in order to produce a single optimum classification model (Asscher et al., 2021). Though the most common Ensemble methods utilize decision trees (Deegalla et al., 2022), other types such as Bagged and k-nearest neighbours (KNN) can be applied (Table 3.2).

Table 3.3 is a summary of Tables 3.1 and 3.2, showing the changes in classification precisions attainable from training the ML models with 8 classes, as compared to training with 2 input and output classes. The average individual rock TPR (labelled 2 outputs) on Table 3.3) precision is 91.2%, a 20.3% improvement from the previous average TPR (labelled 8 outputs) of 72%.

Table 3.3: Summary of ML classification precisions based on Figure. 3.8, Table 3.1 and Table 3.2 post NCA outputs.

Rock	8 outputs TPR prec. (%)	2 outputs TPR prec. (%)	Percentage change (%)
Basalt	61.0	89.2	+28.2
Dacite	80.5	88.3	+7.8
Diorite	66.3	94.8	+28.5
Gabbro	61.9	90.0	+28.1
Granite	88.9	97.4	+8.5
Granodiorite	73.3	90.4	+17.1
Rhyolite	80.6	91.9	+11.3
Whole database (averages)	72	91.2	+20.3

From Table 3.3, andesite, basalt and diorite show a greater increase of 20%+ in their classification precision. This could be attributed to the shape of their frequency histogram shapes (Figures 3.5 and 3.6) being distinctly different with steep peaks at different positions across all 5 bands as compared to those from other rocks. On the other hand, granite, dacite, and rhyolite, show a slight increase in their classification precision capabilities. This is potentially attributed to their relatively similar frequency histograms across the 5 spectral bands or dimensionalities (Figures 3.5 and 3.6). These results show a strong correlation between the NCA 2D plots with the employed ML models, hence proving the significance of objective ML models.

3.5. Significance of Proposed System

Therefore, given our findings, we can confirm that our proposed system, which consists of DR of rock hyperspectral data and subsequently employing specific discriminant features for our igneous rock database, performs extremely well. This, in essence, means for rock engineering, problems requiring discrimination of rocks, minerals, soils and other environmental phenomena based on their spectral signatures can indeed employ this system.

By setting desired attributes founded on preknowledge of a site, such as types of rocks present within a mine site, rocks transported via a conveyer belt, or the general mapping of the environment, it is possible to maximise data collection. Based on specific multispectral bands, we can eliminate unnecessary storage, processing or classification costs associated with massive data. With our integrated system, here are several optimisations we were able to achieve:

- Through DR, we can reduce the storage capacity required to store and handle a database, thereby reducing storage costs as we have proven there is no need to collect, store and process redundant data;
- With DR, we were able to break down hyperspectral signature data into different dimensionalities, hence the ability to plot such data in 2D planes, which as a result allows for easy visual assessment;
- As proven with post-NCA specialised multispectral imaging, we can attain respectable classification accuracies. This proves that multispectral imaging is a good enough option as it can be programmed to be highly specialised, costs less, has lower operation costs, and has the flexibility of being applied in specialised multispectral imaging, such as on a UAV drone. Having said this, it is important to note that samples used in this study were clean and manually prepared before analysis, which is not the state in which rocks are found in the field, due to dirt and other matter. Therefore, classification accuracy variations in our envisioned identification of these rocks in the field, compared to the study's attained results, are likely to exist;
- Through ML, we can analyse and classify multispectral signatures produced by rocks and minerals with high accuracies. By finding the right model for a particular dataset, subsequent related data is relatively easier to classify as the training data always assists the model in future predictions as proven;

- With our proposed combined system, we have proved that any industry looking to cut spectral data (or equivalent) analysis costs whilst still retaining high classification accuracies, DR via a feature selection supervised NCA algorithm to specify the most discriminative bands, and verifying the viability of selected bands via ML, thereafter employing these 5-bands (or more, depending on application) in future specialised classifications, could potentially be the key to achieving several system design optimisations;
- Via a post-NCA 5-band rock and mineral classification specialised multispectral camera mounted on a UVA drone, such as the ‘DJI P4 Multispectral drone used in agricultural applications’, there is a plethora of applications in which this specialised technology could find potential use. This, as a result, minimises purchase, operation and data interpretation costs as compared to a hyperspectral imaging system. This could aid in remote sensing from long distances without the need for physical presence, as well as rapid in situ assessments of the state of the environment via the UAV drone, possibilities are endless.
- Lastly, there is potential to employ such a post-NCA specialised multispectral camera in the frequent monitoring of mine dams. This would allow quicker assessment of contaminants based on spectral signatures produced by unexpected and/or anticipated metal contaminants. Hence, we deem this proposed system viable in all mining-related stages, from exploration, operation and closure.

3.6. Conclusions

There are a number of optimizations this study was able to achieve. Reduction of storage capacity required to store and handle a database via NCA dimensionality reduction. Moreover, with post NCA specialized multispectral imaging, respectable classification accuracies were

attained, proving that multispectral imaging is a good option as it can be designed to be highly specialized for a given rock database. This quality gives it the flexibility to be applied in specialized rock multispectral imaging such as on a UAV drone (as will be discussed in Chapter 4). From NCA, it can thus be concluded that the most discriminative 5 multispectral bands viable in the classification of igneous rocks such as granite, diorite, gabbro, granodiorite, rhyolite, andesite, basalt and dacite, are bands with the following wavelengths: 441 nm, 535 nm, 741 nm, 791 nm and 897 nm.

In addition, the proposed system shows that there is an undoubted correlation between the NCA 2D spectral band plots with the outputs presented by the quantitative and highly objective ML models. Using the 5 NCA defined bands, the best performing model for whole-rock dataset classification was Cubic SVM with a global accuracy and per class precision of 70.9% and 72% respectively. When performing optimizations for each of the rocks against others within the database using 8 different models, it was found that the average global accuracy and average individual rock TPR outputs were 95.4% and 91.2% respectively. This suggests that the proposed system works seamlessly in deducing the spectral relationships between different rocks. With this proposed method, there is no need to change or re-determine the most intrinsic bands to discriminate rocks with emphasis on one particular rock, only the ML models. Lastly, the proposed system is highly sustainable as optimizations only take place on the ML models, which, is in line with the SDGs especially since this study is centralized around the development of a specialized multispectral UAV drone. Applying the same method in classifying minerals and other subject database classification problems has the potential to elevate such rock and/or mineral focused industries towards more sustainable practices.

CHAPTER 4: Capabilities of a Multispectral Imaging UAV Drone in Identifying Minerals via SAM and AI Techniques: A Case Study on Magnetite Iron Sands

In an attempt to classify rocks and/or minerals based on subject-specific multispectral bands as presented in Chapter 3, the following limitations in the methodology were realised: one is not always availed the opportunity to fine-tune feature bands to their required specification due to mass production of spectral imaging apparatus; machine learning models are not as superior as deep learning models. Therefore, in this chapter, a 6 multispectral bands UAV drone is flown at 3 different flight elevations in an attempt to perform mineral classification of magnetite iron sand. Based on the spectral angle analysis results at each elevation, machine learning and deep learning models will be used in ascertaining the classification capabilities of this system.

4.1. Introduction

The mining industry has been no stranger to the introduction of unmanned machines such as automated haul trucks in the attempt to improve safety and ore tracking abilities has been seen (Sinaice et al., 2021; Gaffey and Bhardwaj, 2020). 3D laser scanning of mines in order to assess the current state of a mine to enable better planning for the future has also been a common occurrence (Gaffey and Bhardwaj 2020; Heinz-H. Erbe et al., 2004; Mohajane et al., 2017). With regards to rocks and minerals, the application of automated identifications via spectral imaging is still a ‘hot topic’. The reason being, as demonstrated in Chapters 2 and 3, high resolving power requires multitudes of information processing resources.

With such high requirements in terms of time and sophisticated computational resources, it is difficult to perform rapid field spectral imaging via hundreds of spectral bands. Part of this reason is, the need to process multitudes of redundant bands which do not

necessarily improve the overall subject classification capabilities (Hu et al., 2021) Coupled with the weight constraint, it is even more difficult to employ high dimensional imaging technologies in aerial assessments of a site at considerable spatial areas and resolutions (Ganesh Kannan, 2017).

On the other hand, research has shown that the application of a few specialized multispectral imaging bands to classify rocks and minerals offers similar high subject resolving power (Weyermann et al., 2009). Specialized multispectral bands whose dimensionality has been reduced from hyperspectral imaging eliminate the said hyperspectral imaging disadvantages (Hu et al., 2021), for this reason, this study employs a 6 bands DJI P4 multispectral drone. Studies aimed at employing unmanned automated vehicles (UAVs) such as drones to identify certain rocks or minerals in mines are important as they offer a plethora of advantages (Rauhala et al., 2017; Martelet et al., 2017). Despite this, it is difficult to perform a thorough mine site rock or mineral assessment via a visible light camera-mounted drone. This is due to the fact that such cameras do not collect the intrinsic characteristics of rocks and minerals beyond the visible light spectrum (Sinaice et al., 2021; Martelet et al., 2021).

Mohajane et al. (2017), employed a method which incorporated remote collection of vegetation data via a multispectral camera mounted UAV drone in order to identify certain vegetation species. With modifications and improvements to this methodology, a novel method by which rocks and/or minerals can be identified in rapid, large scale areas with detailed field assessments was born. This proposed method combines multispectral UAV drone technology with Spectral Angle Mapping (SAM), ML and DL algorithms to automatically identify magnetite iron sands. The potential advantages of this proposed system are; The UAV possesses multiple spectral sensors which all capture information pertaining to a scene at the same time, this results in reduced exposure times for each image, which in turn ensures one captures cleaner images without blur, and less heating of the sensors.

Since the UAV drone spectral sensor comes pre-set with a few spectral dimensionalities to process, applying SAM becomes an advantage as it does not require the UAV to be specialized in magnetite identification. SAM takes advantage of the pre-existing spectral bands by assessing the difference between a reference subject's (magnetite) spectra characteristics with those similar or different to it in an image scene (Shafri et al, 2007; Girouard et al., 2004). AI algorithms such as ML and DL possess great spectral image classification power (Chauhan et al., 2022; Hartog et al., 2021), allowing one to resolve qualitative as well as quantitative data in an objective and understandable manner, making it highly eligible in multiple industry applications.

This combined system, has the potential to optimize several aspects of the mining chain, hence the motivation for this study. The main objective of this study is to assess an efficient approach for the automatic identification of magnetite iron sands. For this purpose, investigations on the viability of a multispectral camera mounted UAV drone will be discussed. Positive results of this research, assessed via SAM and AI models would aid in ascertaining the feasibility of field applications.

The study area, Kamaiso, is located along the west coast of Yamagata prefecture bounded to the left by the Japan sea. This site is a magnetite iron sand placer deposit which is said to have been a result of volcanic activity by Mt. Chokai estimated to have taken place 600 000 years ago (Kobayashi et al., 2019). With ore grades declining worldwide, it makes sense to explore the possibility of mining easily accessible placer deposits such as those in Kamaiso (Nguyen et al., 2018). These present an opportunity to maximize profit margins depending on the amount of resources present. Deposits located in coastal areas are rather difficult to quantify due to their close proximity to the sea. Aerial methods such as the employment of UAV drones present an alternative way of exploring and quantifying target resources within this area effectively (Beretta et al., 2019). Figure 4.1 is a map showing a 30 m × 90 m area from which

experiments were conducted in an attempt to apply UAV drone technology in identifying magnetite iron sands.

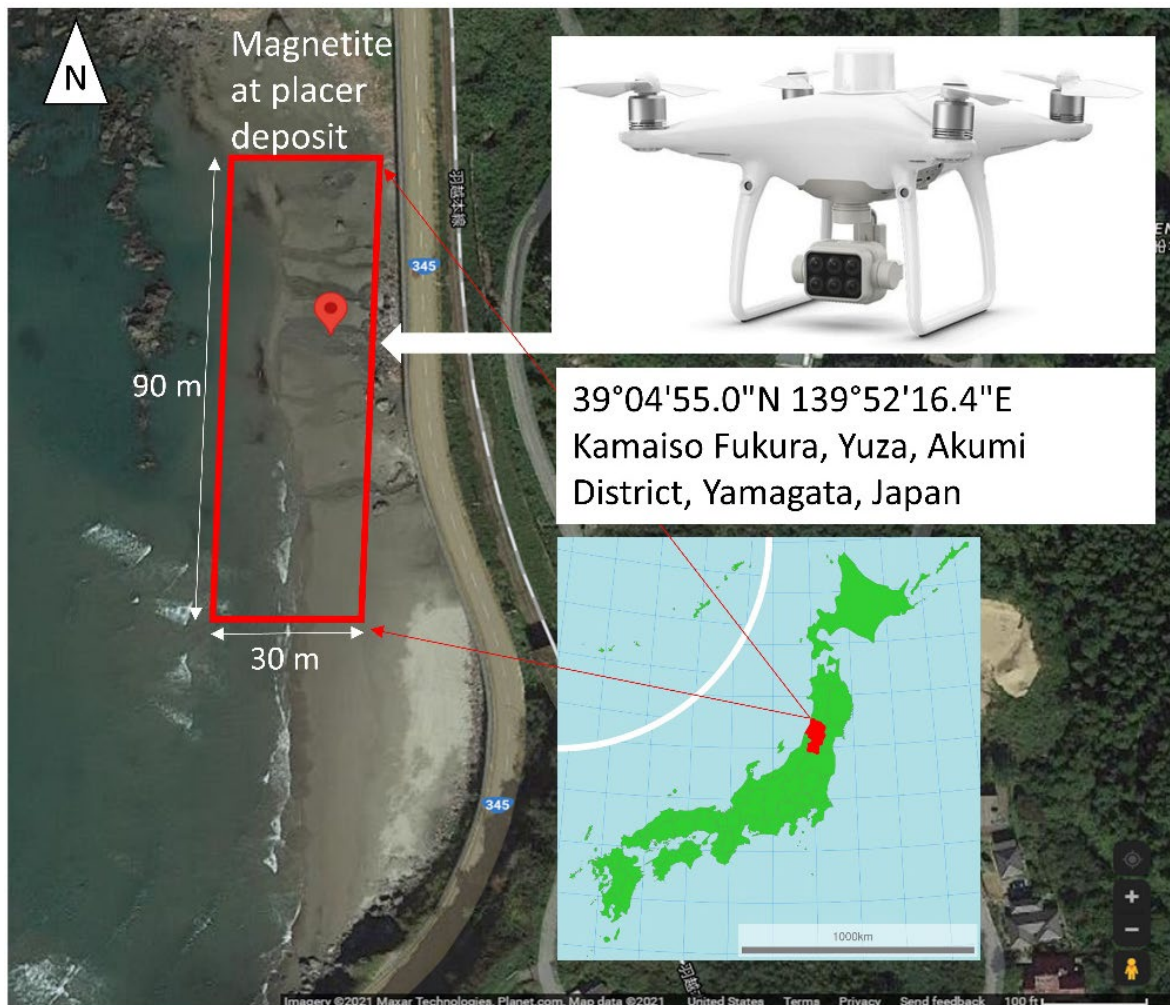


Figure 4.1: Map showing Kamaiso magnetite iron sand placer deposits. Red polygon represents the 30m by 90 m study area within which the UAV drone shown was flown. Map acquired from: Google maps (2021).

4.2. Methodological Strategies for SAM and AI Integration

4.2.1. UAV Drone Mounted Multispectral Imaging

Drone technology has evolved over the years, with recent developments catering to specialized industrial applications. One of the advantages of UAV drones is the protection of human life as sites can be assessed from a remote area (Heinz et al., 2004; Beretta et al., 2019;

Jackisch et al., 2019). In addition, camera-mounted drones aid in real-time assessments of sites via visual feed. This feed can be in the form of real, false or manipulated colours which are preprogrammed to represent a certain phenomenon understood by the operator (Mohajane et al., 2017).

It is said that hyperspectral imaging is arguably one of the best methods by which rocks and minerals can be identified through their spectral characteristics (Fox et al., 2017). However, van de Meer et al. (2012), have been able to attain high classification accuracy outputs in similar rock identification problems via multispectral imaging. Motivated by the demonstrated multispectral capabilities, this paper employs a DJI P4 Multispectral camera mounted UAV drone released in September 2019 (Figure 4.2). To achieve centimetre level position accuracy, the drone has a real-time kinematics (RTK) module attached to it. In addition, the six cameras are 1/2.9-inch (complementary metal-oxide-semiconductor) CMOS sensors, all at 2 megapixels with a global shutter, on a 3-axis stabilized gimbal to ensure accurate multispectral image capturing at spatial resolutions as high as 0.1 cm/pixel. The spectral sensor specifications are as follows: Blue: 450 nm \pm 16 nm, Green: 560 nm \pm 16 nm, Red: 650 nm \pm 16 nm, Red Edge: 730 nm \pm 16 nm, Near-Infrared: 840 nm \pm 26 nm which are all captured as TIFF image files. The drone moreover boasts a 62.7° field of view, a net weight of 468 g and an RGB camera which facilitates the extraction of magnetite iron sand spectral information in the visible light spectral range of 400-700 nm as a JPG image. This, consequently makes the system effective in a wide range of electromagnetic spectra within the visible-near-infrared range (VNIR) with a total of 6 multispectral bands.

The drone flight height plan was set to 3 different elevations so as to investigate the effect of the ground resolution, proximity to the subject, and the ease of flying. By investigating these attributes, it would be easier to find the optimum height at which magnetite iron sand identification can be performed effectively. The 3 UAV flight elevation heights measured from

the camera sensor to the subject were 2 m, 10 m and 20 m. The drone was moreover set such that the aerial multispectral imaging procedure is automatically performed at intervals that ensured an equal amount of area ($30 \text{ m} \times 90 \text{ m}$) was captured by the end of each flight mission. In principle, this meant that more multispectral images were to be captured at 2 m, followed by 10 m, with the least number being at 20 m. As a flight setting procedure, the drone was flown over the area in order to pre-program the flight plan and ensure the drone flies within the desired area, direction and height before allowing it to perform all these manoeuvres autonomously from a remote area.

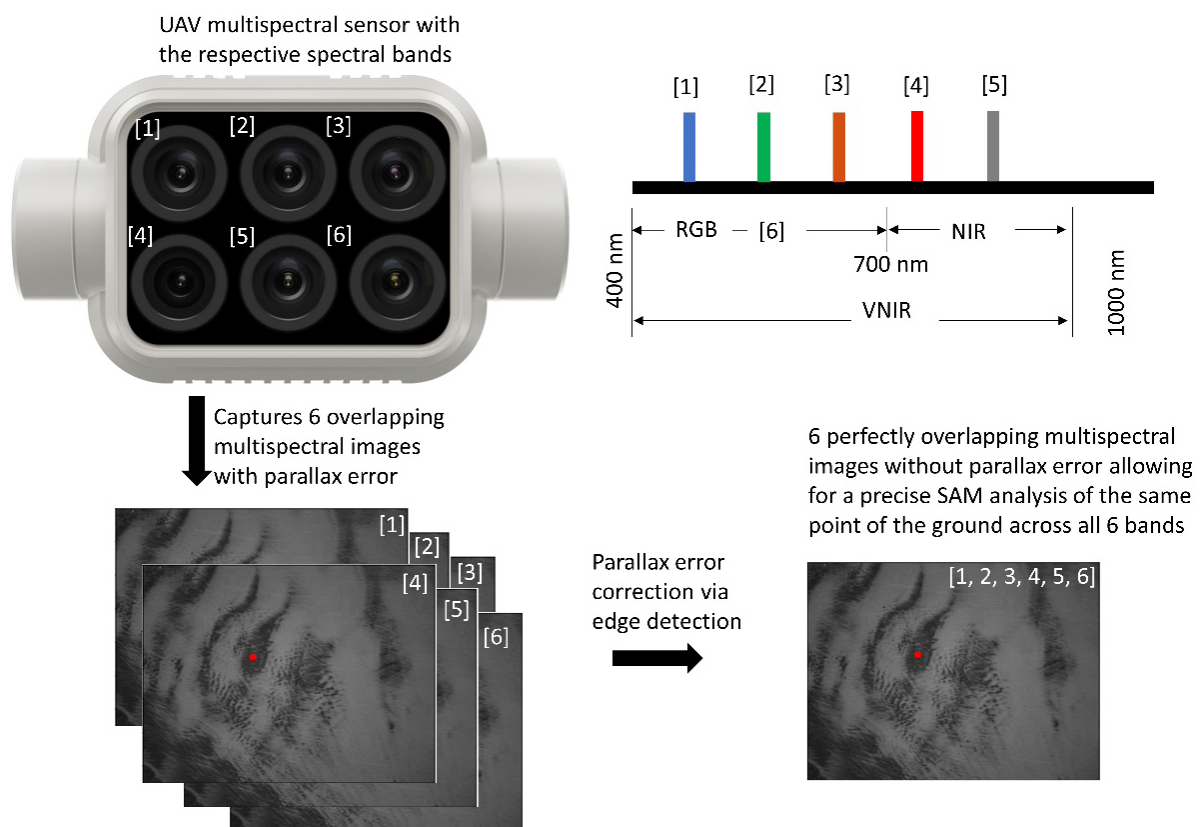


Figure 4.2: The 6 bands multispectral sensor with a 62.7° field of view; [1] Blue: $450 \text{ nm} \pm 16 \text{ nm}$, [2] Green: $560 \text{ nm} \pm 16 \text{ nm}$, [3] Red: $650 \text{ nm} \pm 16 \text{ nm}$, [4] Red Edge: $730 \text{ nm} \pm 16 \text{ nm}$, [5] Near Infrared: $840 \text{ nm} \pm 26 \text{ nm}$ and [6] RGB camera: $400\text{-}1000 \text{ nm}$ represent the multispectral sensor capabilities. Images captured are corrected for parallax error via an edge detection method. The red point is the reference area from which magnetite iron sands are known to exist.

4.2.2. Parallax Error Correction

Since there is a small distance between the 6 spectral sensors of the drone, parallax error always needs to be corrected for to ensure all sensors are aimed at the same image scene depending on the UAV flight height. At low altitudes, the parallax error is significantly higher relative to higher flight altitudes (Ono, 1995). There are several methods such as the Hough transform and least-squares techniques amongst others which can be applied to perform this task aimed at interpolating the images into perfectly overlapping images (Ono, 1995; Laurence, 2012). However, according to Laurence (2012), the edge detection method performs well as it takes into account the individual pixels within each of the 6 multispectral images to be overlapped. It calculates the centres of gravity and automatically nullifies the differences in position, thereby creating a perfect overlay of images (Laurence, 2012), hence the application of this method in this study.

It should be noted, however, that in order to assume a perfect overlay, each of the 6 images loses a small part of its edges. The lower the UAV elevation, the more data is lost relative to higher flight elevations. The data loss depends on the distance from the drone sensor to the subject, as well as the distance between sensors within the drone, and so parallax error always needs to be corrected. Though a small percentage of data is lost per image during parallax correction, this is not the case when considering the study area as a whole. The reason for this is, that the UAV flight missions were set up such that each captured image slightly overlaps those around it. This, in principle, ensures zero data loss within the 30 m × 90 m study area, with only the image regions outside the study area experiencing data loss.

4.2.3. A Scrutiny of SAM Analysis

Mohajane et al. (2017), have employed several indexes in an attempt to perform rapid field vegetation classification based on a number of criteria. These included the intensity of certain vegetation colours and moisture content via SAM. Using the same principle, Zhang and Li (2014), have employed SAM as an index to classify lithology. SAM is a physically-based spectral classification that uses an n-dimensional angle to match pixels to reference spectra (Weyermann et al., 2009; Girouard et al., 2004; Yang et al., 2012). The algorithm determines the spectral similarity between spectra by calculating the angle between them, treating them as vectors in a space with dimensionality equal to the number of bands (Shafri et al., 2007), which in this study is 6. This technique, when used on calibrated reflectance data, is relatively insensitive to illumination and albedo effects (Girouard et al., 2004). This makes SAM highly applicable in multitudes of real-life field observations, which motivated the employment of this method in this study. In short, SAM compares the angle between the endmember spectrum vector and each pixel vector in n-dimensional space. Smaller angles represent closer matches to the reference spectrum (Zhang, and Li 2014). Pixels further away than the specified maximum angle threshold in radians are not classified as the reference spectrum of what is being sought after. Figure 4.3 illustrates the principle of SAM analysis.

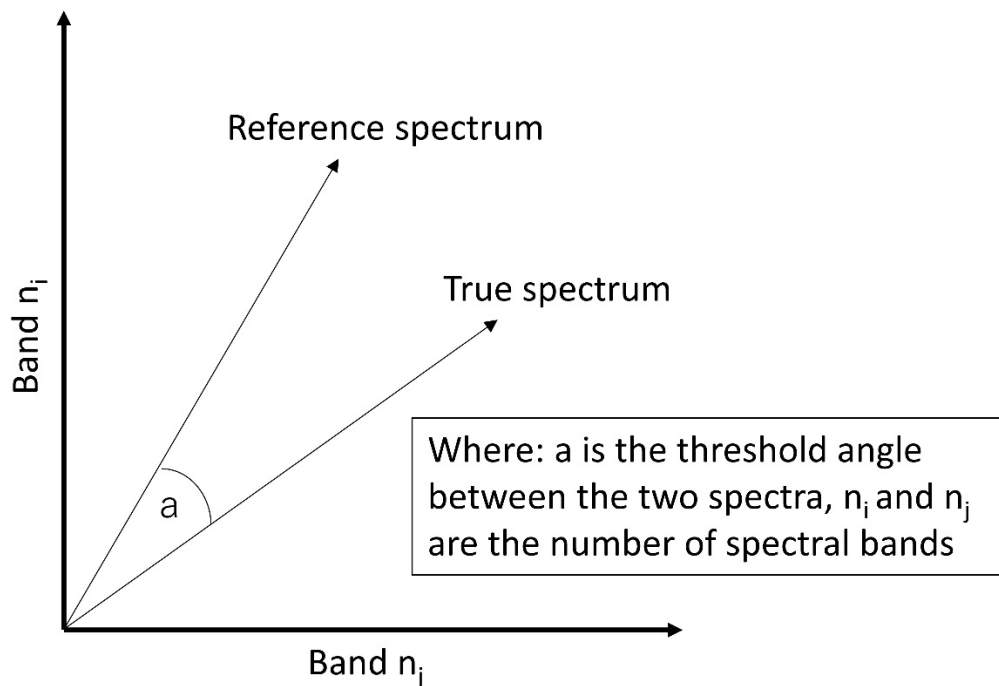


Figure 4.3: Schematic diagram showing the principle of SAM cosine similarity. Reference spectrum is what is sought after. Angle a is the cosine similarity threshold between a reference and a synthetic spectrum.

On the ground, the drone is linked to a tablet which receives captured data allowing for on-site SAM analysis and aiding in the identification of magnetite iron sands. Though best performed in the field, this operation can be performed in laboratory analytics. To perform SAM, each captured multispectral image is imported into a SAM operation algorithm such as python. Thereafter, the user pinpoints the area of importance which in this case was any area within the multispectral image scene known to be occupied by magnetite iron-sand. The algorithm then performs a cosine similarity computation for every pixel in each image scene to determine whether or not there are similarities between the reference and subsequent subjects (Weyermann et al., 2009). To determine the threshold from the determination of whether or not new subjects are similar or related to the reference, Equation 7 is used.

$$a = \cos^{-1} \left(\frac{t \times t_0}{\|t\| \times \|t_0\|} \right) \quad (7)$$

where a is the threshold for variables related to the reference, t_0 is the reference spectra, and t is the subject's spectra.

Having successfully stacked the 6 bands TIFF and JPG qualitative images, as well as performed SAM analysis, the images are then converted to CSV format. This data conversion provides quantitative values pertaining to magnetite iron sand spectral characteristics across the 6 multispectral bands, this data type is useful in training AI algorithms.

4.2.4. Benefits of Employing ML and DL AI Methods in Magnetite Identification

In order to determine regions of images where magnetite iron sand exists post-SAM analysis, ML and DL models are upheld techniques by which this task can be performed (Saha and Annamalai, 2021). This step involves pre-processing the data before training the AI algorithms. Pre-processing is important as it cleans the data and makes it easier for the algorithms to interpret it, for this study, the pre-processing step involved the extraction of the SAM segmentation maps per image. This simply means magnetite and non-magnetite post-SAM spectral variables, given their cosine similarity thresholds, are assigned labels so as to take advantage of supervised AI algorithms. Hence, this process is referred to as image segmentation and is simply defined as the labelling of each pixel in an image scene (Saha and Annamalai, 2021). Pixels within and outside the threshold are assigned magnetite and non-magnetite labels respectively.

Since SAM is mostly a visual interpretation, ground truthing is needed in order to employ AI algorithms. For this reason, the SAM segmentation map is extracted together with two ground truths for magnetite and non-magnetite pixels. Ground truths are image pixels known to be 100% occupied by magnetite and non-magnetite pixels per image. Since each

image is 6 bands deep, the result is a total of 12 ground truths. Ground truth for magnetite is defined as the target, whereas non-magnetite ground truth is defined as noise.

Labelled datasets guide and allow algorithms to take advantage of both the global and local structures of the data, which in turn results in quicker and more direct classifications (Sharma et al., 2021). This in essence means for each image, the CSV file contains labelled pixels for both magnetite iron sand (together with target ground truth), as well as non-magnetite beach sand (together with noise ground truth). Using this data as input, the algorithms are subsequently trained and outputs pertaining to the classification capabilities of the models in deducing magnetite iron sands and non-magnetite beach sand are presented.

4.3. Experimental and Analytical Results

4.3.1. In the field UAV Drone Analytics

Based on the flight history logs at the different flight elevation heights, 80, 32 and 8 multispectral images at 2 m, 10 m and 20 m respectively were captured (Table 4.1). The number of images is governed by the flight heights, as well as the 62.7° UAV field of view. From the number of images captured, the spatial resolution at each elevation can thus be resolved as shown in Figure 4.4. Given that each spectral image measures 1300 pixels × 1600 pixels, at 2 m, 10 m and 20 m, the spatial resolutions were 34 m², 84 m² and 338 m² respectively, each multiplied to cover the 2700 m² study area. Hence, it can be said that the higher the flight elevation, the lower the spatial resolution, the opposite being true at lower flight elevations.

Moreover, based on Figure 4.4 and Table 4.1 post-flight logs, it has been demonstrated that greater flight elevations allow for a wider area to be captured at a given time. This disregards the need to operate the UAV drone at close proximities to the subject where larger spatial coverage is required. This is a great advantage as it saves time, uses less power, and

requires less computational resources to process the numerous multispectral images. Though Table 4.1 demonstrates the implications of flying at the 3 different elevations, it does not communicate outputs pertaining to the actual identification of magnetite. This is a task meant for the SAM analysis and AI.

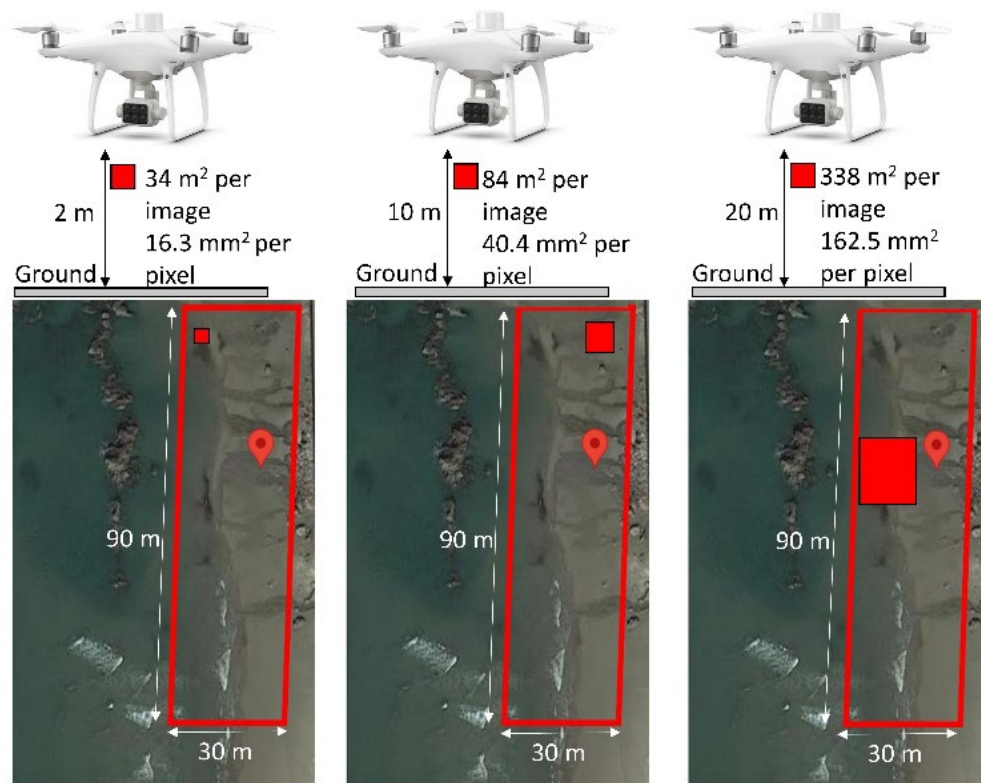


Figure 4.4: Illustration of the difference spatial resolutions of each image, attained from capturing multispectral images at 2 m, 10 m, and 20 m flight elevations.

Table 4.1: Multispectral UAV drone post flight logs from operating at 3 different flight elevations.

UAV drone flight elevation	Number of Images captured	Flight time (minutes: seconds)	Spatial area coverage (m ²)	Battery power consumed during mission (%)
2 meters	80	21: 32	34	69
10 meters	32	8: 23	84	29
20 meters	8	2: 08	338	7

4.3.2. Outputs Pertaining to SAM Analysis

Multispectral images were analyzed for the 3 flight elevations and the results show that by altering the reference cosine similarity value thresholds, an accurate mapping of the area can be achieved. This is in agreement with Shafri et al. (2007), where altering their threshold values ensured better subject separation. From the visual analysis of Figure 4.5, it is clear to see that the SAM analysis seems to have performed well across all the 3 flight heights. The smaller the threshold, the smaller the mask, meaning less of the targeted magnetite iron sands are identified, resulting in none of the non-magnetite pixels being misidentified. On the other hand, the larger the threshold, the more magnetite iron sand pixels are identified. This however means non-magnetite pixels are likely to be identified as magnetite. To resolve this, one is required to alter the threshold such that the mask perfectly overlays the magnetite pixels only.

For this study, the best SAM cosine similarity threshold values from visual interpretation are 0.12, 0.13 and 0.17 for 2 m, 10 m and 20 m flight elevations respectively (Figure 4.5). As this is the case, it can therefore be said that distance from the sensor to the subject affects the nature of the results as the SAM value needed to be altered for each flight elevation. The lower the UAV drone, the lower the threshold required to identify magnetite iron sands, whilst the opposite was true at higher UAV drone flights. It should be noted that since the multispectral sensors are located at different positions of the multispectral camera (Figure 4.2), parallax error was accounted for as previously described in section 2.2. The result is a perfect overlay of all 6 multispectral images at each flight elevation.

Another assessment that can be made is, that the larger the threshold values, the more noise is introduced (Girouard et al., 2004). Such noise may be due to the presence of mini-ripples and shadows. These ripples tend to trick the SAM into assuming there is a similarity in image pixel characteristics between the actual reference subject and those exhibited by ripples

and shadows (Girouard et al., 2004). Though a visual assessment of the SAM mask illustrations seems rather qualitative, it can still be argued that this method provides a great amount of information pertaining to the location of a specific subject such as the magnetite iron sands. The application of the UAV drone coupled with SAM analysis has the potential to be employed in a plethora of applications within the mining industry. These include resource exploration, resource mapping, resource estimation, mine site monitoring, and ore processing amongst others where quick and accurate separation of rocks and/or minerals is constantly performed.

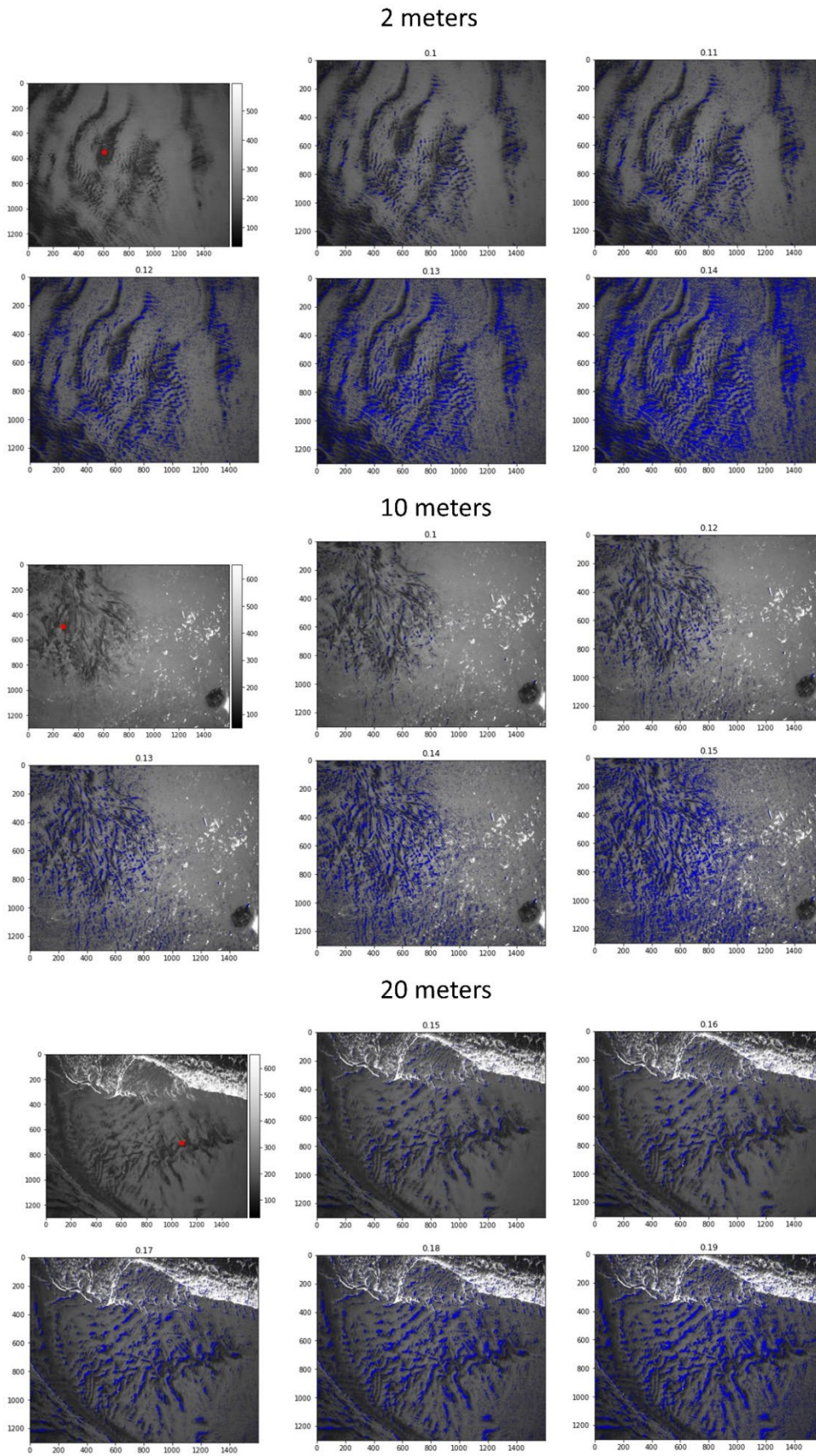


Figure 4.5: SAM analysis at 2 m, 10 m and 20 m UAV drone elevations at different reference spectral thresholds. The red points represent the user selected reference point known to be magnetite (pre-SAM), whilst the blue overlay represent areas within the threshold limit thought to be magnetite (post SAM cosine similarity). The best threshold cosine similarities are 0.12, 0.13 and 0.17 at 2 m, 10 m and 20 m respectively. The x and y axis represent the size of each captured multispectral image. The bar on the right of each first image represent the variation in spectral intensities present in each captured image.

4.3.3. Application of AI Methods in Magnetite Spectral Classification post SAM

To eliminate subjectivity pertaining to the visual interpretation of SAM analysis masks, AI algorithms are a trusted way in which human error can be eliminated in an objective analysis of data (Saha and Annamalai, 2021). The mask data from the 0.12, 0.13 and 0.17 SAM cosine similarity thresholds, for 2 m, 10 m and 20 m flight elevations respectively (labelled as target), is mixed with the rest of the non-masked pixel data (labelled as noise) so as to build an input dataset. Figure 4.6 and 4.7 are representations of how the SAM masks were extracted, hence creating the labelled segmentation maps. Using the quantitative labelled segmentation maps as demonstrated in Figure 4.6, input datasets are ready to be employed in training and testing the supervised ML and DL algorithms. The output variables are predicted or classified from the training database (Sharma et al., 2021). This means, that algorithms will try to learn some patterns in the data during training, so as to implement these learnt patterns within the testing dataset (Chauhan et al., 2022). This, therefore, provides results in relation to the learnt patterns.

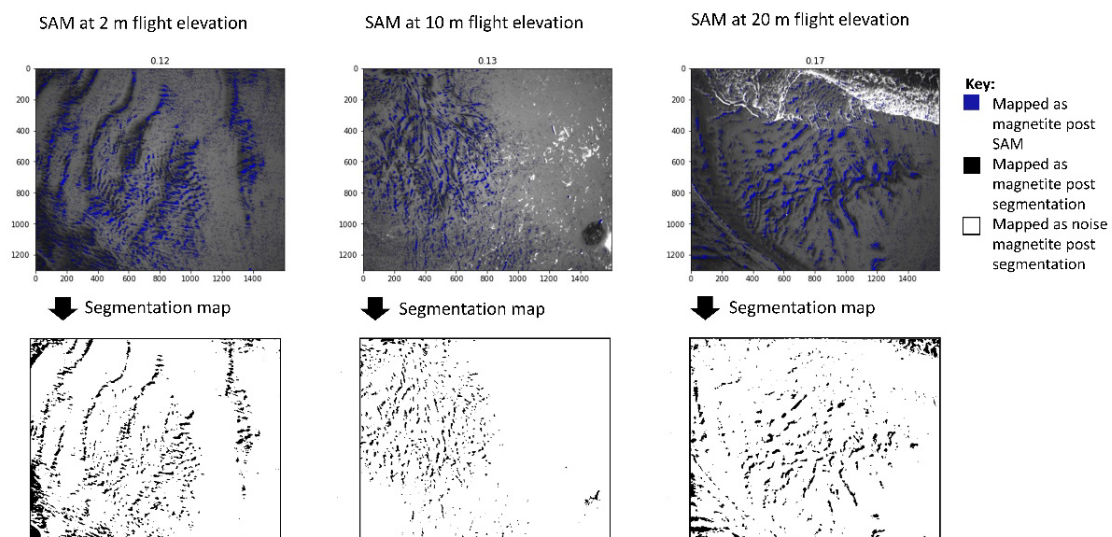


Figure 4.6: Extraction of segmentation maps used to create a magnetite iron sand database. Segmentation maps at each UAV flight elevation are based on the 0.12, 0.13 and 0.17 cosine similarity thresholds at 2 m, 10 m and 20 m.

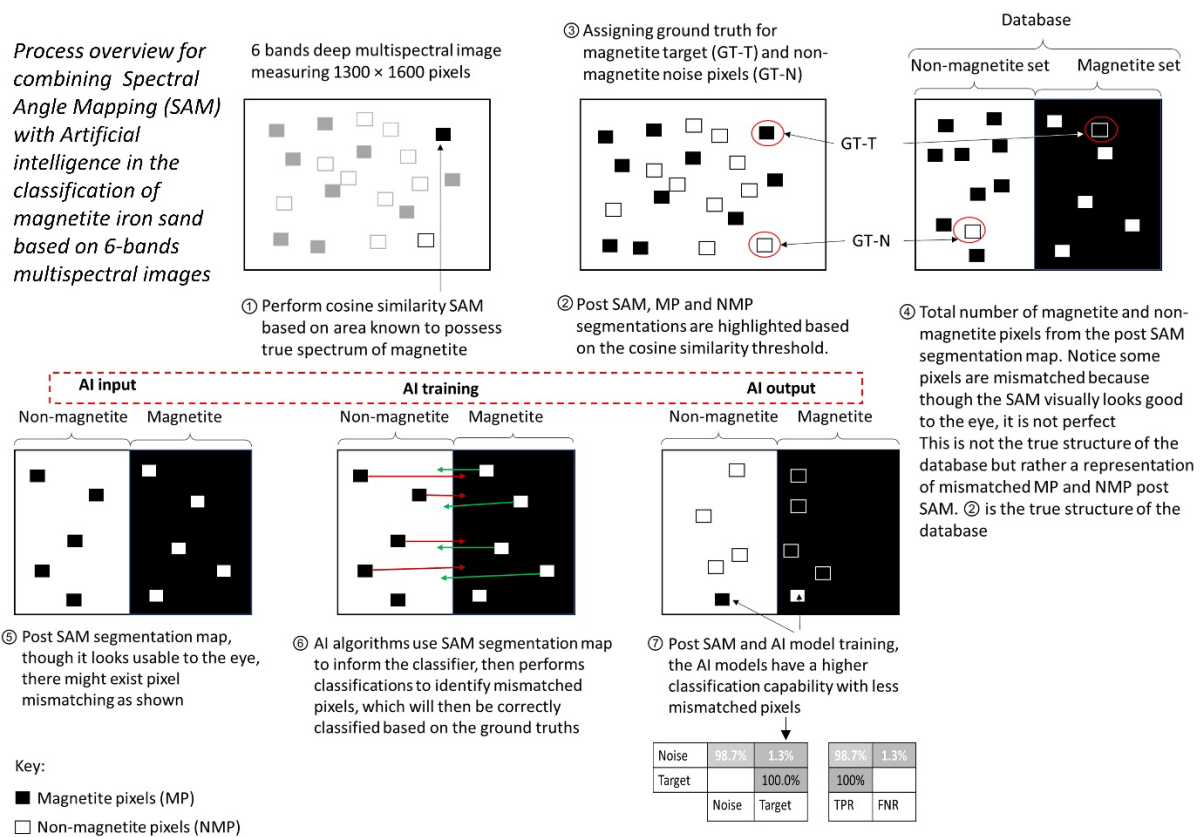


Figure 4.7: Extraction of segmentation maps used to create a magnetite iron sand database. Proposed process overview with emphasis on how data extracted from spectral angle mapping cosine similarities is segmented, assigned ground truths, and used in training artificially intelligent algorithms in the classification of magnetite iron sand.

At 2 m flight elevation, the total dataset size was 998,400,000, derived from the product of image sizes (1300×1600), the number of multispectral bands (6), and the number of captured images (80). At 10 m flight elevation, the total dataset size was 399,360,000, derived from the product of image sizes (1300×1600), the number of multispectral bands (6), and the number of captured images (32). Lastly, at 20 m flight elevation, the total dataset size was 99,840,000, derived from the product of image sizes (1300×1600), the number of multispectral bands (6), and the number of captured images (8).

These dataset sizes were however too large to run using the computational resources employed in this study (32 GB memory, Intel i7-8750H CPU @ 2.2 GHz processor, NVIDIA

GeForce GTX 1060 graphics, Windows 10, 64 bits operating system). To counter this, Figure 4.8 demonstrates our approach. At 2 m flight elevation, the input dataset size used to train each algorithm was 12,480,000, derived from the product of image sizes (1300×1600), and the number of multispectral bands (6). Since 80 of such datasets exist, 80 algorithms were trained, and the best performing model from the rest was chosen as the most viable. The same approach was applied at 10 m and 20 m flight elevations, the difference being the number of times (32 times and 8 times respectively) training was performed, this number corresponding to the number of images captured. With this approach, all image datasets still get to participate in the training of the various algorithms, the training times are quicker, and it requires less computational resources.

Model training approach: Train each image dataset and select best performing model

	Image size and no# of bands	Input dataset per algorithm	No# of images	Final model
2 m:	$1300 \times 1600 \times 6$	= 12,480,000	80	Choose best model
10 m:	$1300 \times 1600 \times 6$	= 12,480,000	32	Choose best model
20 m:	$1300 \times 1600 \times 6$	= 12,480,000	8	Choose best model

Figure 4.8: Input dataset sizes used to train the machine learning and deep learning algorithms as well as selection of the best performing model at each UAV flight elevation.

4.3.3.1 Classification via Machine Learning Models

The input dataset sizes for training and testing variables for each of the ML algorithms stood at 12,480,000 (from Figure 4.8) for each of the three flight elevation heights. Moreover, a 5-fold-cross-validation was used at all times in order to ensure that every observation ($2,496,000 \times 5$) from the original dataset (12,480,000) has the chance of appearing in training and test sets. Therefore, this method generally results in a less biased model compared to other validation methods (Sharma et al., 2021).

Using MATLAB R2020b classification learner Machine Learning toolbox, multiple ML algorithms were evaluated. Classification performance was presented in terms of global accuracy, average per-class precision, and time taken to train the algorithm. These attributes are said to be among the most important classification evaluation criteria (Saha and Annamalai, 2021). These said attributes, except the time taken to train the models, govern industrial applicability, and the overall viability of the algorithm in solving the task at hand (Sinaice et al., 2020). Table 4.2 is a compilation of the top 3 performing ML models for the 3 multispectral UAV drone flight elevations post-SAM. It quantitatively demonstrates the differences in classification capabilities based on differences in flight elevation. In definition, global accuracy refers to the validation accuracy acquired during training. Average per-class precision refers to the individual magnetite iron sands (target) and the beach sand (noise) classification score averages in testing the models. Lastly, training time refers to elapsed time in training the models to classify the datasets based on the presence of magnetite iron sand. These are important performance variables in comparing the different ML as well as DL models given their intended application.

Results from the ML models in Table 4.2 show that the best performing model was Ensemble (RUS Boosted Trees) for 2 m flight elevation. This model acquired the best outputs in terms of global accuracy (85.7%), per-class precision (84.5%), and training time (5.8 seconds). On the other hand, the Tree (Course-tree) model performed the best for 10 m flight elevation. This model acquired the best outputs in terms of global accuracy (78.7%), per-class precision (83.4%), and training time (1 second). Lastly, the Tree (Course-tree) model performed the best for 20 m flight elevation. This model acquired the best outputs in terms of global accuracy (85.7%), per-class precision (88.9%), and training time (1 second).

From the results compiled in Table 4.2, the differences in accuracies acquired and elapsed times when training the ML models for the 3 flight heights can moreover be

appreciated. The reason is, that this confirms the hypothesis which stated that with the automatic magnetite iron sand identification system, rapid run times and good accuracies are potentially attainable. This is of course without compromise to the fundamental differences in the multispectral characteristics of magnetite iron sands and the surrounding beach sand.

Table 4.2: Top 3 machine learning classification model comparisons at 2 m, 10 m and 20 m UAV flight elevations based 0.12, 0.13 and 0.17 SAM cosine similarity thresholds respectively.

UAV drone flight elevation	Machine Learning model	Global Accuracy (%)	Average per-class precision (%)	Training time (seconds)
2 meters	Ensemble (Bagged Trees)	78.6	83.4	8.4
	Ensemble (Subspace KNN)	71.4	77.8	8.1
	Ensemble (RUS Boosted Trees)	85.7	84.5	5.8
10 meters	Tree (Fine-tree)	78.6	83.4	1.5
	Tree (Medium-tree)	78.6	83.4	1.0
	Tree (Course-tree)	78.6	83.4	0.9
20 meters	Tree (Fine-tree)	85.7	88.9	1.9
	Tree (Medium-tree)	85.7	88.9	1.2
	Tree (Course-tree)	85.7	88.9	1.0

At 2 m, the ML model has an 80% TPR, which may not be considered satisfactory as target data should have had a 100% target return (Figure 4.9). This means 20% of the target pixels were thought to have been noise, suggesting the model at 2 m did not perform well at discriminating magnetite iron sand pixels from the rest of the non-target pixels. This in essence means flying and collecting data at this elevation may not be the best practice. At 10 m, the target has a 100% TPR, meaning the target pixels were undisturbed, suggesting the target output did not include any noise. The same can be said for the 20 m flight elevation, making these flight elevations the most viable of the 3. At 20 m however, the model has a higher noise TRP of 77.8% compared to the 67.7% at 10 m. This suggests the Tree (Course-tree) model at

20 m performed better at discriminating the targeted magnetite iron sand data compared to the other 2 flight elevations model outputs.

Another assessment that can be drawn from the Figure 4.9 confusion matrix is the average per-class precisions of 84,5%, 83.4% and 88.9% at 2 m, 10 m and 20 m flight elevations respectively; at 20 m, the model is still seen to perform better. It can consequently be said that the best classification ML model for this magnetite iron sands identification problem is Tree (Course tress) at 20 m.

2 m: Ensemble (RUS booted trees)				
Noise	88.9%	11.1%	88.9%	11.1%
Target	20.0%	80.0%	80.0%	20.0%
	Noise	Target	TPR	FNR

10 m: Tree (Course trees)				
Noise	66.7%	33.3%	67.7%	33.3%
Target		100%	100%	
	Noise	Target	TPR	FNR

20 m: Trees (Course trees)				
Noise	77.8%	22.2%	77.8%	22.2%
Target		100.0%	100%	
	Noise	Target	TPR	FNR

Figure 4.9: Machine learning confusion matrices from Ensemble (RUS Boosted Trees) at 2 m UAV drone elevation, Tree (Course-tree) at 10 m UAV drone elevation, and Tree (Course-tree) at 20 m UAV drone.

4.3.3.2 Classification via Deep Learning CNN

A convolution applies a filter over the multispectral data per band. Unlike visual imagery data with height and width, the filters in a one dimensional CNN exhibit a 1D (spectral intensity) architecture instead of 2D as with normal visual images. Hence the motivation to employ this type of CNN in this study as the datasets contain 6 bands deep spectral intensity data that require a 1D data processing method.

The input dataset sizes for training and testing variables for each of the algorithms stood at 12,480,000 (from Figure 4.8) for each of the three flight elevations prior to obtaining the highest performing model. However, to train the 1D CNN, the spectral data was pre-processed in the following ratios: 70% (9,736,000) designated to training, 15% (1,872,000) validation and the remaining 15% (1,872,000) to testing. Moreover, all models were trained with Adam optimizer which is said to have the best accuracy in enhancing CNN abilities in classification (Chauhan et al., 2022). A learning rate of 0.001, a batch size of 128, and 25 epochs were also employed. As with ML, the 1D CNN training processes were conducted using the MATLAB 2020b deep learning toolbox with the model selection at each flight elevation governed by global accuracy, average per class precision, and time taken to train each 1D CNN algorithm.

At 2 m, 10 m and 20 m flight elevations, 80, 32 and 8 algorithms were trained and one model from the multitudes of trained models was selected as performed in training the ML models. Table 4.3 is a compilation of the best performing models at each of the 3 flight elevations. Results from the DL 1D CNN models in Table 4.3 show that the global accuracies, as well as the average per-class precisions, have an average of 99.8% and 99.3% respectively. Moreover, based on global accuracy, the 1D CNN performs the same at 2 m and 10 m at 99.9%, followed by 20 m at 99.7%. However, the trend changes in considering the average per-class precision where the best performing model is the 1 D CNN at 2 m (99.8%), followed by 20 m (99.4%) and 10 m (98.7%). Lastly, at 2 m, the 1D CNN takes a longer time to train (78 seconds) compared to the 1D CNNs at 10 m (45 seconds) and 20 m (68 seconds); this could suggest, that the longer the training time, the higher the average per-class precision for this DL classification problem.

Table 4.3: Deep learning one dimensional convolution neural network classification model comparisons at 2 m, 10 m and 20 m UAV flight elevations based 0.12, 0.13 and 0.17 SAM cosine similarity thresholds respectively.

Flight height	Global accuracy (%)	Average per-class precision (%)	Training time (seconds)
2 meters	99.9%	99.8%	78
10 meters	99.9%	98.7%	45
20 meters	99.7%	99.4%	68

To further assess the viability of the best performing 1D CNN models for the 3 flight elevations, Figure 4.10 presents TPR and FNR performance metrics (Equations 1 and 2). At 2 m, 10 m and 20 m, the 1D CNN models have a 100% TPR for magnetite iron sand (target). This suggests the models are highly capable of deducing magnetite iron sands from the combination of magnetite iron sands (target) and beach sand (noise). On the other hand, the 1D CNN models attained a 99.6%, 97.4% and 98.7% TPR for beach sand (noise) at 2 m, 10 m and 20 m respectively, which is considerably high. This suggests the models are all highly effective at separating reference (magnetite iron sand) spectra from other (beach sand) spectra from within the image scenes.

2 m: 1D CNN

Noise	99.6%	0.4%
Target		100%
	Noise	Target

99.6%	0.4%
100%	
TPR	FNR

10 m: 1D CNN

Noise	97.4%	2.6%
Target		100%
	Noise	Target

97.4%	2.6%
100%	
TPR	FNR

20 m: 1D CNN

Noise	98.7%	1.3%
Target		100.0%
	Noise	Target

98.7%	1.3%
100%	
TPR	FNR

Figure 4.10: Deep learning one dimensional convolution neural network confusion matrices at 2 m, 10 m and 20 m UAV drone elevation.

4.4. Discussion

In a study by Gholami et al. (2012), they applied independent component analysis (ICA) in remote sensing data processing based on satellite data to map an area and attained good results. However, the differences between their method and ours are as follows; with the ICA method, they reduced the dimensionality of spectral bands from 6 bands to 2 bands. However, researchers van der Meer et al. (2012) and Zhang (2014), mention that higher dimensionalities are relatively superior in deducing materials as they retain the original data structure. Hence, our study applied SAM, which retains the full 6 bands data structure. In addition, our methodology employs a UAV drone, which allows for the collection of varied, as well as higher spatial resolution data. For example, at 2 m flight elevation, our spatial resolution is 0.4 cm/pixel, as opposed to their fixed satellite resolution of 30 m/pixel. Considering our 30 m × 90 m study area, their spatial resolution is rather inadequate. Lastly, we employ super-vised DL 1D CNN classification algorithms which are known to be state of the art in imagery data classification problems. As pointed out by Sharma and Sharma (2021), supervised learning

algorithms are superior unsupervised ML methods such as ICA, especially in cases where the output variables (magnetite or non-magnetite) are known, as it is the case in this study.

Based on this study's findings, it was realised that the SAM cosine similarity thresholds require slight adjustments relevant for each UAV flight elevation. With the increase in elevation from 2 m, 10 m to 20 m, these thresholds vary from 0.12, 0.13 to 0.17 respectively. Though these SAM cosine similarities vary, the ability of the SAM in differentiating the targeted magnetite iron sand from non-magnetite beach sand remains relatively unchanged from visual analysis. This is demonstrated by the masks at each flight elevation which seem to flawlessly overlap the sought after magnetite iron sands (Figure 5), as well as the high ground truths supported by AI classification capabilities. With respect to the UAV drone post-flight logs and the typical size of surface mines, it would be in the best interest of engineers to perform mineral identification practices at higher elevations such as 20 m. The reason being, the UAV is not as challenged in terms of power consumption, elapsed capturing time, number of images to capture, and area coverage; as at lower elevations (Table 4.1).

Figure 4.11 and 4.12 are summarized comparisons between the ML and DL CNN model classification capabilities as well as the length of time required to train each model. Based on global accuracies, the CNN models perform better than the ML models across all 3 flight elevations. With ML, the attained global accuracies were 85.7%, 78.6% and 85.7% at 2 m, 10 m and 20 m flight elevations, whilst with the CNN, attained global accuracies were 99.9%, 99.9% and 99.7% respectively. A look into the attained per-class precisions shows that with the ML models, 84.5%, 83.4%, and 89.9% classification capabilities were attained at 2 m, 10 m and 20 m flight elevations. These model classification capabilities are different from the 99.9%, 99.9% and 99.7% attained via the CNN at 2 m, 10 m and 20 m respectively. Therefore, it can be said that based on the global accuracies as well as the per-class precisions (Figure

4.11), model capabilities show that the 1D CNNs employed in this study are far superior in classifying the magnetite iron sands than the ML models.

From Figure 4.12, one is able to appreciate the differences in the times required to train the AI models. With ML models, training times are shorter (5.8, 0.9 and 1.0 seconds at 2 m, 10 m and 20 m respectively) compared to those of the CNN models (78, 45 and 68 seconds at 2 m, 10 m and 20 m respectively). Though the ML model training times seem relatively more efficient, the time taken to train a model is not what governs its industrial applicability. Training duration merely communicates the time it took to turn an algorithm into a model.

Lastly, considering the UAV flight logs, as well as the AI model outputs in this study, one can come to the conclusion that the most effective UAV flight elevation is 20 m. At 20 m, one has a larger spatial area coverage, which eliminated the need to capture multitudes of images. Matching these variables with the attained AI model classifications shows that, the best classifier at this UAV flight elevation in identifying magnetite iron sands is the 1D CNN.

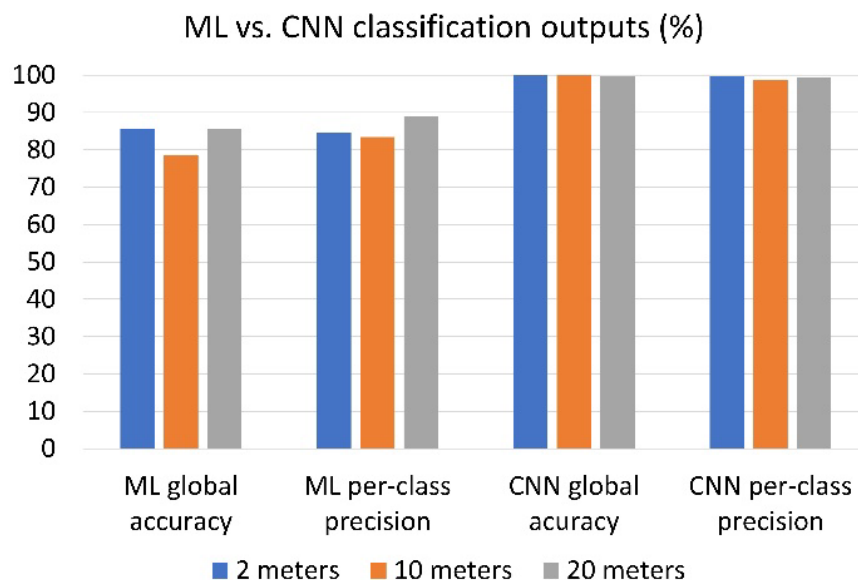


Figure 4.11: Global accuracy and pre-class precision: best performing machine learning vs. deep learning classification models based on SAM cosine similarity thresholds at 2 m, 10 m and 20 m.

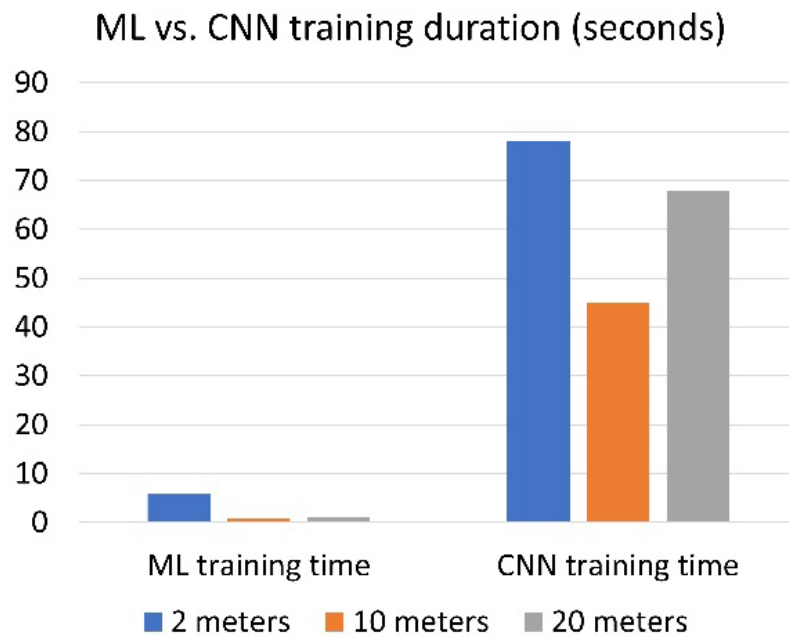


Figure 4.12: Model training durations: best performing machine learning vs. deep learning classification models based on SAM cosine similarity thresholds at 2 m, 10 m and 20 m.

4.5. Conclusions

This paper proposed the employment of a multispectral UAV drone-mounted camera in the automatic identification of magnetite iron sands at a placer deposit. First, the UAV drone was flown at 3 different flight elevations of 2 m, 10 m, and 20 m so as to find the optimum magnetite iron sand identification flight height. Based on flight times, power consumption and the number of spectral images captured, 20 m flight elevation was the most viable. The paper went on to investigate the SAM analysis at these 3 flight elevations. It was found that the SAM cosine similarities could indeed identify the magnetite iron sand target areas at 2 m, 10 m and 20 m at 0.12, 0.13 and 0.17 cosine similarity threshold values respectively, from the 6 bands multispectral images.

Using the respective cosine similarity thresholds per flight elevation, the paper continued to address the viability of coupling SAM analysis with different AI models. It was found that the proposed coupled system did indeed yield industry viable outputs across all flight

heights. However, considering all outputs of this study, it was found that the best overall performance ratios were demonstrated at 20 m flight elevation. At this elevation, the UAV drone was able to capture 6 bands multispectral images with a spatial resolution of 338 m². Furthermore, using the 6 bands multispectral imagery data, a 1D CNN DL model with a global accuracy of 99.7% and a per-class precision of 99.4% was found as the best overall AI model.

The study has demonstrated system capabilities with the potential for applicability in the mining industry/sphere. These applications include rock and mineral exploration from a remote location; mapping of mine sites via UAV drone technology; the ability to identify rocks and minerals based on their cosine similarities (SAM analysis) to a reference or known spectrum; the ability to take advantage of multispectral imaging from an elevation and distance of one's choosing, and lastly, the flexibility of applying objective AI models in the classification of rocks and minerals (as demonstrated with magnetite).

CHAPTER 5: Study Conclusions

This chapter sums up the conclusions made in Chapters 1, 2, 3 and 4, as well as presents the study's overall conclusions.

In Chapter 1, the study discusses how several industries, are starting to realize the benefits offered by artificial intelligence (AI) based methods. With particular interest to the mining industry, where classification of rocks and minerals is of the utmost importance, one is able to imagine how AI-based methods would potentially be able to improve this task, therefore offering a plethora of advantages. Henceforth, this paper proposed the employment of hyperspectral as well as multispectral imaging techniques in an attempt to classify rocks and minerals based on their spectral signatures.

In Chapter 2, with eight plutonic and volcanic igneous rock lithologies namely andesite, basalt, dacite, gabbro granite, diorite, granodiorite and rhyolite as the subject, the study had the following conclusions:

From hyperspectral imaging, rocks can be distinguished via their visible-near-infrared range spectral signatures (400-1000 nm). These anomalies can be presented in various ways, such as whole rock image average signatures which are easier for human interpretation since each rock is presented as a single anomaly. Or, as image partitions which results in multitudes of spectral signatures per rock image. Though this data is hard to interpret via human visual observations, it offers one the opportunity to train and take advantage of imagery focused AI techniques, namely the deep learning one-dimensional convolution neural network (1D CNN).

Having trained the 1D CNN, it was found that classification of each of the eight rock lithologies via their hyperspectral signatures was indeed achieved. Three 1D CNN models were trained, the first focused on classifying plutonic rocks which obtained a global accuracy of 88.2%, the second focused on volcanic rocks, obtaining a global accuracy of 74.3%, whilst the

third focused on classifying all eight igneous rocks and obtained a global accuracy of 96.4%. The study also found that based on classification precision capacities of the three 1D CNNs, the best precision values were as follows: andesite 96%, basalt 81.3%, dacite 100%, diorite 84.3%, gabbro 97.7%, granite 93.2%, granodiorite 97.7% and rhyolite 79.5%. These findings deem the combination of hyperspectral imaging with deep learning 1D CNN models a viable technique by which rock delineation may be performed in this computer age.

Chapter 3 employed the same database of the eight igneous rock lithologies as Chapter 2, the study had the following conclusions:

Though analysis of rocks via their hyperspectral image signatures is a highly capable method in which rocks can be distinguished, hyperspectral imaging suffers from the dimensionality curse due to the hundreds of spectral bands/ dimensionalities which include redundant or unimportant bands. Hence, a neighbourhood component analysis (NCA) dimensionality reduction (DR) technique was used in identifying the 5 most important spectral bands out of a total of 204 spectral bands. In essence, this means the system transitions from hyperspectral imaging to being multispectral imaging. The study found that the 5 most important discriminatory spectral bands each possessing an accuracy of $\pm 3\text{nm}$ were bands located at positions 14, 46, 116, 133 and 169 from the initial 204 bands. These positions translate to 441 nm, 535 nm, 741 nm, 791 nm and 897 nm respectively.

To assess the capabilities of these 5 now multispectral bands in classifying the eight rock lithologies, AI in the form of machine learning algorithms was brought into the picture. It was found that post-NCA, the best performing ML model was the Cubic SVM with a global accuracy and per class precision of 70.9% and 72% respectively. When performing optimizations for each of the rocks against others within the database using 8 different ML models, it was found that the average global accuracy and average individual rock prediction

precision outputs were 95.4% and 91.2% respectively. Given the 97.5% dimensionality reduction from 204 to 5 bands magnitude, these output results deem this system highly viable in the discrimination of rocks via specialized multispectral bands post NCA DR.

Chapter 4 was a remote sensing case study on mineral classification based on magnetite iron sands. The study had the following conclusions:

The study aimed at classifying magnetite iron sands from a placer deposit via an unmanned aerial vehicle (UAV) at 3 different flight elevations, 2 m, 10 m and 20 m. The production drone in question had 6 pre-set multispectral bands. Pre-set means the bands are not factory specialized to classify magnetite iron sands. However, using spectral angle mapping (SAM) cosine similarity, the study was able to pinpoint the reference/ sought after magnetite iron sands at SAM threshold limits of 0.12, 0.13 and 0.17 at 2 m, 10 m and 20 m respectively for the 30 m by 90 m study area.

Using these threshold limits, image segmentation maps were extracted from each of the 6 bands deep images in order to create a database with labelled variables (magnetite and non-magnetite), which meant supervised ML, as well as DL models, could be taken advantage of. From training the ML models, the attained global accuracies were 85.7%, 78.6% and 85.7% at 2 m, 10 m and 20 m flight elevations, whilst with the 1D CNNs, attained global accuracies were 99.9%, 99.9% and 99.7% respectively. A look into the attained per-class precisions shows that with the ML models attained 84.5%, 83.4%, and 89.9% classification capabilities, these model classification capabilities are different from the 99.9%, 99.9% and 99.7% attained via the CNN at 2 m, 10 m and 20 m flight elevations respectively. Therefore, based on the UAV drone flight history, SAM analysis, and model capabilities, it was concluded that the overall best cost-performance ratios were demonstrated at 20 m flight elevation.

In closing, having considered all outputs of this study, it was found spectral imaging techniques are indeed a viable procedure by which rock and mineral delineation may be performed in this digital age. Moreover, results from the study showed that in comparison, DL models, on average, perform better than ML models in classification problems. Lastly, both DL and ML models offer one the opportunity to fine-tune and optimize the algorithms such that the resulting models perform even better in the classification of rocks and/or minerals given the intention of use of such models.

REFERENCES

- Al Sallab, A. A.; Rashwan, M. A. Self Learning Machines Using Deep Networks. In 2011 International Conference of Soft Computing and Pattern Recognition (SoCPaR); IEEE: Dalian, China, 2011; pp 21–26. <https://doi.org/10.1109/SoCPaR.2011.6089108>.
- Altaf, F.; Islam, S. M. S.; Akhtar, N.; Janjua, N. K. Going Deep in Medical Image Analysis: Concepts, Methods, Challenges and Future Directions. arXiv:1902.05655 [cs] 2019.
- Asscher, Y.; Angelini, I.; Secco, M.; Parisatto, M.; Chaban, A.; Deiana, R.; Artioli, G. Mineralogical Interpretation of Multi-spectral Images: The Case Study of the Pigments in the Frigidarium of the Sarno Baths, Pompeii. *J. Archaeol. Sci. Rep.* 2021, 35, 102774, doi:10.1016/j.jasrep.2020.102774.
- Ayesha, S.; Hanif, M.K.; Talib, R. Overview and Comparative Study of Dimensionality Reduction Techniques for High Dimensional Data. *Inf. Fusion* 2020, 59, 44–58, doi:10.1016/j.inffus.2020.01.005
- Bar-Hillel, A.; Hertz, T.; Shental, N.; Weinshall, D. Learning a Mahalanobis Metric from Equivalence Constraints. *J. Mach. Learn. Res.* 2005, 6, 937–965.
- Bar-Hillel, A.; Hertz, T.; Shental, N.; Weinshall, D. Learning Distance Functions Using Equivalence Relations. In Proceedings of the Twentieth International Conference on Machine Learning (ICML-2003), Washington, DC, USA, 21–24 August 2003. Available online: https://www.researchgate.net/publication/221344999_Learning_Distance_Functions_using_Equivalence_Relations (accessed on 23 March 2021).

- Bhattacharya, S.; Chauhan, P.; Rajawat, A. S.; Ajai; Kumar, A. S. K. Lithological Mapping of Central Part of Mare Moscoviense Using Chandrayaan-1 Hyperspectral Imager (HySI) Data. *Icarus* 2011, 212 (2), 470–479. <https://doi.org/10.1016/j.icarus.2011.02.006>.
- Beretta, F.; Rodrigues, A. L.; Peroni, R. L.; Costa, J. F. C. L. Automated Lithological Classification Using UAV and Machine Learning on an Open Cast Mine. *Applied Earth Science* 2019, 128 (3), 79–88. <https://doi.org/10.1080/25726838.2019.1578031>.
- Burley, L. L.; Barnes, S. J.; Laukamp, C.; Mole, D. R.; Le Vaillant, M.; Fiorentini, M. L. Rapid Mineralogical and Geochemical Characterisation of the Fisher East Nickel Sulphide Prospects, Western Australia, Using Hyperspectral and PXRF Data. *Ore Geology Reviews* 2017, 90, 371–387. <https://doi.org/10.1016/j.oregeorev.2017.04.032>
- Carrino, T. A.; Crósta, A. P.; Toledo, C. L. B.; Silva, A. M. Hyperspectral Remote Sensing Applied to Mineral Exploration in Southern Peru: A Multiple Data Integration Approach in the Chapi Chiara Gold Prospect. *International Journal of Applied Earth Observation and Geoinformation* 2018, 64, 287–300. <https://doi.org/10.1016/j.jag.2017.05.004>.
- Chauhan, D.; Anyanwu, E.; Goes, J.; Besser, S. A.; Anand, S.; Madduri, R.; Getty, N.; Kelle, S.; Kawaji, K.; Mor-Avi, V.; Patel, A. R. Comparison of Machine Learning and Deep Learning for View Identification from Cardiac Magnetic Resonance Images. *Clinical Imaging* 2022, 82, 121–126. <https://doi.org/10.1016/j.clinimag.2021.11.013>.
- Chen, X.; Warner, T. A.; Campagna, D. J. Integrating Visible, near-Infrared and Short-Wave Infrared Hyperspectral and Multispectral Thermal Imagery for Geological Mapping at Cuprite, Nevada. *Remote Sensing of Environment* 2007, 110 (3), 344–356. <https://doi.org/10.1016/j.rse.2007.03.015>

- Debba, P.; van Ruitenbeek, F. J. A.; van der Meer, F. D.; Carranza, E. J. M.; Stein, A. Optimal Field Sampling for Targeting Minerals Using Hyperspectral Data. *Remote Sensing of Environment* 2005, 99 (4), 373–386. <https://doi.org/10.1016/j.rse.2005.05.005>.
- Deegalla, S.; Walgama, K.; Papapetrou, P.; Boström, H., “Random subspace and random projection nearest neighbor ensembles for high dimensional data” *Expert Systems with Applications* 191, 116078 (2022).
- Dolz, J.; Desrosiers, C.; Ben Ayed, I. 3D Fully Convolutional Networks for Subcortical Segmentation in MRI: A Large-Scale Study. *NeuroImage* 2018, 170, 456–470. <https://doi.org/10.1016/j.neuroimage.2017.04.039>.
- Estrada-Ruiz R.H. and Pérez-Garibay R. Neural networks to estimate bubble diameter and bubble size distribution of flotation froth surfaces. *The Southern African Institute of Mining and Metallurgy* 109 (2009) 441-446.
- Farooq, S.; Govil, H. Mapping Regolith and Gossan for Mineral Exploration in the Eastern Kumaon Himalaya, India Using Hyperion Data and Object Oriented Image Classification. *Advances in Space Research* 2014, 53 (12), 1676–1685. <https://doi.org/10.1016/j.asr.2013.04.002>.
- Fox N., Parbhakar-Fox A., Moltzen J., Feig S., Goemann K., Huntington J. Applications of hyperspectral mineralogy for geoenvironmental characterisation. *Minerals Engineering* 107 (2017) 63–77. <https://doi.org/10.1016/j.mineng.2016.11.008>.
- Gaffey, C.; Bhardwaj, A. Applications of Unmanned Aerial Vehicles in Cryosphere: Latest Advances and Prospects. *Remote Sensing* 2020, 12 (6), 948. <https://doi.org/10.3390/rs12060948>.

- Galal, A.; Hasan, H.; Imam, I. F. Learnable Hyperspectral Measures. *Egyptian Informatics Journal* 2012, 13 (2), 85–94. <https://doi.org/10.1016/j.eij.2012.04.004>.
- Galdames, F.J.; Perez, C.A.; Estévez, P.A.; Adams, M. Rock Lithological Classification by Hyperspectral, Range 3D and Col-or Images. *Chemom. Intell. Lab. Syst.* 2019, 189, 138–148, doi:10.1016/j.chemolab.2019.04.006.
- Ganesh, U.K.; Kannan, S.T. Creation of Hyper Spectral Library and Lithological Discrimination of Granite Rocks Using SVCHR -1024: Lab Based Approach. *J. Hyperspectral Remote. Sens.* 2017, 7, 168–177.
- Gholami, R.; Moradzadeh, A.; Yousefi, M. Assessing the Performance of Independent Component Analysis in Remote Sens-ing Data Processing. *J Indian Soc Remote Sens* 2012, 40 (4), 577–588. <https://doi.org/10.1007/s12524-011-0189-9>.
- Girouard, G.; Bannari, A.; Harti, A. E.; Desrochers, A. Validated Spectral Angle Mapper Algorithm for Geological Mapping: Comparative Study between Quickbird and Landsat-TM. 6. 2004.
- Goldberger, J.; Roweis, S.; Hinton, G.; Salakhutdinov, R. Neighbourhood Components Analysis. 8. Available online: <https://www.cs.toronto.edu/~hinton/absps/nca.pdf> (accessed on 5 February 2021).
- Gunduz, H. An Efficient Dimensionality Reduction Method Using Filter-Based Feature Selection and Variational Auto en-coders on Parkinson’s Disease Classification. *Biomed. Signal Process. Control.* 2021, 66, 102452, doi:10.1016/j.bspc.2021.102452.
- Hartog, D. den; Harlaar, J.; Smit, G. The Stumblemeter: Design and Validation of a System That Detects and Classifies Stumbles during Gait. *Sensors* 2021, 21 (19), 6636. <https://doi.org/10.3390/s21196636>.

- Haixiang, G.; Yijing, L.; Shang, J.; Mingyun, G.; Yuanyue, H.; Bing, G. Learning from Class-Imbalanced Data: Review of Methods and Applications. *Expert Systems with Applications* 2017, 73, 220–239. <https://doi.org/10.1016/j.eswa.2016.12.035>.
- Heinz-H. Erbe, John E., Udd ,J. Sasiadek (2004). Mining Automation. *IFAC Proceedings*, Volume 37, Issue 5, June 2004, Pages 299-304. [https://doi.org/10.1016/S1474-6670\(17\)32384-4](https://doi.org/10.1016/S1474-6670(17)32384-4)
- Hu, H.; Feng, D.-Z.; Chen, Q.-Y. A Novel Dimensionality Reduction Method: Similarity Order Preserving Discriminant Analysis. *Signal Process.* 2021, 182, 107933, doi:10.1016/j.sigpro.2020.107933.
- Jackisch; Madriz; Zimmermann; Pirttijärvi; Saartenoja; Heincke; Salmirinne; Kujasalo; Andreani; Gloaguen. DroneBorne Hyperspectral and Magnetic Data Integration: Otanmäki FeTiV Deposit in Finland. *Remote Sensing* 2019, 11 (18), 2084. <https://doi.org/10.3390/rs11182084>.
- Jang H., Topal E., and Kawamura Y. Unplanned dilution and ore loss prediction in longhole stoping mines via multiple regression and artificial neural network analyses. *The Southern African Institute of Mining and Metallurgy* 115 (2015) 449-456.
- Jain, U.; Nathani, K.; Ruban, N.; Joseph Raj, A.N.; Zhuang, Z.; Mahesh, V.G.V. Cubic SVM Classifier Based Feature Extraction and Emotion Detection from Speech Signals. In *Processing of the 2018 International Conference on Sensor Networks and Signal (SNSP)*, Xi'an, China, 28–31 October 2018. doi:10.1109/SNSP.2018.00081.
- Jia F., Lein Y., Lin J., Zhou X., Lu N. Deep neural networks: A promising tool for fault characteristic mining and intelligent diagnosis of rotating machinery with massive data. *Mechanical Systems and Signal Processing* 72 (2016)-73, 303–315. doi:10.1016/j.ymsp.2015.10.025.

- Jiang, Z.; Li, J. High Dimensional Structural Reliability with Dimension Reduction. *Struct. Saf.* 2017, 69, 35–46, doi:10.1016/j.strusafe.2017.07.007.
- Jie Liang., Jun Zhou., Lei Tong., Xiao Bai., Bin Wang. Material based salient object detection from hyperspectral images. *Pattern Recognition*. 76 (2018) 476–490.
- Jun-Hu Cheng., Da-Wen Sun. Hyperspectral imaging as an effective tool for quality analysis and control of fish and other seafoods: Current research and potential applications. *Trends in Food Science & Technology* 37 (2014) 78-91.
- Kobayashi S.; Ikuta K.; Sugimoto R.; Honda H.; Yamada M.; Tominaga O.; Shoji J.; Taniguchi M. Estimation of submarine groundwater discharge and its impact on the nutrient environment at Kamaiso beach, Yamagata, Japan. *NIPPON SUISAN GAKKAISHI* 2019, 85 (1), 30–39. <https://doi.org/10.2331/suisan.18-00020>.
- Kalia, V.; Walker, D.I.; Krasnodemski, K.M.; Jones, D.P.; Miller, G.W.; Kioumourtzoglou, M.-A. Unsupervised Dimensionality Reduction for Exposome Research. *Curr. Opin. Environ. Sci. Health* 2020, 15, 32–38, doi:10.1016/j.coesh.2020.05.001.
- Kartun-Giles, A.P.; Bianconi, G. Beyond the Clustering Coefficient: A Topological Analysis of Node Neighbourhoods in Complex Networks. *Chaos Solitons Fractals X* 2019, 1, 100004, doi:10.1016/j.csf.2019.100004.
- Kim, S.; Kim, H. Hyperspectral Image-Based Analysis of Weathering Sensitivity for Safety Diagnosis of Seongsan Ilchulbong Peak. *International Journal of Applied Earth Observation and Geoinformation* 2016, 52, 485–501. <https://doi.org/10.1016/j.jag.2016.07.012>
- Koren, Y.; Carmel, L. Robust Linear Dimensionality Reduction. *IEEE Trans. Visual. Comput. Graph.* 2004, 10, 459–470, doi:10.1109/TVCG.2004.17.

- Kruse F. A. Mapping surface mineralogy using imaging spectrometry. *Geomorphology* 137 (2012) 41–56. doi:10.1016/j.geomorph.2010.09.032.
- Laurence, S. J. On Tracking the Motion of Rigid Bodies through Edge Detection and Least-Squares Fitting. *Exp Fluids* 2012, 52 (2), 387–401. <https://doi.org/10.1007/s00348-011-1228-6>.
- Li, J.; Wang, T. Dimension Reduction in Binary Response Regression: A Joint Modeling Approach. *Comput. Stat. Data Anal.* 2021, 156, 107131, doi:10.1016/j.csda.2020.107131.
- Li, Y.; Chai, Y.; Zhou, H.; Yin, H. A Novel Dimension Reduction and Dictionary Learning Framework for High-Dimensional Data Classification. *Pattern Recognit.* 2021, 112, 107793, doi:10.1016/j.patcog.2020.107793.
- Li Y., Hu J., Zhao X., Xie W., Li J. Hyperspectral image super-resolution using deep convolutional neural network. *Neurocomputing* 000 (2017) 1–13.
- Liu, J.; Chen, S. Discriminant Common Vecotors Versus Neighbourhood Components Analysis. *Image Vis. Comput.* 2006, 24, 249–262, doi:10.1016/j.imavis.2005.11.007.
- Ma, S.; Bargal, S. A.; Zhang, J.; Sigal, L.; Sclaroff, S. Do Less and Achieve More: Training CNNs for Action Recognition Utilizing Action Images from the Web. *Pattern Recognition* 2017, 68, 334–345. <https://doi.org/10.1016/j.patcog.2017.01.027>.
- Mangold, N.; Schmidt, M. E.; Fisk, M. R.; Forni, O.; McLennan, S. M.; Ming, D. W.; Sautter, V.; Sumner, D.; Williams, A. J.; Clegg, S. M.; Cousin, A.; Gasnault, O.; Gellert, R.; Grotzinger, J. P.; Wiens, R. C. Classification Scheme for Sedimentary and Igneous Rocks in Gale Crater, Mars. *Icarus* 2017, 284, 1–17. <https://doi.org/10.1016/j.icarus.2016.11.005>.

- Marais C. and Aldrich C. The estimation of platinum flotation grade from froth image features by using artificial neural networks. *The Southern African Institute of Mining and Metallurgy* 111 (2011) 81-85.
- Martelet, G.; Gloaguen, E.; Døssing, A.; Lima Simoes da Silva, E.; Linde, J.; Rasmussen, T. M. Airborne/UAV Multisensor Surveys Enhance the Geological Mapping and 3D Model of a Pseudo-Skarn Deposit in Ploumanac'h, French Brittany. *Minerals* 2021, 11 (11), 1259. <https://doi.org/10.3390/min11111259>.
- Meer F. The effectiveness of spectral similarity measures for the analysis of hyperspectral imagery. *International Journal of Applied Earth Observation and Geoinformation* 8 (2006) 3–17.
- Meer F., Werff H., Ruitenbeek F., Hecker C, Bakker W., Noomen M., Meijde M., Carranza J. E., Smeth B. J., Woldai T. Multi- and hyperspectral geologic remote sensing: A review. *International Journal of Applied Earth Observation and Geoinformation* 14 (2012) 112–128.
- Mei, S.; Ji, J.; Geng, Y.; Zhang, Z.; Li, X.; Du, Q. Unsupervised Spatial-Spectral Feature Learning by 3D Convolutional Auto-encoder for Hyperspectral Classification. *IEEE Trans. Geosci. Remote. Sens.* 2019, 57, 6808–6820, doi:10.1109/TGRS.2019.2908756.
- Mohajane, M.; Essahlaoui, A.; Oudija, F.; El Hafyani, M.; Cláudia Teodoro, A. Mapping Forest Species in the Central Middle Atlas of Morocco (Azrou Forest) through Remote Sensing Techniques. *IJGI* 2017, 6 (9), 275. <https://doi.org/10.3390/ijgi6090275>.
- Mohammadi, M.; Rezaei, J. Ensemble Ranking: Aggregation of Rankings Produced by Different Multi-Criteria Decision-Making Methods. *Omega* 2020, 96, 102254. <https://doi.org/10.1016/j.omega.2020.102254>.

- Nageshwaraniyer S.S., Kim K., and Son Y-J. A mine-to-mill economic analysis model and spectral imaging-based tracking system for a copper mine. *The Southern African Institute of Mining and Metallurgy* 118 (2018) 7-14.
- Nguyen, H. H.; Carter, A.; Hoang, L. V.; Vu, S. T. Provenance, Routing and Weathering History of Heavy Minerals from Coastal Placer Deposits of Southern Vietnam. *Sedimentary Geology* 2018, 373, 228–238. <https://doi.org/10.1016/j.sedgeo.2018.06.008>.
- Ono, M. Parallax Error Correction Techniques by Image Matching for ASTER/SWIR Band-to-Band Registration; Barnes, W. L., Horais, B. J., Eds.; Rome, Italy, 1995; pp 18–27. <https://doi.org/10.1117/12.198943>.
- Poria S., Cambria E., Gelbukh A. Aspect extraction for opinion mining with a deep convolutional neural network. *Knowledge-Based Systems* 108 (2016) 42–49.
- Qin, C.; Song, S.; Huang, G. Non-Linear Neighborhood Component Analysis Based on Constructive Neural Networks. In 2014 IEEE International Conference on Systems, Man, and Cybernetics (SMC); IEEE: San Diego, CA, USA, 2014; pp 1997–2002. <https://doi.org/10.1109/SMC.2014.6974214>.
- Qiu J., Zhanga C., Yua Z., Xub Q., Wua D, Lia W., Yao J. Subsetting hyperspectral core imaging data using a graphic-identification based IDL program. *Computers & Geosciences* 106 (2017) 68–76.
- Raghu, S.; Sriraam, N. Classification of Focal and Non-Focal EEG Signals Using Neighborhood Component Analysis and Machine Learning Algorithms. *Expert Systems with Applications* 2018, 113, 18–32. <https://doi.org/10.1016/j.eswa.2018.06.031>.

- Rauhala, A.; Tuomela, A.; Davids, C.; Rossi, P. UAV Remote Sensing Surveillance of a Mine Tailings Impoundment in Sub-Arctic Conditions. *Remote Sensing* 2017, 9 (12), 1318. <https://doi.org/10.3390/rs9121318>.
- Rahimi, B.; Sharifzadeh, M.; Feng, X.-T. A Comprehensive Underground Excavation Design (CUED) Methodology for Geotechnical Engineering Design of Deep Underground Mining and Tunneling. *Int. J. Rock Mech. Min. Sci.* 2021, 143, 104684, doi:10.1016/j.ijrmms.2021.104684.
- Ramamurthy, M.; Robinson, Y. H.; Vimal, S.; Suresh, A. Auto Encoder Based Dimensionality Reduction and Classification Using Convolutional Neural Networks for Hyperspectral Images. *Microprocessors and Microsystems* 2020, 79, 103280. <https://doi.org/10.1016/j.micpro.2020.103280>.
- Rowan, L. C.; Crowley, J. K.; Schmidt, R. G.; Ager, C. M.; Mars, J. C. Mapping Hydrothermally Altered Rocks by Analyzing Hyperspectral Image (AVIRIS) Data of Forested Areas in the Southeastern United States. *Journal of Geochemical Exploration* 2000, 68 (3), 145–166. [https://doi.org/10.1016/S0375-6742\(99\)00081-3](https://doi.org/10.1016/S0375-6742(99)00081-3).
- Ruiz Hidalgo, D.; Bacca Cortés, B.; Caicedo Bravo, E. Dimensionality Reduction of Hyperspectral Images of Vegetation and Crops Based on Self-Organized Maps. *Inf. Process. Agric.* 2020, doi:10.1016/j.inpa.2020.07.002.
- Saha, D.; Annamalai, M. Machine Learning Techniques for Analysis of Hyperspectral Images to Determine Quality of Food Products: A Review. *Curr. Res. Food Sci.* 2021, 4, 28–44, S2665927121000034. <https://doi.org/10.1016/j.crfs.2021.01.002>.
- Salles, R.D.R.; de Souza Filho, C.R.; Cudahy, T.; Vicente, L.E.; Monteiro, L.V.S. Hyperspectral Remote Sensing Applied to Uranium Exploration: A Case Study at the

- Mary Kathleen Metamorphic-Hydrothermal U-REE Deposit, NW, Queensland, Australia. *J. Geochem. Explor.* 2017, 179, 36–50, doi:10.1016/j.gexplo.2016.07.002
- Salvatore, M. R.; Mustard, J. F.; Head, J. W.; Marchant, D. R.; Wyatt, M. B. Characterization of Spectral and Geochemical Variability within the Ferrar Dolerite of the McMurdo Dry Valleys, Antarctica: Weathering, Alteration, and Magmatic Processes. *Antartic science* 2014, 26 (1), 49–68. <https://doi.org/10.1017/S0954102013000254>.
- Savage, S. H.; Levy, T. E.; Jones, I. W. Prospects and Problems in the Use of Hyperspectral Imagery for Archaeological Remote Sensing: A Case Study from the Faynan Copper Mining District, Jordan. *Journal of Archaeological Science* 2012, 39 (2), 407–420. <https://doi.org/10.1016/j.jas.2011.09.028>.
- Schölkopf, B.; Smola, A.; Müller, K.-R. Nonlinear Component Analysis as a Kernel Eigenvalue Problem. *Neural Computation* 1998, 10 (5), 1299–1319. <https://doi.org/10.1162/089976698300017467>.
- Shafri, H. Z. M.; Suhaili, A.; Mansor, S. The Performance of Maximum Likelihood, Spectral Angle Mapper, Neural Network and Decision Tree Classifiers in Hyperspectral Image Analysis. *J. of Computer Science* 2007, 3 (6), 419–423. <https://doi.org/10.3844/jcssp.2007.419.423>.
- Sharma, N.; Sharma, R.; Jindal, N. Machine Learning and Deep Learning Applications—A Vision. *Glob. Transit. Proc.* 2021, 2, 24–28. S2666285X21000042. <https://doi.org/10.1016/j.gltp.2021.01.004>.
- Sinaice, B. B.; Kawamura, Y.; Kim, J.; Okada, N.; Kitahara, I.; Jang, H. Application of Deep Learning Approaches in Igneous Rock Hyperspectral Imaging. In *Proceedings of the 28th International Symposium on Mine Planning and Equipment Selection - MPES 2019*; Topal, E., Ed.; Springer Series in Geomechanics and Geoen지니어ing; Springer

International Publishing: Cham, 2020; pp 228–235. https://doi.org/10.1007/978-3-030-33954-8_29.

Sinaice B. B., Takanohashi Y., Owada N., Utsuki S., Hyongdoo J., Bagai Z., Shemang E., Kawamura Y. Automatic magnetite identification at Placer deposit using mul-ti-spectral camera mounted on UAV and machine learning. In Proceedings of the 5th International Future Mining Conference 2021 - AusIMM 2021; 2021; pp 33-42. ISBN 978-1-922395-02-3.

Singh Kushwah, J.; Kumar, A.; Patel, S.; Soni, R.; Gawande, A.; Gupta, S. Comparative Study of Regressor and Classifier with Decision Tree Using Modern Tools. *Materials Today: Proceedings* 2021, S2214785321076574. <https://doi.org/10.1016/j.matpr.2021.11.635>.

Sitharam T. G & Kolathayar S. Chapter 4 - Geotechnical considerations for coastal reservoirs. *Sustainable Water Resource Development Using Coastal Reservoirs*, 2020, 61-83.

Spinetti, C.; Mazzarini, F.; Casacchia, R.; Colini, L.; Neri, M.; Behncke, B.; Salvatori, R.; Buongiorno, M. F.; Pareschi, M. T. Spectral Properties of Volcanic Materials from Hyperspectral Field and Satellite Data Compared with LiDAR Data at Mt. Etna. *International Journal of Applied Earth Observation and Geoinformation* 2009, 11 (2), 142–155. <https://doi.org/10.1016/j.jag.2009.01.001>.

Tang, P.; Wang, X.; Huang, Z.; Bai, X.; Liu, W. Deep Patch Learning for Weakly Supervised Object Classification and Discovery. *Pattern Recognition* 2017, 71, 446–459. <https://doi.org/10.1016/j.patcog.2017.05.001>.

Taylor, G.R. Mineral and Lithology Mapping of Drill Core Pulps Using Visible and Infrared Spectrometry. *Nat. Resour. Res.* 2000, 9, 257–268, <https://doi.org/10.1023/A:1011501125239>

- Tong, Z.; Gao, J.; Zhang, H. Recognition, Location, Measurement, and 3D Reconstruction of Concealed Cracks Using Con-volutional Neural Networks. *Constr. Build. Mater.* 2017, 146, 775–787, doi:10.1016/j.conbuildmat.2017.04.097.
- Tuttaß, T.; Bryngdahl, O. Neural Learning Algorithm for Halftoning. *Optics Communications* 1995, 113 (4–6), 360–364. [https://doi.org/10.1016/0030-4018\(94\)00570-K](https://doi.org/10.1016/0030-4018(94)00570-K).
- van der Meer, F. The Effectiveness of Spectral Similarity Measures for the Analysis of Hyperspectral Imagery. *Int. J. Appl. Earth Obs. Geoinf.* 2006, 8, 3–17, doi:10.1016/j.jag.2005.06.001.
- van der Meer, F. D.; van der Werff, H. M. A.; van Ruitenbeek, F. J. A.; Hecker, C. A.; Bakker, W. H.; Noomen, M. F.; van der Meijde, M.; Carranza, E. J. M.; Smeth, J. B. de; Woldai, T. Multi- and Hyperspectral Geologic Remote Sensing: A Review. *International Journal of Applied Earth Observation and Geoinformation* 2012, 14 (1), 112–128. <https://doi.org/10.1016/j.jag.2011.08.002>.
- van Ruitenbeek, F. J. A.; Cudahy, T. J.; van der Meer, F. D.; Hale, M. Characterization of the Hydrothermal Systems Associated with Archean VMS-Mineralization at Panorama, Western Australia, Using Hyperspectral, Geochemical and Geothermometric Data. *Ore Geology Reviews* 2012, 45, 33–46. <https://doi.org/10.1016/j.oregeorev.2011.07.001>.
- Venna, J. Dimensionality Reduction for Visual Exploration of Similarity Structures. 82. Available online: <https://www.researchgate.net/publication/27516587> (accessed on 23 March 2021).
- Vetrivel A., Gerke M., Kerle N., Nex F., Vosselman G. Disaster damage detection through synergistic use of deep learning and 3D point cloud features derived from very high resolution oblique aerial images, and multiple-kernel-learning. *ISPRS Journal of Photogrammetry and Remote Sensing*. DOI: 10.1016/j.isprsjprs.2017.03.001

- Weyermann, J.; Schläpfer, D.; Hueni, A.; Kneubühler, M.; Schaepman, M. Spectral Angle Mapper (SAM) for Anisotropy Class Indexing in Imaging Spectrometry Data; Shen, S. S., Lewis, P. E., Eds.; San Diego, CA, 2009; p 74570B. <https://doi.org/10.1117/12.825991>.
- Wright, R.; Lucey, P.; Crites, S.; Horton, K.; Wood, M.; Garbeil, H. BBM/EM Design of the Thermal Hyperspectral Imager: An Instrument for Remote Sensing of Earth's Surface, Atmosphere and Ocean, from a Microsatellite Platform. *Acta Astronautica* 2013, 87, 182–192. <https://doi.org/10.1016/j.actaastro.2013.01.001>.
- Xing J., Lib K., Hua W., Yuana C., Ling H. Diagnosing deep learning models for high accuracy age estimation from a single image. *Pattern Recognition* 66 (2017) 106–116.
- Yang, C.; Everitt, J. H. Using Spectral Distance, Spectral Angle and Plant Abundance Derived from Hyperspectral Imagery to Characterize Crop Yield Variation. *Precision Agric* 2012, 13 (1), 62–75. <https://doi.org/10.1007/s11119-011-9248-z>.
- Yang, W.; Wang, K.; Zuo, W. Neighborhood Component Feature Selection for High-Dimensional Data. *JCP* 2012, 7 (1), 161–168. <https://doi.org/10.4304/jcp.7.1.161-168>.
- Zhang, C.; Lei, Y.-K.; Zhang, S.; Yang, J.; Hu, Y. Orthogonal Discriminant Neighborhood Analysis for Tumor Classification. *Soft Comput.* 2016, 20, 263–271, [doi:10.1007/s00500-014-1501-8](https://doi.org/10.1007/s00500-014-1501-8).
- Zhang, L.; He, Z.; Liu, Y. Deep Object Recognition across Domains Based on Adaptive Extreme Learning Machine. *Neurocomputing* 2017, 239, 194–203. <https://doi.org/10.1016/j.neucom.2017.02.016>.

Zhang, X.; Li, P. Lithological Mapping from Hyperspectral Data by Improved Use of Spectral Angle Mapper. *International Journal of Applied Earth Observation and Geoinformation* 2014, 31, 95–109. <https://doi.org/10.1016/j.jag.2014.03.007>.

Zheng, Y.; Liu, Q.; Chen, E.; Zhao, J. L.; He, L.; Lv, G. Convolutional Nonlinear Neighbourhood Components Analysis for Time Series Classification. In *Advances in Knowledge Discovery and Data Mining*; Cao, T., Lim, E.-P., Zhou, Z.-H., Ho, T.-B., Cheung, D., Motoda, H., Eds.; *Lecture Notes in Computer Science*; Springer International Publishing: Cham, 2015; Vol. 9078, pp 534–546. https://doi.org/10.1007/978-3-319-18032-8_42.

Zuniga, M.M.; Murangira, A.; Perdrizet, T. Structural Reliability Assessment through Surrogate Based Importance Sampling with Dimension Reduction. *Reliab. Eng. Syst. Saf.* 2021, 207, 107289, doi:10.1016/j.ress.2020.107289.